

POLARIMETRIC DOPPLER RADAR AND ELECTRICAL OSERVATIONS OF
DEEP MOIST CONVECTION ACROSS NORTHERN ALABAMA DURING THE
DEEP CONVECTIVE CLOUDS AND CHEMISTRY EXPERIMENT

by

ANTHONY L. BAIN

A THESIS

Submitted in partial fulfillment of the
requirements for the degree of Master of Science

In

The Department of Atmospheric Science

To

The School of Graduate Studies

Of

The University of Alabama in Huntsville

HUNTSVILLE, ALABAMA

2013

In presenting this thesis in partial fulfillment of the requirements for the Master of Science degree from the University of Alabama in Huntsville, I agree that the Library of this University shall make it freely available for inspection. I further agree that permission for extensive copying for scholarly purposes may be granted by my advisor in his/her absence, by the Chair of the Department or by the Dean of the School of Graduate Studies. It is also understood that due recognition shall be given to me and the University of Alabama in Huntsville in any scholarly use which may be made of any material in this thesis.

THESIS APPROVAL FORM

Submitted by Anthony L. Bain in partial fulfillment of the requirements for the degree of Master of Science in Atmospheric Science and accepted on behalf of the Faculty of the School of Graduate Studies by the thesis committee.

We, the undersigned members of the Graduate Faculty of the University of Alabama in Huntsville, certify that we have advised and/or supervised the candidate on the work described in this thesis. We further certify that we have reviewed the thesis manuscript and approve it in partial fulfillment of the requirements for the degree of Master of Science in Atmospheric Science.

_____ Committee Chair

_____ Department Chair

_____ College Dean

_____ Graduate Dean

ABSTRACT

School of Graduate Studies

The University of Alabama in Huntsville

Degree Master of Science College/Dept. Science/Atmospheric Science

Name of Candidate Anthony Lamont Bain

Title: Polarimetric Doppler Radar and Electrical Observations of Deep Moist Convection across Northern Alabama during the Deep Convective Clouds and Chemistry Experiment

The Deep Convective Clouds and Chemistry (DC3) experiment seeks to understand the kinematic and microphysical controls on the lightning behavior of deep moist convection. Ultimately, a key objective is to use DC3 observations to develop quantitative relationships for the parameterization of flash rate in numerical cloud models that do not explicitly resolve electrification processes. This study utilized multiple dual-polarization Doppler radars across northern Alabama to quantify microphysical and kinematic properties and processes that often serve as precursors to lightning such as the graupel echo volume, graupel mass and convective updraft volume. Relationships between these radar inferred properties and the total lightning flash rate were developed. This study concludes that the best relationship between a radar inferred quantity and total lightning flash rate in terms of the Pearson product moment correlation and lowest root mean square error was the graupel echo volume ($\rho = 0.91$, RMSE = 2.7 flashes per minute).

Abstract Approval: Committee Chair _____

(Date)

Department Chair _____

Graduate Dean _____

ACKNOWLEDGEMENTS

I would like to acknowledge all M.S. Advisor, Dr. Larry D. Carey for his relentless patience and willingness to work with me. He and Dr. Brad Smull of the National Science Foundation have given me a great opportunity to work on a large scale project that was the Deep Convective Clouds and Chemistry Experiment. Secondly, I'd like to thank my other committee members, Dr. Kevin Knupp and Dr. John Mecikalski. Furthermore, I'd like to thank Dr. Phil Bitzer who acted as a supplemental committee member. Next, I'd like to acknowledge Chris and Elise Schultz for offering their expertise in the fields of Lightning and Radar Meteorology. I'd like to thank Mariana Felix for her IT support and Retha Mathee for assistance and collaboration of various radar and lightning computations. I'd like to also thank my officemates, Ryan Rogers and Danielle Kozlowksi who were always willing to discuss various aspect of my research. These discussions really assisted in the success of this research. Last, but not least, I'd like to thank Dr. Sundar Christopher for accepting my application to the University of Alabama in Huntsville. This has been a truly rewarding experience!

TABLE OF CONTENTS

LIST OF FIGURES.....	ix
LIST OF TABLES.....	xxii
Chapter	
1. Introduction.....	1
2. Background.....	3
2.1 Conceptual model of thunderstorms.....	3
2.2 Observations and Numerical Modeling of NO _x	9
2.3 Theories of Cloud Electrification.....	15
2.3.1 The Convective Charging Mechanism.....	15
2.3.2 The Inductive Charging Mechanism(s).....	16
2.3.3 The Non-Inductive Charging Mechanism.....	17
2.4 A Review of Past Studies that examined Microphysical, Kinematic, and Lightning Relationships.....	21
2.5 Thesis Objective and Goals.....	26
3. Data and Methodology.....	29
3.1 DC3 Experimental Design.....	29
3.2 DC3 Alabama Domain.....	31
3.3 Overview of the ARMOR and KHTX radar platforms.....	32
3.4 Overview of the North Alabama Lightning Mapping Array.....	35
3.5 Overview of the National Lightning Detection Network.....	36
3.6 Comments about the Radiosonde Operations.....	37
3.7 ARMOR and KHTX data.....	38
3.8 Overview of C-band NCAR PID.....	42

3.9	Quality control of NALMA and NLDN data.....	43
3.10	Quality control of UAH Mobile Radiosonde Observation (RAOB) Data...	45
3.11	Cell Identification and Tracking.....	46
3.12	Calculation of Microphysical, Kinematic and Electrical Quantities.....	46
4.	Results.....	49
4.1	18 May 2012 Case Day.....	50
4.1.1	Meteorological Overview	50
4.1.2	Developing Phase of Complex A1 2203-2211 UTC.....	54
4.1.3	Initial Lightning Activity of Complex A1 2215 UTC.....	60
4.1.4	Increasing Lightning Part I 2231-2243 UTC.....	67
4.1.5	Increasing Lightning Part II 2248 UTC.....	71
4.1.6	Increasing Lightning Part III 2304 UTC.....	73
4.1.7	Dissipation Phase of Complex A1.....	75
4.2	21 May 2012 Case Day.....	78
4.2.1	Meteorological Overview	78
4.2.2	Development of two separate updrafts 1945-2001 UTC.....	81
4.2.3	Lightning Production in Northernmost Updraft 2002-2012 UTC....	84
4.2.4	Lightning Production the Southernmost Updraft 2004-2015 UTC..	86
4.2.5	Rapid Lightning Increase Post Updraft Merger 2015-2023 UTC....	88
4.2.6	Decay and Dissipation Stages of B2 2026-2057 UTC.....	92
4.3	11 June 2012 Case Day.....	95
4.3.1	Meteorological Overview.....	95
4.3.2	Developing and Initial Lightning Phase 1815-1845 UTC.....	98
4.3.3	Continued Lightning 1854 UTC.....	101

4.3.4 Increasing Lightning 1859-1928 UTC.....	103
4.3.5 Decreasing Lightning Activity 1933-1958 UTC.....	106
4.3.6 Increasing Lightning Part II 2000 – 2030 UTC.....	107
4.3.7 Decaying Phase 2030-2100 UTC.....	107
4.4 14 June 2012.....	108
4.4.1 Meteorological Overview.....	108
4.4.2 Developing Stage and Initial Lightning Activity 1600-1610 UTC.....	110
4.4.3 Rapid increase in Lightning Production 1628-1652 UTC.....	111
4.4.4 Peak Lightning Production 1703 -1709 UTC.....	114
4.4.5 Decline in Lightning Production 1713-1800 UTC.....	116
5. Discussion.....	117
5.1 Discussion of DC3 AL Case Days.....	117
5.2 Discussion on errors associated with DC3 AL Dataset.....	128
6. Summary and Conclusions.....	130
6.1 Summary.....	130
6.2 Conclusions.....	131
Appendix A.....	136
Appendix B.....	138
References.....	141

LIST OF FIGURES

Figure	Page
2.1	Adapted from Byers and Braham (1949) and modified by Doswell (1985), this figure shows the three stages of the ordinary, single-celled thunderstorms. Velocity vectors derived from aircraft observations are denoted. The vertical solid lines indicate precipitation. The solid black horizontal lines represent heights in both ft. and km. The dashed line indicates the 0 °C level. In the leftmost pane, the towering cumulus stage is depicted. The center most pane shows the mature phase. The rightmost pane displays the dissipating stage.....4
2.2	Results from numerical simulations of sensitivity of cold pool to vertical wind shear from Rotunno et al. (1988). The vectors depict airflow and magnitude of air motion. The contour fill represents negative potential temperature perturbations at 2 K intervals (beginning at a perturbation 1 K below ambient theta). Examples of no vertical wind shear over the lowest 2 km of the domain, 20 m s ⁻¹ of wind shear over the lowest 2 km and 30 m s ⁻¹ of wind shear in the lowest 2 km are depicted in the top, middle and bottom panes, respectively.....7
2.3	Schematic of time evolution of multicellular convection as suggested by Doswell (1985) [modified by Markowski and Richardson (2010)]. The vectors represent air flow around the convective cells, with the gust front represented by the solid blue line with barbs. The horizontal radar reflectivity (dBZ) is indicated in the contour filled and the cloud boundary is outlined. The horizontal radar reflectivity begins at 50 dBZ (yellow fill) with an interval of 20 dBZ. The top pane depicts an instantaneous schematic of a multicellular complex at any given point in its lifecycle. The middle pane represents 10 minutes after the top pane, and the bottom pane represents 20 minutes after the top pane.....8
2.4	Simplified diagram from Williams (2001) showing the various lightning flashes. This image assumes a “normal” polarity storm in which the higher portion of the convective cloud attains a predominantly positive charge (associated with positively charged ice crystals) and the lower portion of the cloud retains a predominately negative charge (associated with negatively charged rimed graupel). From left to right, schematics of an intra-cloud (IC) and cloud-to-ground (CG) flashes.....19
2.5	Illustration of the charge separated to the riming ice particle during rebounding rimer-ice crystal collisions as a function of the effective liquid water content (g m ⁻³) and temperature (°C). The (+) denotes regions of positive polarity while the (-) denotes regions of negative polarity. Adapted from Saunders et al. (1991).....20

- 3.1. Schematic of the AL domain during the DC3 field project. The solid red circle represents the location of the ARMOR radar at KHSV. The solid orange circle represents the location of the MAX radar site at New Market, AL. The solid blue circle represents the location of KHTX at Hytop, AL. The green triangles show the location of NALMA sensor locations. Note that the northern GA sites are excluded. The dashed lines represents the ARMOR-KHTX multi-Doppler regions.....32
- 4.1. 1200 UTC objective upper air analysis from the NOAA Storm Prediction Center. Panel A represents the 700 hPa pressure surface, Panel B represents the 850 hPa pressure surface, Panel C represents the 500 hPa pressures surface and Panel D represents the 300 hPa pressure surface...51
- 4.2. Comparison of 1200 UTC RAOB from Redstone Arsenal, AL (a) on 18 May 2012 and 1800 UTC UAH (b) mobile RAOB taken from Fayetteville, TN.....52
- 4.3. CAPPI at 3 km from ARMOR at 2203 UTC. Contour filled image represents Z_h in dBZ and the solid lines represents the vertical motion field in intervals of 2, 5, 10, 15, 20, and 25 $m s^{-1}$. Horizontal winds are plotted.....54
- 4.4. CAPPI at 3 km from ARMOR at 2203 UTC. Contour filled image represents Z_h in dBZ, solid vertical lines represent vertical motion in intervals of 2, 5, 10, 15, 20, and 25 $m s^{-1}$. NALMA Lightning Initiation (LI) points are denoted in the solid black circle and NLDN CG Flashes are denoted in the solid brown circle. Horizontal winds are plotted.....55
- 4.5. Corresponding ARMOR PPI of A1 from 2203 UTC on 18 May 2012. Left panel (a) is ρ_{hv} from 2203 UTC and right panel (b) is Z_h from 2203 UTC. The elevation angle is around 9.8° or just over 3 km. The circled region highlights regions in which ρ_{hv} drops to around 0.85. The level of $0^\circ C$ is at 3 km..... 56
- 4.6. Left panel (a) represents a CAPPI at 5 km from ARMOR at 2203 UTC. The contour filled image represents the Z_h in dBZ and solid lines represent the vertical motion field in intervals of 2, 5, 10, 15, 20, and 25 $m s^{-1}$. Horizontal wind vectors are plotted. The solid black line at 20 km represents the location of the X-Z cross-section. The right panel (b) is a vertical cross-section in the X-Z plane taken at 20 km north of ARMOR. Contour filled image represents Z_h in dBZ and solid lines represent regions of upward vertical motion. Contour intervals for vertical motion are 2, 4, 6, 8, 10, 15, 20, 25 $m s^{-1}$57
- 4.7. Left panel (a) represents a CAPPI at 5 km from ARMOR at 2203 UTC. Contour filled image represents Z_h in dBZ and solid vertical lines represent vertical motion in intervals of 2, 5, 10, 15, 20, and 25 $m s^{-1}$. The

solid black line at 20 km represents the location of the X-Z cross-section. Horizontal wind vectors are plotted. The right panel (b) is a vertical cross-section in the X-Z plane taken at 20 km north of ARMOR. Contour filled image represents the horizontal radar reflectivity in dBZ and dashed line contour represents differential radar reflectivity greater than 0 dB at 1 dB increments.....59

4.8. CAPPI at 7 km from ARMOR at 2211 UTC. Contour filled image represents Z_h in dBZ, solid vertical lines represent vertical motion in intervals of 2, 5, 10, 15, 20, and 25 $m s^{-1}$. Horizontal wind vectors are plotted.....60

4.9. Left panel (a) represents a CAPPI at 5 km from ARMOR at 2215 UTC. The contour filled image represents the Z_h in dBZ and the solid lines represent the vertical motion field in intervals of 2, 5, 10, 15, 20, and 25 $m s^{-1}$. NALMA Lightning Initiation (LI) points are denoted in the solid black circle and NLDN CG Flashes are denoted in the solid brown circle. Horizontal wind vectors are plotted. The right panel (b) is a vertical cross-section in the X-Z plane taken at 28 km north of ARMOR. Contour filled image represents the horizontal radar reflectivity in dBZ and solid lines represent regions of upward vertical motion. Contour intervals for vertical motion are 2, 4, 6, 8, 10, 15, 20, 25 $m s^{-1}$62

4.10. Left panel (a) represents a CAPPI at 5 km from ARMOR at 2215 UTC. The contour filled image represents Z_h in dBZ and the solid vertical lines represent vertical motion in intervals of 2, 5, 10, 15, 20, and 25 $m s^{-1}$. NALMA Lightning Initiation (LI) points are denoted in the solid black circle and NLDN CG Flashes are denoted in the solid brown circle. Horizontal wind vectors are plotted. The right panel (b) is a vertical cross-section in the X-Z plane taken at 28 km north of ARMOR. The contour filled image represents the horizontal radar reflectivity in dBZ and dashed line contour represents differential radar reflectivity greater than 0 dB at 1 dB increments.....64

4.11. Co-evolution of kinematic and electrical properties for A1 on 18 May 2012. Left panel (a) represents the time series evolution of the maximum updraft velocity (solid brown line) as determined from multi-Doppler wind synthesis within the -10 °C and -40 °C temperature levels. The right panel (b) represents the time series evolution of the updraft volume greater than 5 $m s^{-1}$ (solid brown line) within the -10 °C and -40 °C temperature levels and the total lightning flash. In (a) and (b) the total lightning flash rate (solid blue line) as inferred from NALMA and the CG flash rate (solid red line) as inferred from the NLDN are both depicted.....64

- 4.12. Co-evolution of kinematic and electrical properties for A1 on 18 May 2012. Left panel (a) represents the time series evolution of the graupel echo volume (solid black line) as determined from the NCAR PID within the $-10\text{ }^{\circ}\text{C}$ and $-40\text{ }^{\circ}\text{C}$ temperature levels. The right panel (b) represents the time series evolution of the graupel mass (solid black line) within the $-10\text{ }^{\circ}\text{C}$ and $-40\text{ }^{\circ}\text{C}$ temperature levels and the total lightning flash. In (a) and (b) the total lightning flash rate (solid blue line) as inferred from NALMA and the CG flash rate (solid red line) as inferred from the NLDN are depicted NLDN are both depicted.....65
- 4.13. Left panel (a) represents a CAPPI at 5 km from ARMOR at 2215 UTC. Contour filled image represents the Z_h in dBZ and the solid lines represent the vertical motion fields in intervals of 2, 5, 10, 15, 20, and 25 m s^{-1} . Horizontal wind vectors are also plotted with the NALMA Lightning Initiation (LI) points are denoted in the solid black circle and NLDN CG Flashes are denoted in the solid brown circle. The right panel (b) is a vertical cross-section in the X-Z plane taken at 15 km north of ARMOR. Contour filled image represents Z_h in dBZ and solid lines represent regions of upward vertical motion. Contour intervals for vertical motion are 2, 4, 6, 8, 10, 15, 20, 25 m s^{-1}66
- 4.14. Gridded radar cross-section in the X-Z plane 30 km north of ARMOR at 2231 UTC (left [a]) and 2235 UTC (right [b]). Both images depict Z_h (dBZ) in the color fill. The dashed contours represent $Z_{dr} > 0$ dB in intervals of 1 dB. The solid black circles present NALMA VHF initiation sources while the solid brown circles represent NLDN CG flashes. Also in each plot, the dashed blue line corresponds to the $0\text{ }^{\circ}\text{C}$ isotherm, the dashed orange line represents the $-10\text{ }^{\circ}\text{C}$ temperature level and the dashed black line represents the $-40\text{ }^{\circ}\text{C}$ level.....68
- 4.15. The left pane (a) depicts an ARMOR PPI during the 2231 UTC ARMOR scan volume. The right pane (b) depicts an ARMOR PPI during the 2235 UTC ARMOR scan volume. The approximate height of the radar beam is around 6 km in both panes. The solid white circle highlights the three body scatter spike signature.69
- 4.16. Left panel (a) represents a CAPPI at 3 km from ARMOR at 2248 UTC on 18 May 2012. Right panel (b) represents a CAPPI at 5 km from ARMOR at 2248 UTC on 18 May 2012. For both images, contour filled regions represent Z_h in dBZ and solid lines represent the vertical motion field in intervals of 2, 5, 10, 15, 20, and 25 m s^{-1} . In (a), horizontal wind vectors are plotted. NALMA Lightning Initiation (LI) points are denoted in the solid black circle and NLDN CG Flashes are denoted in the solid brown circle.....72
- 4.17. The left panel (a) is a vertical cross-section in the X-Z plane taken around 25 km north of ARMOR at 2304 UTC. The contour filled image represents the Z_h in dBZ and dashed line contour represents differential

radar reflectivity greater than 0 dB at 1 dB increments. Also, the dashed blue line corresponds to the 0 °C isotherm, the dashed orange line represents the -10 °C temperature level and the dashed black line represents the -40 °C level. Right panel (b) represents a CAPPI at 6 km from ARMOR at 2304 UTC. The contour filled image represents Z_h in dBZ and the solid black lines represent the vertical motion field in intervals of 2, 5, 10, 15, 20, and 25 $m s^{-1}$. NA LMA Lightning Initiation (LI) points are denoted in the solid black circle and NLDN CG Flashes are denoted in the solid brown circle.....74

- 4.18. Left panel (a) represents a CAPPI at 2 km from ARMOR at 2248 UTC on 18 May 2012. Right panel (b) represents a CAPPI at 12 km from ARMOR at 2304 UTC on 18 May 2012. For both images, contour filled regions represent Z_h in dBZ and the solid black lines represent the vertical motion field in intervals of 2, 5, 10, 15, 20, and 25 $m s^{-1}$. NALMA Lightning Initiation (LI) points are denoted in the solid black circle and NLDN CG Flashes are denoted in the solid brown circle. Horizontal wind vectors are plotted.....75
- 4.19. Left panel (a) represents a CAPPI at 9 km from ARMOR at 2354 UTC. Contour filled image represents Z_h in dBZ and the solid black lines represent the vertical motion field in intervals of 2, 5, 10, 15, 20, and 25 $m s^{-1}$. NALMA Lightning Initiation (LI) points are denoted in the solid black circle and NLDN CG Flashes are denoted in the solid brown circle. Horizontal wind vectors are plotted. The right panel (b) is a vertical cross-section in the X-Z plane taken at 10 km north of ARMOR during the same time. The contour filled image Z_h in dBZ and solid lines represent regions of upward vertical motion. The contour intervals for vertical motion are 2, 4, 6, 8, 10, 15, 20, 25 $m s^{-1}$. Also, the dashed blue line corresponds to the 0 °C isotherm, the dashed orange line represents the -10 °C temperature level and the dashed black line represents the -40 °C level.....77
- 4.20. Graphical representation of three flashes detected by NALMA between 2252 UTC and 2258 UTC. The top panel is a time series plot showing the approximate time and vertical extent of the VHF sources. The middle left panel is an X-Z cross-section with the right left panel representing a VHF source frequency histogram with height. The bottom left panel shows the X-Y plan view of VHF sources and the bottom right panel shows the Y-Z view of the VHF sources. Distances are relative to the NSSTC.....78
- 4.21. The left panel (a) depicts the 1200 UTC objective analysis from SPC on 21 2012 at 300 hPA. The right panel (b) is the subjective surface analysis from the Hydrometeorological Prediction Center (HPC) at 06 UTC on 21 May 2012.....79

- 4.22. Comparison of 1200 UTC RAOB from Redstone Arsenal, AL (a) on 21 May 2012 and 2037 UTC UAH mobile RAOB (b) taken from Capshaw, AL.....80
- 4.23. Left panel (a) represents a CAPPI at 5 km from ARMOR at 2001 UTC on 21 May 2012. Contour filled image represents the Z_h in dBZ and the solid black lines represent the vertical motion field in intervals of 2, 5, 10, 15, 20, and 25 $m s^{-1}$. The solid black line denotes the X-Z cross-section location (around 76 km north of ARMOR). Horizontal wind vectors are plotted. The right panel (b) is a vertical cross-section in the X-Z plane taken at 76 km north of ARMOR during the same time. Contour filled image represents the horizontal radar reflectivity in dBZ and solid lines represent regions of upward vertical motion. Contour intervals for vertical motion are 2, 4, 6, 8, 10, 15, 20, 25 $m s^{-1}$. Also, the dashed blue line corresponds to the 0 °C isotherm, the dashed orange line represents the -10 °C temperature level and the dashed black line represents the -40 °C level.....82
- 4.24. Left panel (a) represents a CAPPI at 5 km from ARMOR at 2001 UTC on 21 May 2012. Contour filled image represents the Z_h in dBZ and the solid black lines represent the vertical motion field in intervals of 2, 5, 10, 15, 20, and 25 $m s^{-1}$. The solid black line denotes the X-Z cross-section location (around 76 km north of ARMOR). Horizontal winds are plotted. The right panel (b) is a vertical cross-section in the X-Z plane taken at 76 km north of ARMOR during the same time. Contour filled image represents Z_h in dBZ and dashed lines represent Z_{dr} greater than 0 dB with increments of 1 dB. Also, the dashed blue line corresponds to the 0 °C isotherm, the dashed orange line represents the -10 °C temperature level and the dashed black line represents the -40 °C level.83
- 4.25. Time series evolution of DMC microphysics and electrical properties for complex B2 on 21 May 2012. The left panel (a) represents the time series evolution of graupel echo volume (solid black line) within the -10 °C and -40 °C temperature layer. The right panel (b) represents the graupel mass (solid black line) within the -10 °C and -40 °C temperature level. In both (a) and (b) the total lightning flash rate as inferred from NALMA (solid blue line) and the CG lightning flash rate (solid red line) are both depicted.....84
- 4.26. Time series evolution of DMC kinematic and electrical properties for complex B2 on 21 May 2012. The left panel (a) represents the time series evolution of the maximum updraft velocity (solid brown line) within the -10 °C and -40 °C temperature layer. The right panel (b) represents updraft volume $> 5 m s^{-1}$ (solid brown line) within the -10 °C and -40 °C temperature level. In both (a) and (b) the total lightning flash rate as inferred from NALMA (solid blue line) and the CG lightning flash rate (solid red line) are both depicted.....84

- 4.27. Left panel (a) represents a CAPPI at 5 km from ARMOR at 2004 UTC on 21 May 2012. The contour filled image represents the Z_h in dBZ and the solid black lines represent the vertical motion field in intervals of 2, 5, 10, 15, 20, and 25 $m s^{-1}$. NALMA Lightning Initiation (LI) points are denoted in the solid black circle and NLDN CG Flashes are denoted in the solid brown circle. The solid black line denotes the X-Z cross-section location (around 77 km north of ARMOR). Horizontal wind vectors are plotted. The right panel (b) is a vertical cross-section in the X-Z plane taken at 77 km north of ARMOR during the same time. Contour filled image represents Z_h in dBZ and dashed lines are contours of $Z_{dr} > 0$ dB in intervals of 1 dB. Also, the dashed blue line corresponds to the 0 °C isotherm, the dashed orange line represents the -10 °C temperature level and the dashed black line represents the -40 °C level.....85
- 4.28. Gridded radar cross-sections in the X-Z plane roughly at 65 km north of ARMOR. The time stamps for these cross-sections are around 2004 UTC. In the left panel (a), Z_h in dBZ is the contour fill, solid black lines represent the vertical motion field in intervals of 2, 4, 6, 8, 10, 15, 20, and 25 $m s^{-1}$. In the right panel (b) time, the contour filled figure represents Z_h in dBZ and dashed lines represent Z_{dr} greater than 0 dB with increments of 1 dB. Also, the dashed blue line corresponds to the 0 °C isotherm, the dashed orange line represents the -10 °C temperature level and the dashed black line represents the -40 °C level.....87
- 4.29. Gridded radar cross-sections in the X-Z plane roughly at 65 km north of ARMOR. The time stamps for these cross-sections are around 2012 UTC. In the left panel (a), Z_h in dBZ is the contour fill, solid black lines represent the vertical motion field in intervals of 2, 5, 10, 15, 20, and 25 $m s^{-1}$. In the right panel (b) time, the contour filled figure represents Z_h in dBZ and dashed lines represent Z_{dr} greater than 0 dB with increments of 1 dB. Also, the dashed blue line corresponds to the 0 °C isotherm, the dashed orange line represents the -10 °C temperature level and the dashed black line represents the -40 °C level.88
- 4.30. Gridded radar cross-sections in the X-Z plane roughly at 65 km north of ARMOR. The time stamps for these cross-sections are around 2015 UTC. In the left panel (a), Z_h in dBZ is the contour fill and the solid black lines represent the vertical motion field in intervals of 2, 5, 10, 15, 20, and 25 $m s^{-1}$. In the right panel (b), the contour filled figure represents Z_h in dBZ and dashed lines represent Z_{dr} greater than 0 dB with increments of 1 dB. Also, the dashed blue line corresponds to the 0 °C isotherm, the dashed orange line represents the -10 °C temperature level and the dashed black line represents the -40 °C level. In both panels, NALMA Lightning Initiation (LI) points are denoted in the solid black circle and NLDN CG Flashes are denoted in the solid brown circle.89
- 4.31. Gridded radar cross-sections in the X-Z plane roughly at 65 km north of ARMOR. The time stamps for these cross-sections are around 2020 UTC.

In the left panel (a) , Z_h in dBZ is the contour fill and the solid black lines represent the vertical motion field in intervals of 2, 5, 10, 15, 20, and 25 $m s^{-1}$. In the right panel (b), the contour filled figure represents Z_h in dBZ and dashed lines represent Z_{dr} greater than 0 dB with increments of 1 dB. Also, the dashed blue line corresponds to the 0 °C isotherm, the dashed orange line represents the -10 °C temperature level and the dashed black line represents the -40 °C level. In both panels, NALMA Lightning Initiation (LI) points are denoted in the solid black circle and NLDN CG Flashes are denoted in the solid brown circle.90

- 4.32. Gridded radar cross-sections in the X-Z plane roughly at 60 km north of ARMOR. The time stamps for these cross-sections are around 2023 UTC. In the left panel (a), Z_h in dBZ is the contour fill and the solid black lines represent the vertical motion field in intervals of 2, 5, 10, 15, 20, and 25 $m s^{-1}$. In the right panel (b), the contour filled figure represents Z_h in dBZ and dashed lines represent Z_{dr} greater than 0 dB with increments of 1 dB. Also, the dashed blue line corresponds to the 0 °C isotherm, the dashed orange line represents the -10 °C temperature level and the dashed black line represents the -40 °C level. In both panels, NALMA Lightning Initiation (LI) points are denoted in the solid black circle and NLDN CG Flashes are denoted in the solid brown circle.....92
- 4.33. Left panel (a) represents a CAPPI at 5 km from ARMOR at 2044 UTC on 21 May 2012. The contour filled image represents Z_h in dBZ and the solid black lines represent the vertical motion field in intervals of 2, 5, 10, 15, 20, and 25 $m s^{-1}$. NALMA Lightning Initiation (LI) points are denoted in the solid black circle and NLDN CG Flashes are denoted in the solid brown circle. The solid black line denotes the X-Z cross-section location (around 55 km north of ARMOR). Horizontal wind vectors are plotted. The right panel (b) is a vertical cross-section in the X-Z plane taken at 55 km north of ARMOR during the same time. Contour filled image represents the horizontal radar reflectivity in dBZ and solid lines represent regions of upward vertical motion. Contour intervals for vertical motion are 2, 4, 6, 8, 10, 15, 20, 25 $m s^{-1}$. Also, the dashed blue line corresponds to the 0 °C isotherm, the dashed orange line represents the -10 °C temperature level and the dashed black line represents the -40 °C level.....94
- 4.34. The 11 June 2012 1200 UTC objective upper air analysis from the NOAA Storm Prediction Center. Panel A represents the 700 hPa pressure surface, Panel B represents the 850 hPa pressure surface, Panel C represents the 500 hPa pressures surface and Panel D represents the 300 hPa pressure surface.97
- 4.35. Comparison of 1200 UTC RAOB from Redstone Arsenal, AL (a) on 11 June 2012 and 1836 UTC UAH mobile RAOB (b) taken from the NSSTC (Huntsville, AL).....97

- 4.36. Left panel (a) represents a CAPPI at 3 km from KHTX at 1815 UTC on 11 June 2012. Right panel (b) represents a vertical cross-section at $y = 105$ km from ARMOR at 1815 UTC on 11 June 2012. For both panels contour filled regions represent Z_h in dBZ. On the right panel (b), contours of Z_{dr} (dashed line) are plotted beginning at 0 dB with 0.5 dB increments. NALMA Lightning Initiation (LI) points are denoted in the solid black circle and NLDN CG Flashes are denoted in the solid brown circle. In panel (b), the dashed blue line corresponds to the 0°C isotherm, the dashed orange line represents the -10°C temperature level and the dashed black line represents the -40°C level.....99
- 4.37. Left panel (a) represents a CAPPI at 5 km from KHTX at 1840 UTC on 11 June 2012. Right panel (b) represents a vertical cross-section at $y = 115$ km from ARMOR at 1815 UTC on 11 June 2012. For both figs., contour filled regions represent Z_h in dBZ. On the right panel, contours of Z_{dr} (dashed line) are plotted beginning at 0 dB with 1 dB increments. NALMA Lightning Initiation (LI) points are denoted in the solid black circle and NLDN CG Flashes are denoted in the solid brown circle. In panel (a), horizontal wind vectors are plotted. In panel (b) , the dashed blue line corresponds to the 0°C isotherm, the dashed orange line represents the -10°C temperature level and the dashed black line represents the -40°C level.....99
- 4.38. This figure depicts a CAPPI at 5 km from ARMOR at 1844 UTC on 11 June 2012. Contour filled regions represent Z_h in dBZ, solid black lines represent the vertical motion field in intervals of 2, 5, 10, 15, 20, and 25 m s^{-1} . NALMA Lightning Initiation (LI) points are denoted in the solid black circle and horizontal wind vectors are plotted.101
- 4.39. Left panel (a) represents a CAPPI at 5 km from ARMOR at 1854 UTC on 11 2012. Right panel (b) represents a CAPPI at 9 km from ARMOR at 1854 UTC on 11 June 2012. For both images, contour filled regions represent Z_h in dBZ, solid black lines represent the vertical motion field in intervals of 2, 5, 10, 15, 20, and 25 m s^{-1} . NALMA Lightning Initiation (LI) points are denoted in the solid black circle and horizontal wind vectors are plotted.....102
- 4.40. Co-evolution of kinematic and electrical properties for C1 on 11 June 2012. Left panel (a) represents the time series evolution of the maximum updraft velocity (solid brown line) as determined from multi-Doppler wind synthesis within the -10°C and -40°C temperature levels and the total lightning flash rate as inferred from NALMA. The dashed brown line represents the maximum updraft velocity within the -10°C and -40°C temperature layer and the solid blue line represents the total lightning flash rate as inferred from NALMA. The solid red line represents the NLDN inferred CG flash rate. The right panel (b) represents the time series evolution updraft volume greater than 5 m s^{-1} (sold brown line) within the -10°C and -40°C temperature levels and the total lightning

- flash rate (solid blue line) as inferred from NALMA. The solid red line represents the NLDN inferred CG flash rate.....104
- 4.41. Time series evolution of DMC microphysics and electrical properties for complex C1 on 11 June 2012. The left panel (a) represents the time series evolution of graupel echo volume (solid black line) within the -10 °C and -40 °C temperature layer and total lightning flash rate as inferred from NALMA (solid blue line). The solid red line denotes the CG lightning flash rate as determined by NLDN. The right panel (b) represents the graupel mass (solid black line) within the -10 °C and -40 °C temperature layer and the total lightning flash rate as inferred from NALMA (solid blue line). The solid red line denotes the CG lightning flash rate as determined by NLDN.....105
- 4.42. Left panel (a) represents a CAPPI at 5 km from ARMOR at 1909 UTC on 11 June 2012. The contour filled image represents the horizontal radar reflectivity in dBZ and the solid black lines represent the vertical motion field in intervals of 2, 5, 10, 15, 20, and 25 m s⁻¹. NALMA Lightning Initiation (LI) points are denoted in the solid black circle and NLDN CG Flashes are denoted in the solid brown circle. The solid black line denotes the X-Z cross-section location (around 100 km north of ARMOR). Horizontal wind vectors are plotted. The right panel (b) is a vertical cross-section in the X-Z plane taken at 100 km north of ARMOR during the same time. Contour filled image represents the horizontal radar reflectivity in dBZ and solid lines represent regions of upward vertical motion. Contour intervals for vertical motion are 2, 4, 6, 8, 10, 15, 20, 25 m s⁻¹. Also ,the dashed blue line corresponds to the 0 °C isotherm, the dashed orange line represents the -10 °C temperature level and the dashed black line represents the -40 °C level.....105
- 4.43. Comparison of 1200 UTC RAOB from Redstone Arsenal, AL (a) on 14 June 2012 and 1730 UTC UAH mobile RAOB (b) taken from near Guntersville, AL.....108
- 4.44. CAPPI at 3 km from ARMOR at 1610 UTC on 14 June 2012. Contour filled image represents the horizontal radar reflectivity in dBZ. NALMA Lightning Initiation (LI) points are denoted in the solid black circle and NLDN CG Flashes are denoted in the solid brown circle.....111
- 4.45. Time series evolution of DMC microphysics and electrical properties for complex D1 on 14 June 2012. The left panel represents the time series evolution of graupel mass (dashed brown line) within the -10 °C and -40 °C temperature layer and total lightning flash rate as inferred from NALMA (solid blue line) The solid red line denotes the CG lightning flash rate as determined by NLDN. The right panel represents the graupel echo volume (dashed black line) within the -10 °C and -40 °C temperature layer and the total lightning flash rate as inferred from NALMA (solid blue

- line). The solid red line denotes the CG lightning flash rate as determined by NLDN.....112
- 4.46. Left panel (a) represents a CAPPI at 5 km from ARMOR at 1628 UTC on 14 June 2012. The contour filled image represents the horizontal radar reflectivity in dBZ. NALMA Lightning Initiation (LI) points are denoted in the solid black circle and NLDN CG Flashes are denoted in the solid brown circle. The solid black line denotes the X-Z cross-section location (around 18 km north of ARMOR). The right panel (b) is a vertical cross-section in the X-Z plane taken at 18 km north of ARMOR during the same time. Contour filled image represents the horizontal radar reflectivity in dBZ. Also, the dashed blue line corresponds to the 0 °C isotherm, the dashed orange line represents the -10 °C temperature level and the dashed black line represents the -40 °C level.113
- 4.47. Left panel (a) represents a CAPPI at 5 km from ARMOR at 1652 UTC on 14 June 2012. Contour filled image represents the horizontal radar reflectivity in dBZ. NALMA Lightning Initiation (LI) points are denoted in the solid black circle and NLDN CG Flashes are denoted in the solid brown circle. The solid black line denotes the X-Z cross-section location (around 15 km north of ARMOR). The right panel (b) is a vertical cross-section in the X-Z plane taken at 15 km north of ARMOR during the same time. Contour filled image represents the horizontal radar reflectivity in dBZ. Also, the dashed blue line corresponds to the 0 °C isotherm, the dashed orange line represents the -10 °C temperature level and the dashed black line represents the -40 °C level.....114
- 4.48. Left panel (a) represents a CAPPI at 5 km from ARMOR at 1706 UTC on 14 June 2012. Contour filled image represents the horizontal radar reflectivity in dBZ. NALMA Lightning Initiation (LI) points are denoted in the solid black circle and NLDN CG Flashes are denoted in the solid brown circle. The solid black line denotes the X-Z cross-section location (around 10 km north of ARMOR). The right panel (b) is a vertical cross-section in the X-Z plane taken at 10 km north of ARMOR during the same time. Contour filled image represents the horizontal radar reflectivity in dBZ. Also, the dashed blue line corresponds to the 0 °C isotherm, the dashed orange line represents the -10 °C temperature level and the dashed black line represents the -40 °C level.....115
- 4.49. A scatterplot updraft volume greater than 5 m s⁻¹ within the -10 °C and -40 °C layer for all DC3 AL cases excluding 14 June 2012 versus the total lightning flash rate is displayed in panel (a), while a scatterplot of the maximum updraft velocity within the -10 °C and -40 °C layer for all DC3 AL cases excluding 14 June 2012 versus the total lightning flash rate is displayed in panel (b). In each figure, the data points are color coded by date. Solid blue circles correspond to data points of complex A1 (18 May 2012), solid red circles correspond to complex B1 and B2 (21 May 2012),

and solid orange circles correspond to complex C1 (11 June 2012). The solid red line represents the best fit line.....119

4.50. Scatterplot of graupel echo volume within the -10 °C and -40 °C layer for all DC3 AL cases. The filled circles are radar derived graupel echo volume within the -10 °C to -40 °C layer and corresponding total lightning flash rate. Solid blue circles correspond to data points of complex A1, solid red circles correspond to complex B1 and B2, solid orange circles correspond to complex C1, and solid black circles correspond to complex D1.....121

4.51. Scatterplot of graupel mass within the -10 °C and -40 °C layer for all DC3 AL cases. The filled circles are radar derived graupel masses within the -10 °C to -40 °C layer and corresponding total lightning flash rate. Solid blue circles correspond to data points of complex A1, solid red circles correspond to complex B1 and B2, solid orange circles correspond to complex C1, and solid black circles correspond to complex D1.....122

4.52. Scatterplot of 30 dBZ echo volume within the -10 °C and -40 °C layer for all DC3 AL cases. The filled circles are radar derived 30 dBZ echo volume within the -10 °C to -40 °C layer and corresponding total lightning flash rate. Solid blue circles correspond to data points of complex A1, solid red circles correspond to complex B1 and B2, solid orange circles correspond to complex C1, and solid black circles correspond to complex D1.....122

A.1 The chart shows a sensitivity study of VHF source criteria for a DMC event during DC3 across northern AL on 18 May 2012. This DMC event was roughly 80 km from the center of NALMA. VHF sources are clustered using the McCaul 2005 algorithm. The solid blue line represents a 5 source criteria, the solid red line represents a 10 source criteria, and the solid green line represents a 15 source criteria.....136

A.2 The chart shows a sensitivity study of VHF source criteria for a DMC event during DC3 across northern AL on 11 June 2012. This DMC event was roughly 80 km from the center of NALMA. VHF sources are clustered using the McCaul 2005 algorithm. The solid blue line represents a 5 source criteria, the solid red line represents a 10 source criteria, and the solid green line represents a 15 source criteria.....137

A.3 This chart shows the results from a sensitivity study that varies the direction of the integration of the anelastic mass continuity equation. Vertical motion is determined from this integration process. The sensitivity study is performed on data from the 18 May 2012 case day. The

dashed black line represents the updraft volume $> 5 \text{ m s}^{-1}$ in which the updraft velocity was computed using explicit downward integration of the anelastic mass continuity equation. The dotted light violet line represents the updraft volume $> 5 \text{ m s}^{-1}$ in which the updraft velocity was computed using the variational method of integration of the anelastic mass continuity equation.....137

LIST OF TABLES

Table	Page
4.1.	A summary of convective parameters for the 18 May 2012 case day from the 1800 UTC UAH mobile RAOB.....52
4.2.	A summary of convective parameters for the 21 May 2012 case day from the 2037 UTC UAH mobile RAOB.....81
4.3.	A summary of convective parameters for the 11 June 2012 case day from the 1836 UTC UAH mobile RAOB. The RAOB was taken at the NSSTC located in Huntsville, AL.....98
4.4	A summary of convective parameters for the 14 June 2012 case day from the 1730 UTC UAH mobile RAOB.....109
4.5.	Comparison of thermodynamic, electrical, and kinematic properties during DC3 AL.....118
4.6.	Comparison of thermodynamic, electrical, and microphysical properties during DC3 AL.....121
4.7	Results from statistical analysis performed on radar observables during DC3 AL.....123
4.8	Additional storm parameters (30 dBZ echo volume and updraft volume > 3 m s ⁻¹).....126
4.9.	Comparison between updraft volume > 3 m s ⁻¹ and updraft volume > 5 m s ⁻¹ versus total flash rate for all case events during DC3 AL.....127
B.1	NWS Volume Coverage Patterns (VCP) of the WSR-88D.....138
B.2	ARMOR and MAX Scan pattern during DC3.....138
B.3	NCAR PID Category Table.....139
B.4	Quality Control of RAOB Data during the DC3 Experiment.....139
B.5	Summary of Convective Events across northern AL/Southern TN.....140

CHAPTER ONE

INTRODUCTION

The Deep Convective Clouds and Chemistry (DC3) experiment is an interdisciplinary study that seeks to investigate and understand the relationship between the microphysical, kinematic, and electrical properties of deep moist convection (Barth et al. 2012). These properties of deep moist convection (DMC) and the associated environment can be examined using a variety of remote sensing platforms. The high temporal and spatial sampling demands imposed by DC3 science objectives allowed for an in depth examination of microphysical, kinematic, and electrical observations of DMC. The use of multiple dual-polarization Doppler weather radars results in improved observation of hydrometeors and associated microphysical processes that occur within the convective cloud. These microphysical processes can then be linked back to the kinematic and ultimately electrical structure of DMC. In addition, three dimensional kinematic flows and estimates of vertical motion associated with DMC are determined through the use of multi-Doppler wind synthesis techniques. This is particularly desirable to atmospheric chemists as one of the primary objectives of DC3 is to understand DMC's role in the creation and transport of natural and anthropogenic atmospheric constituents throughout the depth of the troposphere. Multi-Doppler wind synthesis can be used to compare observed kinematic structures of DMC with conceptual models of three dimensional kinematic flows around DMC as well as with numerical model simulations of DMC. While there have been numerous studies that have utilized polarimetric Doppler weather radar for their analysis of DMC, only a few studies have provided any type of

analysis that could ultimately be utilized for direct use in an atmospheric chemistry numerical cloud model. Cloud electrification is thought to play a pivotal role in the production of nitrogen oxides (NO_x). The electrical characteristics of DMC during DC3 were documented via very high frequency (VHF) lightning mapping arrays (LMA) and low frequency (LF) to very low frequency (VLF) sensors. The motivation behind the careful documentation of lightning during DC3 was two-fold; 1) it is theorized that lightning can be a useful parameter for describing the intensity of DMC (especially in the absence of weather radar) and 2) it is an important phenomenon that has widespread use in the atmospheric chemistry modeling community. Numerical modeling of lightning flash type, rate, and extent are important due to their hypothesized role in the production of nitrogen oxides (NO_x). The motivation for understanding lightning behaviors from the perspective of an atmospheric chemist will be discussed in detail in the background section. The purpose of this multi-sensor approach for analyzing DMC during DC3 has three main objectives: 1) compare and contrast environmental differences between DMC with varying microphysical, kinematic and electrical properties, 2) document important microphysical and kinematic processes that are thought to be relevant to cloud electrification and lightning production and 3) provide a useful radar observable-total lightning characteristic relationship that can be used to parameterize the production of NO_x via lightning in numerical cloud models that do not include explicitly resolve electrification and lightning physical processes.

CHAPTER 2

BACKGROUND

The background section will highlight a few items as it pertains to observing and modeling of NO_x . Conceptual models of thunderstorm morphology as well as theories of charging and subsequent cloud electrification are summarized. Previous radar-lightning relationships are examined in detail. An overview of the DC3 AL network is provided in the following subsections.

2.1 Conceptual model of thunderstorms

Byers and Braham (1949) developed a conceptual model of the ordinary thunderstorm during the Thunderstorm project over Florida. During this experiment, simplistic, but detailed characteristics of DMC were documented using S-Band weather radar onboard the P-61C aircrafts. Byers and Braham (1949) noted that the examined “thunderstorm” was composed of more than one convective cell. As such, it was proposed that the use of the term thunderstorm cells was more appropriate. More importantly, however, the authors noted that the DMC in this study consisted of three distinct phases: 1) the cumulus phase, 2) the mature phase, and 3) the dissipating and anvil development phase. A graphical representation of these phases can be seen in Fig. 2.1.

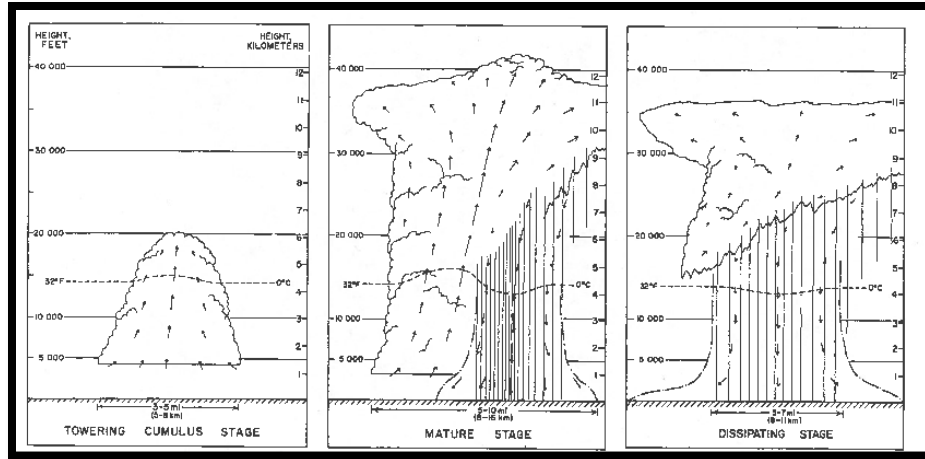


Figure 2.1. Adapted from Byers and Braham (1949) and modified by Doswell (1985), this figure shows the three stages of the ordinary, single-celled thunderstorms. Velocity vectors derived from aircraft observations are denoted. The vertical solid lines indicate precipitation. The solid black horizontal lines represent heights in both ft. and km. The dashed line indicates the 0 °C level. In the leftmost pane, the towering cumulus stage is depicted. The center most pane shows the mature phase. The rightmost pane displays the dissipating stage.

During the cumulus phase, very little precipitation was observed with estimated vertical motions of less than $2\text{-}3\text{ m s}^{-1}$ within a given convective cell. It was hypothesized that during this phase, vertical motions in excess of 30 m s^{-1} were possible depending on the organization of the DMC (e.g. size, severity). Also during this phase, very little downward motion is observed. The authors attribute this to the ability of the updraft to loft or suspend hydrometeors aloft. As these hydrometeors grow larger, the updraft loses its ability to keep the particles suspended. As these particles continue to grow, they often fall through the weaker portion of the updraft. As such, the generation of negative buoyancy via air cooled by evaporation results in the development of the downdraft. The melting of ice hydrometeors and precipitation drag are also considered to be important for the development of downdrafts in ordinary DMC. It was also pointed out that the region of the most intense surface precipitation rate denoted the convective downdraft at

lower altitudes. The precipitation cooled air often becomes collocated within the updraft and proves to be detrimental to the growth of the DMC.

In the mature phase, vertical motions were comparable to those noted in the cumulus phase. Finally, the dissipating and anvil development stage is marked by a decrease in the upward vertical motion and a weak surface precipitation rate. Vertical motions during this phase often dropped below that observed in the cumulus stage. Photogrammetry revealed that the convective cloud often dissipated from the base upward, leaving the anvil as the only resemblance of any convective cell. Moreover, the development of a “pseudo cold front” as a result of the convective downdraft was theorized to be pertinent to the development of additional convective cells. Numerical simulations have shown that this pseudo cold front or gust front is associated with relatively cooler air that originates within the downdraft. The importance of this gust front will be discussed briefly.

Weisman and Klemp (1984), Rotunno et al. (1988), and Bluestein (1993) showed through numerical modeling that the strength of deep vertical wind shear often dictates the morphology and longevity of DMC. Firstly, Weisman and Klemp (1984) suggested that the shape of the hodograph could be used to discriminate between environments that produced different convective morphologies (e.g., single cell, multicell, and supercell). In a qualitative sense, a small and/or linear hodograph suggests very little in the way of vertical wind shear. Environments characterized as having weak vertical wind shear supported ordinary single and multicellular DMC. Conversely, stronger vertical wind shear facilitated quasi-steady, rotating updrafts typical of supercellular DMC. Rotunno et al. (1988) argued that wind shear was important for maintaining a vorticity budget

between convective updrafts and their associated cold pools. Little wind shear resulted in an unbalanced vorticity budget in which the vorticity associated with the cold pool would dominate. In the absence of sufficient lift along the cold pool and ambient environment interface, the convective cells would dissipate. In the event of a balanced vorticity budget, the cold pool and wind shear vorticity contributions were equal in magnitude. This would result in sufficient lift along the cold pool such that continued growth of additional convective cells occurred. Bluestein (1993) suggested that the magnitude of deep vertical shear was important as well. Similar to Rotunno et al. (1988), Bluestein (1993) determined that little vertical wind shear would not foster continued lift along the cold pool gust front such that new parcels could be lifted to the level of free convection (LFC). Moreover, an overabundance of vertical shear would prove to be destructive to the cold pool as mechanical mixing would possibly homogenize the gradient in theta associated with the cold pool gust front. The optimal balance between the cold pool and wind shear contributions would be needed to ensure that continued lift along the cold pool gust front would occur and thus the development of additional cells. Pictorial representations of these simulations are displayed in Fig. 2.2. Doswell (1985) was one of the first to provide a schematic that discusses the lifecycle of multicellular convection. A schematic created by Markowski and Richardson (2010) provides a few snapshots of the cloud- and airflow structure of multicellular convection. From Fig. 2.3 (produced by Markowski and Richardson 2010, adapted from Doswell 1985), it is shown that the strong downdraft of the most mature cell, which is generated via negative buoyancy associated with precipitation, contributes most to the motion of the convective outflow.

Enhanced convergence along the gust front serves to strengthen the next convective cell. This process continues until sufficient lifting of parcels to their LFCs ceases.

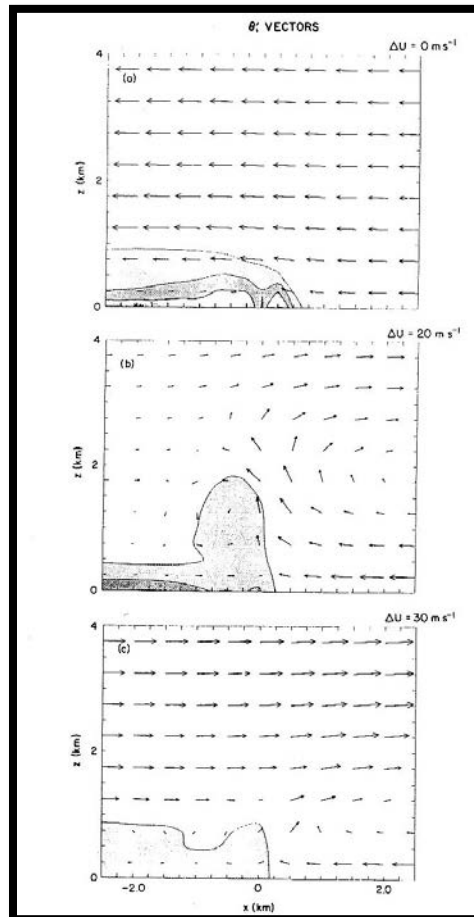


Figure 2.2. Results from numerical simulations of sensitivity of cold pool to vertical wind shear from Rotunno et al. (1988). The vectors depict airflow and magnitude of air motion. The contour fill represents negative potential temperature perturbations at 2 K intervals (beginning at a perturbation 1 K below ambient theta). Examples of no vertical wind shear over the lowest 2 km of the domain, 20 m s^{-1} of wind shear over the lowest 2 km and 30 m s^{-1} of wind shear in the lowest 2 km are depicted in the top, middle and bottom panes, respectively

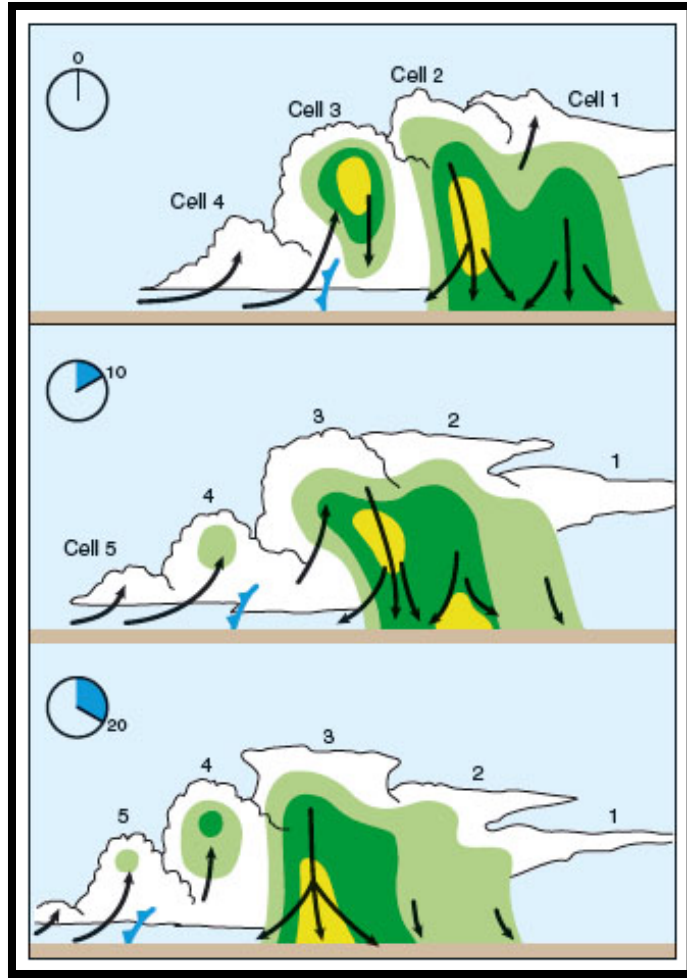


Figure 2.3. Schematic of time evolution of multicellular convection as suggested by Doswell (1985) [modified by Markowski and Richardson (2010)]. The vectors represent air flow around the convective cells, with the gust front represented by the solid blue line with barbs. The horizontal radar reflectivity (dBZ) is indicated in the contour filled and the cloud boundary is outlined. The horizontal radar reflectivity begins at 50 dBZ (yellow fill) with an interval of 20 dBZ. The top pane depicts an instantaneous schematic of a multicellular complex at any given point in its lifecycle. The middle pane represents 10 minutes after the top pane, and the bottom pane represents 20 minutes after the top pane.

It will be shown through the use of the Skew-T Log P diagram that a majority of the environments across DC3 AL fostered the development of ordinary, multicellular convection. The ordinary, multicellular convection will often be referred to as convective complexes. These convective complexes often persisted on the order of 1-2 hours and were generally a result of weak deep layer shear $< 25 \text{ m s}^{-1}$ with modest to moderate

amounts of convective available potential energy (CAPE) that ranged from just below 1000 J kg^{-1} to over 2000 J kg^{-1} . The convective events were generally weakly forced from a synoptic standpoint. Most of the convective events were a result of strong solar insolation, differential heating along the terrain of the Appalachians, and/or convergence along remnant convective outflow from previous thunderstorm activity. In a few instances, a mesoscale convective systems (MCS) developed. The environments during these episodes could be characterized as having a higher amount of deep layer shear. Consistent with Weisman and Klemp (1984), Rotunno et al. (1988), and Bluestein (1993), these convective episodes were longer lasting than their multicellular counterparts. The results presented here will focus on the ordinary multicellular convection, however.

2.2 Observations and Numerical Modeling of NO_x

As mentioned previously, DC3 aims to quantify the relationship between DMC and its role in the production and transport of NO_x and other atmospheric constituents throughout the troposphere. Transport of anthropogenic constituents that reside in the planetary boundary layer (PBL) via DMC is another aspect of DC3. The generation of NO_x ($\text{NO}_x = \text{NO} + \text{NO}_2$) from lightning (LNO_x) as a result of DMC is outlined by Barthe et al. (2010) as one of the more important atmospheric chemistry goals. Lightning fixation is one of the leading theories of the production of naturally occurring NO_x . According to Hill et al. (1980) the generation of nitrogen and oxygen (e.g. O_2 , N_2) gas molecules occurs during the cooling of the lightning channel. NO_x has been shown to be a key part of earth's radiation budget as it serves as a catalyst for the creation of the greenhouse gas ozone (O_3) (Pickering et al. 1998; Dye et al. 2000). Stratospheric and

upper tropospheric O₃ has long been theorized to shield the lower troposphere from harmful ultraviolet (UV) rays that originate from the sun. Conversely, lower tropospheric (e.g. the PBL) O₃ has been known to facilitate the development of smog that may result in respiratory ailments in humans. DMC often serves as an efficient engine to transport NO_x throughout the troposphere and could certainly foster the latter scenario. In addition, DMC could be an effective mechanism to transport O₃, NO_x and other constituents from the planetary boundary layer upward into the troposphere. Lamarque et al. (1996) and Pickering et al. (1998) illustrated through the use of global chemical models that lightning is one of the leading causes of the natural development of NO_x in the upper troposphere.

Pickering et al. (1998) examined convection from several experiments including the Global Atmospheric Research Project (GARP Atlantic Tropical Experiment (GATE)) across the western Atlantic just offshore the west coast of Africa, the Tropical Ocean Global Atmosphere-Coupled Ocean Atmospheric Research Project (TOGA-CORE) across the western Pacific ocean and the Preliminary Regional Experiment for Stormscale Operational and Research Meteorology (PRESTORM) that took place across KS and OK. These three distinct locations allowed for sampling of DMC over both continental and maritime tropical locations. A comparison of modeled vertical profiles of LNO_x mixing ratios after both supercell and multicell DMC events revealed some unique findings. In supercells, the largest quantities of LNO_x mixing ratios tended to be confined to the lowest 0-1 km of the PBL. Conversely, vertical profiles of LNO_x mixing ratios in multicellular DMC showed that the larger LNO_x mixing ratios were aloft between 12-14 km. Pickering et al. (1998) concluded that the relatively strong downdraft (likely the rear

flank downdraft) of supercell thunderstorms serves to transport the LNO_x mixing ratio aloft downward into the PBL. Weaker downdrafts associated with multicellular DMC (with the exception of strong macro- or microbursts) were less efficient at transferring LNO_x mixing ratios down into the PBL (Pickering et al. 1998).

There is some controversy amongst the atmospheric chemistry community as to whether or not the lightning type (e.g. cloud-to-ground [CG], intra-cloud [IC]) has any influence on the amount of NO_x generated per flash. Barthe and Barth (2008) provide an exhaustive list of studies that examine this aspect of NO_x production. Some modeling studies of NO_x suggest that there is roughly an order of magnitude difference between CG and IC lightning (Price et al. 1997; Pickering et al. 1998; Dye et al. 2000). Price et al. (1997) explicitly state that CG flashes produce more NO_x than IC flashes based on the notion of stronger energetics associated with CG's. By taking the product of the breakdown potential and the integrated current pulse, Price et al. (1997) note that the energy of a CG flash is an order of magnitude greater than what is observed with an IC flash. From a magnitude of peak current perspective, Price et al. (1997) argued that the return stroke of CG lightning is the most efficient at producing the highest quantity of NO_x.

Through the use of a three dimensional model of tropospheric oxidized nitrogen, Gallardo and Cooray (1996) showed that the amount of NO_x produced per IC flash may rival or exceed the amount of NO_x produced per CG flashes. As a result, it was argued that perhaps modifications to the strength of the global lightning source used in models are necessary based on findings in their study. Similarly, Cooray (1997) noted that for a relatively small amount of charge (q) neutralized by the discharge and a given charge

density, the amount of energy dissipated occurred primarily in the leader stage of lightning. In a case examined by Cooray (1997), it was noted that 70% of energy dissipated was associated with the leader. In this case, the amount of charge neutralized was around 0.5 C with a charge distribution around 3 km.

During the Stratospheric-Tropospheric Experiment: Radiation, Aerosols and Ozone (STERAO) field experiment, however, Dye et al. (2000) observed a storm across northeastern CO that produced a copious amount of IC lightning. Specifically, they noted that the IC:CG ratio for this storm was approximately 100:1, a much larger ratio than what had been assumed previously. As a result of the overwhelming number of IC flashes to CG flashes for this case, Dye et al. (2000) argued that IC lightning was the significant contributor to the NO_x budget, at least for this convective event. Also, it was noted that a majority of the NO_x induced by lightning for this case occurred primarily in the anvil. Climatologically speaking, Boccippio et al. (2001) noted that a region of anomalously high IC:CG ratios existed across portions of northeastern CO, southwestern NE, and northwestern KS. This was consistent with observations from Krehbiel et al. (1998) who mentioned that intense DMC across the Great Plains appeared to contain copious amounts of IC lightning. Elsewhere, including Alabama, the IC:CG ratio is quite low.

From numerical studies conducted by Pickering et al. (1998), simulated CG flashes produced a larger *instantaneous* amount of LNO_x versus IC lightning. Studies by Koshak et al. (2013) also sought to determine the contribution of NO_x from different types of lightning. The NASA Lightning Nitrogen Oxides Model (LNOM) utilizes information from both VHF data from the North Alabama Lightning Mapping Array (NALMA) as well as information on the location, time, peak current and multiplicity of

flashes from the National Lightning Detection NetworkTM (NLDN). The use of NALMA and NLDN data makes this type of analysis particularly unique. This data are then used to discriminate between IC and CG flashes near an analysis region. The amount of NO_x produced is based on empirical studies by Wang et al. (1998) and theory from Cooray et al. (2009). LNOM also attempts to model various lightning process such as hot core stepped and dart leaders, stepped leader corona sheath, K-changes, continuing currents and M-components. In a study conducted across the Southeastern U.S. during the month of August for 5 years, output from LNOM suggested that the amount of NO_x production per ground flash was approximately an order of magnitude greater than the amount of NO_x production per cloud flash.

In contrast to the aforementioned studies, Hill et al. (1980) made no attempt to discriminate between IC and CG flashes and assumed a single value for the amount of LNO_x produced per flash. Similarly, Barthe and Barth (2008) based estimations of NO_x on laboratory studies conducted by Wang et al. (1998). The relationship that was developed by Wang et al. (1998) showed that the amount of NO_x production has a dependency on the areal flash length as well as the altitude. Sensitivity tests conducted by Barthe and Barth (2008) revealed that varying the IC:CG ratio by a factor of 10 yielded (with the number of flashes being held constant) very little difference on the LNO_x profile. The authors did note, however, that the flux of NO_x into the anvil was impacted by varying the IC:CG ratio. It was argued that the electrical activity that occurred higher in the convective cloud (e.g. IC lightning) had a smaller chance of being diluted as it traversed the cloud. Electrical activity that occurred at lower portions of DMC (e.g. CG lightning) had a much higher probability of being diluted as it was transported throughout

the cloud. It is important to note that Barthe and Barth (2008) found that lightning flash extent appeared to be a useful parameter for exploring the production of NO_x . In the study, it was shown that the magnitude of the amount of NO_x produced per flash length impacted the NO_x mixing ratio near the updraft and into the anvil region. Barthe et al. (2010) explicitly tested the total lightning flash rate against various radar properties under the assumption that both IC and CG flashes produced the same amount of NO_x per flash. These results will be presented later.

The production and transport of NO_x throughout the troposphere is not the only atmospheric chemistry objective associated with DC3. Examining the transport of passive tracers via DMC is important as well. Skamarock et al. (2000) and Mullendore et al. (2005) both examined how the mode of DMC (e.g. supercellular, multicellular) dictates the magnitude of vertical transport of a given constituent or aerosol. The DMC examined by Skamarock et al. (2000) exhibited a complex morphology in which a transition from multicell to supercellular occurred during the STERAO experiment across NE CO. It was noted that during the supercell phase of the DMC, an enhancement (nearly a factor of two greater) in the transport of carbon monoxide (CO) occurred. The authors postulated that the updrafts associated with the multicellular DMC had smaller horizontal and vertical extents that resulted in relatively inefficient transport of CO and other passive tracers. Mullendore et al. (2005) simulated supercell and multicells that each were characterized with identical thermodynamic environments (e.g. identical instability), but differing deep layer vertical wind shear. For the supercell simulation, the deep layer vertical wind shear was increased such that a quasi-steady rotating updraft, characteristic of supercells, could be achieved. Similar to Skamarock et al. (2000), it was observed that the supercell was

the most efficient at transporting tracer gases up from the PBL into the upper troposphere and lower stratosphere when compared to the multicellular convection. Interestingly enough, the total mass transported upward by the supercell updraft was also a factor of two greater than the multicell, coincident with Skamarock et al. (2000).

2.3 Theories of Cloud Electrification

Most of what is understood about charging and resultant electrification has been derived from numerous laboratory experiments. Generally, there have been 3 primary theories of cloud electrification; 1) the “convective” mechanism, 2) the inductive mechanism and 3) a precipitation, ice-graupel or non-inductive mechanism. MacGorman and Rust (1998) discuss these three mechanisms and a brief overview of this discussion is provided hereafter.

2.3.1 The Convective Charging Mechanism

The Convective mechanism, proposed by Vonnegut (1953), is the process in which positive charge associated with the fair weather field is carried upward by cumulus congestus clouds. The positive charge that is carried upward is then collected and captured by various hydrometeors within the convective cloud. The theory then states that this positive charge within the developing convection results in the attraction of negative charge that begins to accumulate along the interface of the cloud (screening layer) and the ambient atmosphere. Once the cloud matures to the point in which a downdraft develops, this negative charge is transported downward where it is then re-ingested into the cloud via the updraft. This results in a positive dipole structure with positive charge located near the top of the cloud with a lower negative charge region

towards the base of the cloud. While this method explains the normal polarity storm (normal dipole), it does not adequately explain the observed tripole model associated with the level of charge reversal (e.g. this method does not address the relationship between charge polarity and temperature/liquid water content). This will be discussed later in section 2.3.3. Furthermore, this mechanism fails to account for any inverted polarity structures that have been documented by numerous observational and modeling studies.

2.3.2 The Inductive Charging Mechanism(s)

Elster and Geitel (1888) proposed an inductive charging mechanism in which hydrometeors that are previously polarized by an ambient electric field fall through a cloud. The theory notes that the cloud particles are also polarized by an ambient electric field. Elastic collisions, in which contact times between particles are sufficiently large, must occur for the transfer of charge. As the hydrometeor falls relative to the cloud particle, contact along the surface must occur. The orientation of the electric dipole of the hydrometeor will dictate the sign of the charge transferred during collision. If the cloud particle rebounds, then the charge acquired during the collision is carried away by the cloud particle.

Wilson (1929) suggested that the capture of ions via hydrometeors could also be used to explain inductive charging. This theory notes that because of the terminal fall velocity of hydrometeors, ions could be selectively captured. Assuming that the hydrometeors were polarized by some ambient electric field, the theory noted that ions of opposing polarity (meaning opposite of the charge along the collision surface of the

hydrometeor) would be captured, while those with similar polarities would be deflected away. It was argued that in the instance in which negative ions exhibited a “slow drift speed” preferential capture by positively charged hydrometeors would occur. As a result, these hydrometeors could attain a dominant polarity if enough ions of the same polarity were captured. In the case of the “slow drift speed” of the negatively charged ions, larger hydrometeors would tend to have a negative polarity.

2.3.3 The Non-Inductive Charging Mechanism

Numerous laboratory experiments, field observations and modeling studies have resulted in an overwhelming consensus amongst atmospheric scientists that the non-inductive charging (NIC) or graupel-ice collisional-based mechanism is the primary reason for cloud electrification. Unlike the inductive charging mechanisms, the NIC does not require the existence of a pre-existing electric field necessary for charging and has been used to adequately describe the varying thunderstorm polarities (e.g. normal dipole, normal tripole, inverted tripole, etc). The NIC involves stochastic rebounding collisions between graupel, which grows via riming of supercooled cloud water and ice crystals. (Reynolds et al. 1957; Takahashi 1978; Saunders 1994; Saunders and Peck 1998). Takahashi (1978) developed empirical relationships that relate the strength of the vertical gradient of the electric field and the rate of graupel electrification via NIC. In Eqn. 2.1 listed below, Takahashi (1978) noted that the number of graupel particles is proportional to the strength of the vertical gradient of the electric field. Takahashi (1978) showed that the vertical gradient of the electric field is related to the product of the number of graupel particles (N) and rate of charge of graupel particles (Eqn. 2.1). The vertical gradient of the electric field is expressed in units of $V\ km^{-1}$. Takahashi (1978) also noted that the rate

of graupel electrification is primarily a function of the graupel particle size (Eqn. 2.2). The rate of charging for a graupel particle in Eqn. 2.2 is related to the square of the graupel particle radius (R^2) in m, the number concentration of ice crystals (n), the terminal fall velocity of graupel (V) in $m\ s^{-1}$, the terminal fall velocity of ice crystals (v_i) in $m\ s^{-1}$, the electric charge per collision between graupel and ice crystals (q), and the collision efficiency between graupel and ice crystals (E).

$$\frac{dF}{dz} = -4 \times \pi \times N \times Q \quad (2.1)$$

$$\frac{dQ}{dt} = \pi \times R^2 \times n \times (V - v_i) \times q \times E \quad (2.2)$$

From laboratory experiments conducted by Takahashi et al. (1978) and Saunders et al. (1991) it was shown that rimed graupel particles obtain a net negative charge while ice particles acquire a net positive charge after rebounding collisions, typically at temperatures colder than $-10\ ^\circ\text{C}$. Closely linked with the rate of graupel electrification, is the size of the particle and ultimately the terminal fall velocity. Gravitational sedimentation and differences in the terminal fall velocities between graupel and ice crystals and the addition of vertical motion via a convective updraft often results in the separation of particles and the generation of an electric field. The smaller ice particles are often carried aloft by a sufficiently large updraft. The relatively larger graupel particles typically are not lofted as far in the vertical or in some instances fall back downward towards the surface of the earth. This charge separation results in the generation of an electric field within the convective cloud. As a result of the trajectory of ice crystals and graupel particles, the most common structure observed is the normal dipole in which the higher portions of the convective cloud retains a net positive charge

(associated with ice crystals) and the dominant polarity in the lower portion of the cloud is negative (primarily associated with graupel). This simplified charge structure can be examined in Fig. 2.4 from Williams (2001). Figure 2.4 also illustrates the different types of electrical discharges that are observed. The intracloud (left diagram) flash is associated with a discharge that occurs within the cloud. The cloud-to-ground flash is associated with a discharge that extends from somewhere in the cloud and contacts the ground.

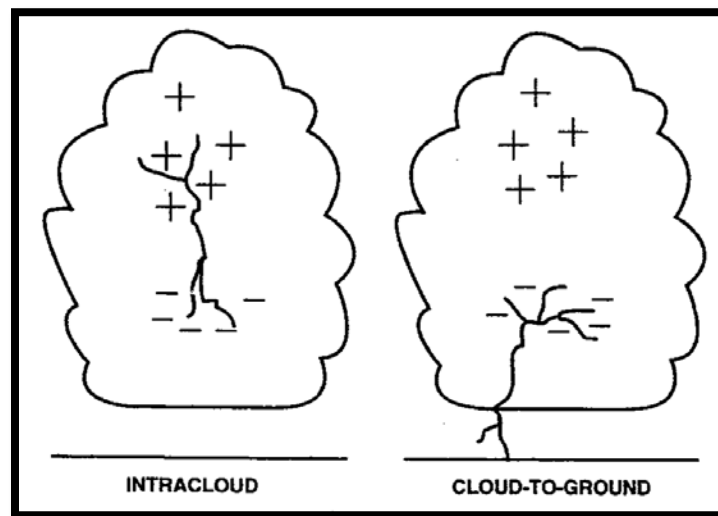


Figure 2.4. Simplified diagram from Williams (2001) showing the various lightning flashes. This image assumes a “normal” polarity storm in which the higher portion of the convective cloud attains a predominantly positive charge (associated with positively charged ice crystals) and the lower portion of the cloud retains a predominately negative charge (associated with negatively charged rimed graupel). From left to right, schematics of an intra-cloud (IC) and cloud-to-ground (CG) flashes.

In some instances, however, the aforementioned hydrometeors can experience a reversal in their acquired charge. This reversal, as noted by Takahashi (1978) and Saunders et al. (1991) has a dependency on both the temperature and/or the liquid water content (LWC). Figure 2.5 from Saunders et al. (1991) denotes that the polarity of the particle responsible for riming is dependent on the temperature and the LWC. In laboratory experiments, Takahashi (1978) observed that at temperatures warmer than -10

°C, the riming apparatus always charged positively regardless of the LWC. In the case of thunderstorms, positive charging of graupel is likely when temperatures are warmer than -10 °C. This so-called reversal temperature has been used to explain the existence of a lower positive charge region below the main normal dipole in DMC. The descent of graupel below the melting layer may be a sufficient means to create this lower charge region as illustrated by Coleman et al. (2008) and MacGorman et al. (2011). Information from Takahashi (1984) and Saunders et al. (1991) suggested that the acquired charge of graupel could change as particles descended to warmer temperatures and/or higher values of LWC. This change in charge acquired could explain the tripole charge structure of a storm during the latter portion of its lifetime. The descent of graupel below the melt layer has been shown to coincide with an increase in the CG lightning flash rate (Carey and Rutledge 1996 and Kuhlman et al. 2006).

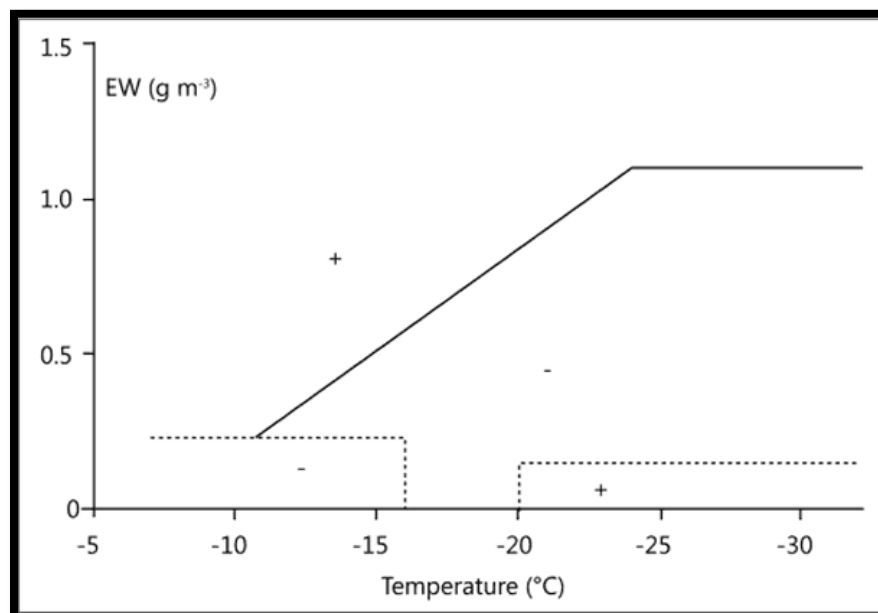


Figure 2.5. Illustration of the charge separated to the riming ice particle during rebounding rimer-ice crystal collisions as a function of the effective liquid water content (g m^{-3}) and temperature ($^{\circ}\text{C}$). The (+) denotes regions of positive polarity while the (-) denotes regions of negative polarity. Adapted from Saunders et al. (1991).

2.4 A Review of Past Studies that examined Microphysical, Kinematic and Lightning Relationships

Numerous observational and numerical studies have examined the relationship between kinematic and microphysical properties of DMC and the resultant electrical behavior of DMC. Most of these studies support the theory of NIC for the electrification of clouds. The use of radar (both reflectivity and polarimetric) has proven to be a useful tool for diagnosing hydrometeors, specifically graupel, within the convective cloud that may be important for NIC, as discussed earlier. Multi-Doppler wind synthesis techniques allow for estimates of vertical motion within DMC. Sufficient vertical motion is necessary for microphysical processes within the mixed phase region. This vertical motion likely leads to the lofting and suspension of liquid hydrometeors upwards into the mixed phase region. Zipser and Lutz (1994) examined midlatitude continental, tropical oceanic and tropical continental convection and suggested that mean updraft velocities of $6-7 \text{ m s}^{-1}$ or maximum updraft velocities of $10-12 \text{ m s}^{-1}$ was sufficient to facilitate cloud electrification. It was theorized that updrafts of these magnitudes were capable of lofting rain into the mixed phase region. While in the mixed phase region, rain would freeze and ultimately grow via riming into graupel and small hail such that they could participate in NIC. Moreover, it was noted that the vertical motion associated with these updrafts was a source for the continual replenishment of supercooled cloud liquid water. Since then, kinematic variables such as the maximum updraft velocity and updraft volume have been explored to try to quantify their role in NIC, as discussed further below.

Carey and Rutledge (1996), Carey and Rutledge (2000), Lang and Rutledge (2002), Wiens et al. (2005), Kuhlman (2006), Deierling and Petersen (2008), Deierling et

al. (2008) have all reported that radar observables (e.g. kinematic or microphysical characteristics) have been shown to trend well with the total lightning flash rate. The most important finding is that ice processes that occur within the mixed phase region (0 °C to -40 °C) are critical to cloud electrification.

Carey and Rutledge (1996), hereafter CR96, examined multicellular DMC across the Colorado Front Range with the polarimetric Colorado State University-University of Chicago-Illinois State Water Survey (CSU-CHILL). CR96 employed a polarimetric-based Boolean logic method to determine a graupel echo volume. Consistent with NIC, the time evolution of graupel echo volume and total lightning flash rate appeared to be well correlated for this DMC across CO. Further, in Carey and Rutledge (2000), referred to as CR00, it was suggested that graupel particles were required for cloud electrification via NIC, *especially in warm cloud base convection*. CR00 examined ordinary single to multicellular DMC across the Tiwi Islands of Australia using a polarimetric C-band radar (CPOL). The use of CPOL enabled CR00 to partition the ice and rain reflectivity into distinct precipitation categories using the difference reflectivity or Z_{dp} method highlighted by Golestani et al. (1989). This method of partitioning the hydrometeors allows for the use of various radar reflectivity-ice mass computations. The radar reflectivity-ice mass in CR00 was computed assuming Rayleigh scatterers took on the form of an inverse exponential size distribution. This will be revisited later. As such, CR00 calculated ice mass within the mixed phase region and it was determined that total ice mass also correlated well with the total lightning flash rate. Finally, both CR96 and CR00 noted that the descent of graupel particles below the 0 °C level was coincident with an increase in the number of CG lightning flashes. As discussed previously, this descent

of graupel particles was thought to result in the generation and enhancement of a lower positive charge region.

Wiens et al. (2005) examined a tornadic supercell thunderstorm during the Severe Thunderstorm Electrification and Precipitation Study (STEPS) across the High Plains of Kansas and Colorado. Polarimetric information from the CSU-CHILL and NCAR S-Pol radars permitted the use of a fuzzy logic based hydrometeor identification algorithm (Vivekanandan 1999; Straka et al. 2000) during this study. With the addition of the National Weather Service Weather Surveillance Radar-1988 Doppler (WSR-88D), triple Doppler wind synthesis was performed. As a result, both kinematic and microphysical behavior could be compared to that of lightning. Wiens et al. (2005) also benefited from the use of a LMA in which detailed information on the structure of total lightning could be examined. More specifics about LMA systems will be addressed later. Similar to CR96, the results from Wiens et al. (2005) concluded that the graupel echo volume and total lightning flash rate were well correlated. From the multi-Doppler wind synthesis, it was also noted that the updraft volume greater than 10 m s^{-1} correlated well with the total lightning flash rate. Correlation coefficients of 0.95 were observed for graupel echo volume and total lightning flash rate, as well as updraft volume greater than 10 m s^{-1} and total lightning flash rate. Kuhlman et al. (2006) simulated the tornadic supercell thunderstorm that was observed by Wiens et al. (2005), and reproduced similar correlations between the graupel echo volume and updraft volume greater than 10 m s^{-1} with the total lightning flash rate. In addition, Kuhlman et al. (2006) showed that the updraft mass flux also correlated well with the total lightning flash rate. Kuhlman et al. (2006) noted that the maximum updraft velocity was not well correlated with the total

lightning flash rate for the tornadic supercell thunderstorm. Similar to CR00, Kuhlman et al. (2006) observed that the CG lightning flash rate typically increased as graupel descended to lower altitudes. Both studies hypothesized that the formation of a lower charge region was necessary for the increase in the CG lightning flash rate. The descent of graupel below the melting layer is thought to be a sufficient means to create this lower charge region (Coleman et al. 2008; MacGorman et al. 2011). Furthermore, Wiens et al. (2005) and Kuhlman et al. (2006) theorized that the increase in the *positive* CG lightning flash rate was a result of continued NIC at lower altitudes.

Deierling and Petersen (2008) noted that lightning can be used as an accurate measure of the updraft intensity. Similar to Kuhlman et al. (2006) the maximum updraft velocity did not *consistently* correlate well with the mean total lightning flash rate. Deierling and Petersen (2008) also examined the relationship between updraft volume and mean total lightning flash rate. In the dataset, there were a total of 11 storms from a couple of regimes; the High Plains and the Southeastern U.S. Sensitivity studies examining the updraft volume greater than 0, 5, 10, and 20 m s⁻¹ above the -5 °C level revealed that the updraft volume greater than 5 and 10 m s⁻¹ correlated the best with the mean total lightning flash rate. The updraft volume greater than 5 m s⁻¹ and 10 m s⁻¹ had correlation coefficients of 0.93 and 0.92, respectively. The correlation seemed regionally invariant and for this reason, it would appear that this kinematic and electrical relationship is robust. Finally, Deierling et al. (2008) showed that the mean total lightning flash rate was also well correlated with the so-called flux product of hydrometeors within DMC. The flux product is computed by taking the product of the upward mass flux of ice crystals and the downward mass flux of graupel particles. After identifying hydrometeor

types with a fuzzy logic algorithm, masses of both ice crystals and graupel particles are computed using radar reflectivity-ice mass relationships that were developed by Heymsfield and Palmer (1986) and Heymsfield and Miller (1988). According to the flux hypothesis, particles charged via the NIC mechanism would ultimately separate due to differences in terminal fall velocities. A key component of the NIC is the generation of a sufficiently large electric field necessary for breakdown. The generation of this field is dependent on the ability to separate the charge of the different polarity hydrometeors. This flux hypothesis was tested on 11 storms across the CO/KS high plains and northern AL. From this observational study, it was shown that the flux product correlated well with the mean total lightning flash rate with a correlation coefficient of 0.96 for this dataset.

Following the results of the radar studies, Barthe et al. (2010) simulated total lightning flash rates in a cloud resolving model without explicit cloud electrification by utilizing six different parameterizations between simulated kinematic and microphysical properties and lightning. The six properties included the maximum updraft velocity, the precipitation ice mass, the cloud top height, the ice mass flux, the ice water path, and the updraft volume. A multicell thunderstorm that evolved into a supercell thunderstorm during the STERAO experiment and a weak multicell thunderstorm from northern AL were both simulated. The early stages of the multicell exhibited flash rates on the order of 10-30 min^{-1} , but then increased to 40-50 min^{-1} during the supercell phase. The DMC across northern AL was not as vigorous from a flash rate standpoint. The peak flash rates with the DMC across northern AL were generally less than 5 flashes min^{-1} . It was found in this study that the maximum updraft velocity had the highest correlation with the total

lightning flash rate ($\rho = 0.80$) while the updraft volume had the worst ($\rho = 0.38$). Interestingly, this result is in opposition to results from Kuhlman (2006) and Deierling and Petersen (2008).

2.5 Thesis Objective and Hypothesis

The purpose of this section is to discuss the objectives and hypothesis of this thesis as it pertains to the DC3 field experiment. Analysis of radar and lightning data is important in order to assist in the determination of a radar inferred microphysical and/or kinematic quantity and total lightning flash rate relationship. As mentioned in section 2.4, a radar inferred quantity total lightning flash rate is desired in order to help parameterize numerical cloud models that are unable to explicitly simulate lightning. The relationships developed in this study will aid in parameterization of these models.

This study will examine five convective cell complexes on four case days during the field phase of DC3 over the AL domain. The four case days to be analyzed include 18 May 2012, 21 May 2012, 11 June 2012, and 14 June 2014. A detailed synopsis of environmental conditions that resulted in the mode and morphology of DMC will be presented. The co-evolution of the kinematics, microphysics and electrical behavior of DMC will be explored thoroughly with the aid of polarimetric and multi-Doppler data collected. Polarimetric radar data will be used to develop quantitative relationships between radar inferred quantities and the total lightning flash rate. This study will examine differences between a bulk hydrometeor volume-total lightning flash rate relationship and mass specific-total lightning flash rate relationship. For this study, the bulk hydrometeor volume will be comprised of the graupel/small hail echo volume. For

brevity, the graupel/small hail echo volume will be referred to simply as the graupel echo volume. The mass specific quantity will be the graupel mass. The studies discussed in section 2.4 would suggest that the graupel echo volume will trend better with regards to the evolution of the total lightning flash rate. A robust correlation is expected between graupel echo volume and graupel mass with the total lightning flash rate due to graupel's role in NIC. While this particular study will be confirmatory in nature, the results presented here will complement those studies highlighted in section 2.4. This study will increase the sample size in which the graupel echo volume-total lightning flash rate and graupel mass-total lightning flash rate relationships can be tested. Moreover, this study will seek to understand the utility of dual-polarization radar when diagnosing hydrometeors relevant to NIC to legacy methods of diagnosing hydrometeors (e.g. 30 dBZ echo volume). Furthermore, the evolution of these trends is examined through the development of statistically expressions between a radar observable and the total lightning flash rate. In addition to microphysical inferred relationships, kinematic quantification of DMC during DC3 AL is also desired. The examination of maximum updraft velocity and updraft volume will help to resolve some of the ambiguity between these quantities and the total lightning flash rates discussed in previous studies. As was noted by Barthe et al. (2010), the updraft volume $> 5 \text{ m s}^{-1}$ correlated the worst with the total lightning flash rate. For this study, updraft volumes of varying magnitudes (e.g. 3 or 5 m s^{-1}) are explored in an attempt to gauge the sensitivity across DMC events with varying flash rates.

Finally, empirical radar observable-total lightning flash rate relationships will be developed in an attempt to provide robust expressions that could be used to assist in the

accurate depiction of lightning in numerical cloud models that do not explicitly resolve cloud electrification. The robustness of a given radar observable-total lightning flash rate relationship will be gauged based on the Pearson product moment correlation, the root mean square error, and mean square error. In addition, it is hoped that these relationships developed across DC3 AL provide to be regionally invariant when tested on convection across the NE Colorado or Oklahoma/Texas domains.

CHAPTER THREE

DATA AND METHODOLOGY

This purpose of this chapter is to provide an overview of the DC3 field experiment, discuss quality control procedures performed on radar, radiosonde, and lightning data for the DC3 AL dataset and discuss computations of various radar derived kinematic and microphysical quantities. The experimental design will briefly highlight the study regions, daily operations and platforms used during the field phase. Finally, this section will discuss methods for retrievals of 3-D flow as well as dual-polarization methods of hydrometeor identification and quantification.

3.1 DC3 Experimental Design

The field phase of the DC3 experiment was conducted from 15 May 2012 through 30 June 2012 across three regions. The three study regions were located across northeastern Colorado, central Oklahoma and the western Texas panhandle, and northern Alabama and southern Tennessee. One of the main motivations for the selection of these three sites was the varying convective morphology and thus lightning behaviors (Barth et al. 2012). From the Boccippio et al. (2001) climatological study which examined the geographic distribution of the IC:CG ratio, the CO region would potentially offer the opportunity to study DMC that produces copious amounts of IC in contrast to the relatively low ratio of IC to CG lightning in AL storms. All regions were equipped with dual-polarization radar to document relevant microphysical and kinematic attributes of DMC. With dual-polarization radar, additional information on hydrometeor type and size

can be extracted. This additional information will allow for a detailed examination of the microphysical processes that are theorized to be linked to the cloud electrification process. For electrical observations of DMC, VHF LMAs were also available at all three regions for detailed three dimensional mapping of total lightning activity. Also, the NLDN is a network of LF to VLF sensors that are located across the United States and can be used to identify regions of primarily CG and some IC lightning activity (Cummins and Murphy 2009). While NALMA does allow for detailed mapping of lightning, the NLDN was used principally as the CG return stroke detector. Environmental upper air observations from mobile ballooning facilities aided in characterizing both the pre-convective and near storm environments, as well as offered short-term forecasting support for the positioning of remote sensing platforms. Aircraft observations were conducted via the National Aeronautical and Space Administration's (NASA) Douglas DC-8 research aircraft and the National Center for Atmospheric Research's (NCAR) GulfStream (GV) research aircraft. The NASA DC-8's primary role was to sample within the PBL in order to sample environmental inflow into DMC. The NCAR GV was tasked with sampling the upper level flow to sample an array of gases and cloud particles found in the convective anvil. Radiation processes associated with DMC were also examined. The NASA DC-8 and NCAR GV were both based out of Salina, KS, the location designated for the operations base. Sampling on any given day at any given site (CO, OK, or AL) was primarily driven by expected weather conditions during the daylight hours. Mission planning typically began around 1300-1330 UTC each day via a teleconference between the operations base and the three sites. A review of the previous day's activities as well as an overall synopsis of major weather patterns across the continental U.S. was

provided. Each region designated forecasters to provide a more detailed synopsis and convective forecast for their respective regions to aid mission planners. Chemical forecasts were furnished by both NASA and NCAR scientists using the Weather Research & Forecasting (WRF) model. Finally, status updates of all equipment used in the experiment were provided. Based on anticipated weather forecasts and region readiness, a decision to deploy aircraft to a given region was made. It should be noted that the lack of aircraft did not preclude a given site from conducting its own independent ground operations.

3.2 DC3 Alabama Domain

The observational network that comprises DC3 AL consists of multiple polarimetric weather radar, a VHF LMA, the LF/VLF NLDN and a mobile ballooning vehicle for environmental radiosonde observations. There are three polarimetric weather radars across northern AL: 1) the WSR-88D located at Hytop, AL (KHTX), 2) the Advanced Radar for Meteorological and Operational Research (ARMOR) located at the Huntsville International Airport (KHSV) and 3) the Mobile Alabama X-band Radar (MAX). A map of the DC3 AL domain including VHF LMA (excluding the 2 north GA points [not shown]), the location of radars, and multi-Doppler regions can be viewed in Fig. 3.1

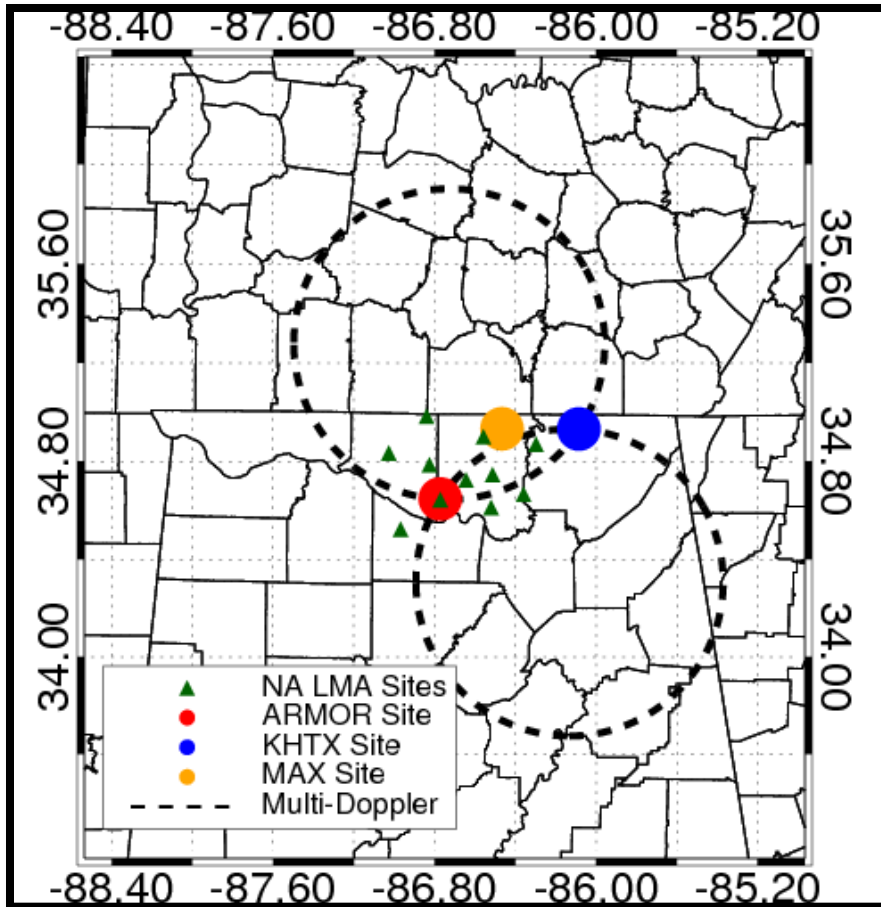


Figure 3.1. Map of the AL domain during the DC3 field project. The solid red circle represents the location of the ARMOR radar at KHSV. The solid orange circle represents the location of the MAX radar at New Market, AL. The solid blue circle represents the location of KHTX at Hytop, AL. The green triangles show the location of NALMA sensor locations. Note that the northern GA sites are excluded. The dashed lines represent the ARMOR-KHTX multi-Doppler regions

3.3 Overview of the ARMOR and KHTX radar platforms

KHTX is a S-band (10.71 cm) polarimetric radar (upgraded 1 Jan 2012 [NWS Radar Operations Center, 2013]) and is located across portions of rural Jackson County, AL, in the northeastern portion of the state). It operates in a simultaneous slant 45° transmit and receive of the horizontal and vertical channels. The approximate beamwidth of KHTX is around 1° . The variables that are available from KHTX include the

horizontal radar reflectivity (Z_h), Doppler velocity (V_r), spectrum width (σ_{sw}), differential radar reflectivity (Z_{dr}), the co-polar correlation coefficient (ρ_{hv}), and the specific differential phase (K_{dp}). For the purposes of this study, Z_h , Z_{dr} and ρ_{hv} are the variables most often used. Hall et al. (1984) define Z_{dr} as the logarithmic ratio between the horizontal and vertical polarized channels. The value of Z_{dr} increases with an increase in the axis ratio (b/a) of the particle. Lastly, ρ_{hv} measures the similarity in the behavior between the horizontally and vertical polarized waves across a radar sample volume (Bringi and Chandrasekar 2001). In the case of uniform hydrometeors, ρ_{hv} approaches unity. In the instances of mixed hydrometeors, ρ_{hv} may decline. Melting of hailstones can also result in the suppression of ρ_{hv} , especially at the shorter weather radar wavelengths (Anderson et al. 2011). While explicit control of KHTX's scan strategy rested with NWS officials, it was often requested that volume coverage pattern (VCP) 11 or 12 (and associated 212 or 211) be implemented during intensive operations for DC3 AL. VCP (2)11 and (2)12 offer update times on the order of 5 minutes. According to the Warning Decision Training Branch (WDTB) the latter VCP's offer superior volumetric scanning of DMC when compared to VCP 21 or 31/32 strategies (WDTB, 2013). For more detail regarding NWS VCP's, please examine Table B.1 in the appendix. KHTX has a maximum range of around 230 km. The WSR-88D operates in continuous 360° surveillance at fixed elevation angles. As such only plane position information is available. In precipitation mode, the WSR-88D has an approximate pulse length of 1.57 μ s.

ARMOR¹ is a C-band (5.5 cm) polarimetric radar that is located at the Huntsville International Airport (KHSV). ARMOR is co-owned by the University of Alabama in Huntsville (UAH) and WHNT-TV in Huntsville, AL (Petersen et al. 2005). Similar to KHTX, ARMOR operates in a slant 45° simultaneous transmit and receive of the horizontal and vertical channels. The approximate beamwidth of ARMOR is around 1°. The number of samples from ARMOR is typically between 56 and 64 samples with a usual radar pulse length of around 0.8 μs. The variables that are available from ARMOR include Z_h , V_r , σ_{sw} , Z_{dr} , ρ_{hv} , ϕ_{dp} , and K_{dp} . For ARMOR, K_{dp} is computed using a method outlined in Hubbert and Bringi (1995) and Bringi et al. (2001).

MAX² is a mobile X-band (~ 3 cm) polarimetric radar. As a result of the complex terrain and vegetation across northern AL and southern TN, MAX was usually deployed to an open field located at New Market, AL (34.932213, -86.466339). New Market, AL is approximately 42 km NE of ARMOR and 35 km W of KHTX. It operates in a simultaneous transmit and receive of the horizontal and vertical channels. The approximate beamwidth of MAX is around 0.95°. The number of samples from MAX is typically between 56 and 64 samples with a typical radar pulse length of around 0.8 μs. The variables from MAX are Z_h , V_r , σ_{sw} , Z_{dr} , ρ_{hv} , ϕ_{dp} , and K_{dp} .

The scan strategies of ARMOR and MAX were both tuned so that specific goals of DC3 were met. With a keen interest on examining upper level outflow (e.g., the anvil), ARMOR and MAX scan strategies each consisted of relatively high maximum up angles (highest around 26.8°). Additional information in tabular form for the ARMOR and

¹ For additional information on the Advanced Radar for Meteorological and Operational Research (ARMOR) please visit www.armor.nsstc.uah.edu/about.php

² For additional information on the Mobile Alabama X-Band (MAX) Radar please see www.vortex.nsstc.uah.edu/mips/max

MAX scan angles are listed in Table B.2. During DC3 both ARMOR and MAX had effective scan ranges of approximately 125 km, although the practical usable range of MAX was often significantly less (e.g., 50 km) due to severe propagation effects in heavy precipitation at X-band (Bringi and Chandrasekar 2001). Also during DC3, both radars operated in three primary modes: 1) a continuous 360° surveillance at fixed elevation angles, 2) sector volume scans with a defined range of azimuths at fixed elevations (SV) or 3) at a fixed azimuth with varying elevation angles (RHI). The continuous 360° surveillance at fixed elevation angles was implemented before convective initiation to characterize the PBL or if widespread convection was ongoing. The SV scan strategy was implemented when aircraft were sampling DMC, when the DMC was particularly robust and/or when the DMC was isolated. Finally, the RHI sampling strategy was implemented for DMC that was close in range to radars. The RHI scan offers a high temporal observation of the vertical structure of DMC. This study will focus on radar data from ARMOR and KHTX. These radars (ARMOR and KHTX) provide the best continuous and complete record of the three-dimensional structure and lifecycle of DMC with less impact of both propagation effects and velocity unfolding.

3.4 Overview of the North Alabama Lightning Mapping Array

The North Alabama 3-D Lightning Mapping Array (NALMA) is owned and operated by officials at NASA's Marshall Space Flight Center (NASA MSFC) in Huntsville, AL. NALMA consists of 11 VHF sensors across northern AL and 2 VHF sensor in north central GA. NALMA's center is located at the National Space Science and Technology Center (34.72 -86.64) in Huntsville, AL (Koshak et al. 2004; Goodman et al. 2005). A VHF LMA detects the electrical breakdown associated with the large

electric field near the tip of a self-propagating leader. This electrical breakdown emits radiation in the VHF range that is readily detectable by time-synchronized sensors. NALMA sensors have a maximum sampling window of around 80 μs in which the peak pulse in radiation, in the VHF range, emitted is recorded. A point “source” of electrical breakdown associated with the tip of a self-propagating leader is detected. These self-propagating leaders emit radiation in the VHF range. Operating on a line-of-sight basis, a time-of-arrival technique (TOA) is employed to determine the position of each individual source. Cummins and Murphy (2009) noted that this TOA technique required time-synchronization of sensors (typically six for sufficient redundancy and hence accuracy). Koshak et al. (2004) found that typical horizontal and vertical spatial errors of NALMA detected VHF sources was on the order of 100s of meters within 150 km from the network center. At ranges in excess of 300 km from the center of the network, these errors increase by an order of magnitude. All cases analyzed during DC3 were within 90 km of the center of NALMA.

3.5 Overview of the National Lightning Detection NetworkTM (NLDN)

The NLDN is a national lightning network across the U.S. that operates at the LF to VLF range. This network has over 100 sensors across the U.S. and has existed for over 25 years. Cummins et al. (1998) and Biagi et al. (2007) noted that the median spatial accuracy error associated with return strokes was around the 200-500 meter range. Return strokes are associated with the transfer of charge after a leader has generated a conductive path between charge regions (e.g. the cloud and the ground). Once the connection between the two charge regions occurs, rapid transfer of charge occurs. This bright luminous phenomenon represents the return stroke (Rakov and Uman 2003) in which

charge is being drained from the cloud through the ionized channel. This large amount of current flow is detected via LF to VLF sensors. Vaisala estimates that the ability to detect a lightning flash across the continental U.S. and surrounding waters to be approximately 95% (Cummins et al. 2006; Cummins and Murphy 2009). Utilizing enhanced campaign observations of lightning, Biagi et al. (2007) found similar flash detection efficiencies of about 92% to 93% in different locations within the continental United States. Detection methods are a combination of TOA and magnetic direction finding (MDF) techniques. Return strokes are then clustered into flashes based on spatial and temporal proximity to the first return stroke. Details on this clustering process will be discussed further in subsequent sections.

3.6 Comments about the Radiosonde Operations

Routine upper air observations were available from the NWS offices in Birmingham, AL (WFO BMX), Nashville, TN (WFO OHX), and Peachtree City, GA (FFC). These observations were made twice daily at 1200 and 0000 UTC. The Redstone Arsenal U.S. Army base located near Huntsville, AL, provided semi-routine upper observations at 1200 UTC, Monday through Friday. These observations were useful as they provided information on the pre-convective environment the morning of possible operations. Finally, the mobile ballooning vehicle operated by UAH performed upper air observations in order to characterize the pre-, near-, and post-convective environment. Due to the complex vegetation and terrain across northern AL and southern TN, predetermined locations at which upper air releases were to take place were identified several weeks in advance of the intensive operations period for DC3 AL.

3.7 ARMOR and KHTX data

The quality control procedure for ARMOR and KHTX is exhaustive in an attempt to ensure the highest data quality possible. As a result of ARMOR's wavelength (~5.5 cm), propagation effects due to the presence of liquid precipitation, including rain, large rain drops and/or melting hailstones must be corrected. To address this issue, the "raw" ARMOR data collected during DC3 is corrected for attenuation and differential attenuation utilizing a self-consistency method that is outlined in Bringi et al. (2001). This process allows for the correction of reflectivity data in both horizontal and vertical polarizations that may become partially attenuated due to large oblate hydrometeors. KHTX is not corrected for propagation effects owing to its relatively larger wavelength. It should be noted, however, that attenuation and differential attenuation can occur at S-band in the instances of large melting hail and heavy precipitation systems. In the latter instance, the echoes associated with these heavy precipitation systems may occur directly over the radar resulting in a slightly attenuated signal. No such events occurred for the data examined for DC3 AL.

After correction for propagation effects were completed on ARMOR, the next step was to remove ground clutter and 2nd trip echo near convective cells of interest. This was performed using NCAR's SOLOii radar visualization and editing tool. Ground clutter was readily identified using a combination of V_r and ρ_{hv} . Ground targets are stationary and result in a near 0 m s⁻¹ Doppler velocity. Ground targets also often produce low values in ρ_{hv} (typically less than 0.8) (Torres et al. 1998). Using the two aforementioned parameters in tandem, ground clutter near precipitation echoes was removed. The removal of 2nd trip echo proved to be slightly more cumbersome as the 2nd

trip echoes are associated with true returns beyond the maximum unambiguous range. Typically associated with 2nd trip echoes are erroneous Doppler velocities. As a result, the 2nd trip echoes were removed where the V_r field appeared erratic and discontinuous. Intuitively, the removal of 2nd trip echo and ground targets near precipitation echoes must be performed to ensure accurate estimates of vertical motion via multi-Doppler retrievals as well as for proper identification of hydrometeors using the NCAR PID. Information on both of these techniques will be highlighted shortly. Doppler velocities for ARMOR and KHTX were also manually dealiased. This technique is subjective in nature and is deemed successful by the user of the data. In most instances, visual inspection was the best method to guarantee that Doppler velocity fields were homogenous. While this task is quite labor intensive, it is important as this information is used in retrievals of vertical motion. Both ARMOR and KHTX radar data were gridded using the NCAR REORDER (Oye et al. 1995) software package. This study uses a Cressman Weighting (Cressman 1959) scheme to grid the radar data. The radius of influence was set at 1.0 km x 1.0 km x 1.0 km with grid spacing of 1.0 km x 1.0 km x 1.0 km. All radar data are gridded with ARMOR being the origin of the grid.

The multi-Doppler wind retrievals were obtained via the Custom Editing and Display of Reduced Cartesian Space (CEDRIC) (Miller and Frederick 1998). The multi-Doppler wind synthesis techniques presented here will be used to document the kinematic structure of DMC. The velocity information will also then be available to the modeling community to verify output from numerical simulations of ordinary, multicellular DMC. Multi-Doppler regions are those characterized as having two or more radars in which vertical air motions can be derived. The region in which the maximum range and the

beam-cross angle constraint of 30° overlaps (Davies-Jones 1979). For the case of only two radars, the use of the radial velocity information from each radar in conjunction with the anelastic form of the mass continuity equation, and an assumption of a terminal fall velocity for precipitation are used (Armijo 1969). For each case day, the storm motion vector was determined using the Gibson Ridge Radar Software. This storm motion was then the input used in CEDRIC in the advection correction scheme. In order to perform a multi-Doppler wind synthesis, there were a few criteria that the data needed to meet in order to be deemed fit for the procedure. 1) Radar data between ARMOR and KHTX needed to have no more than a 2-3 minute offset, 2) the entire precipitation echo (through at least 10-15 dBZ at storm “top”) needed to be sampled within the aforementioned multi-Doppler region and 3) Doppler velocities were dealiased properly. CEDRIC also utilizes a terminal fall velocity that aids in the determination of the true vertical motion. Initially it is assumed that the air motion (not including the terminal fall velocity) is zero. As such the U and V components of the air are computed using the terminal fall velocity. Upon the re-computation of U and V, the anelastic form of the mass continuity equation is integrated using a variational scheme. This variational scheme is thought to reduce errors associated with the accumulation of divergence errors when integrating the mass continuity equation (Gao et al. 1999). Gao et al. (1999) presented results from a supercell thunderstorm and concluded that the variational method could still have utility even if the entire echo volume is not sampled in its entirety. While errors still occur, Gao et al. (1999) note that this method is superior to the upward or downward integration techniques. If sampled properly, the downward technique can be employed and should yield results similar to that if the variational scheme is employed. The upward technique

does not yield realistic results due to sampling limitations of weather radar. In many instances, a sufficient amount of the lowest portion of the storm is not sampled. As a result, the lower boundary condition is ambiguous. The variational method is preferred as it is thought to better redistribute error from both the upper and lower boundary conditions. This “averaging” between errors associated with the two boundary conditions should dampen out any large errors associated with this technique. Due to the radar scan strategy employed during DC3, the entire echo associated with most observed DMC was sampled. Figure A.1 shows results from a sensitivity study when comparing the two methods (variational and downward integration).

It should be noted that errors in multi-Doppler wind retrievals likely occurred during the 18 May 2012 event. Convective complex A1 was roughly 20-30 km north of ARMOR and exhibited rapid vertical growth. Due to the close range, the upper boundary conditions of A1 were inadequately sampled. In this event, maximum echo tops were closer to 30 dBZ. While trends in the evolution of the kinematic information appear reasonable, it is likely that the peak magnitudes of upward vertical motion are an underestimate due to the ambiguity at the upper boundary condition. Similarly, the close range of convection to KHTX (20-30 km) and VCP implemented on KHTX, hampered the ability to provide estimates of vertical motion from multi-Doppler wind synthesis on the 14 June 2012 case (convective complex D1). During this time period, maintenance being performed on KHTX required the use of VCP 21 and VCP 32. Both of these VCPs severely limit the ability for KHTX to sample DMC on an acceptable temporal and spatial scale for multi-Doppler wind synthesis. Accordingly, results from the multi-Doppler wind synthesis on the 14 June 2012 case day are not reported due to the

suspected error. As such, for comparison of kinematic properties of DMC, the number of case days decreases from four to three.

3.8 Overview of C-Band NCAR PID

The NCAR PID is an algorithm that utilizes fuzzy logic to determine hydrometeor type. Fuzzy logic is necessary when determining hydrometeor type as there is often some ambiguity between polarimetric signatures between two or more categories (e.g. mixtures of similar hydrometeors) (Vivekanandan 1999; Straka et al. 2000). Seventeen (14 meteorological and 3 biological) different categories are available for the C-band version of the NCAR PID and can be viewed in Table B.3. For this study, the graupel/small hail category was used nearly exclusively. In order to account for the shorter wavelengths and the fact that ARMOR operates in a simultaneous transmit and receive of the horizontal and vertical channels (LDR is unavailable), the version of the PID used in this study was particularly modified for ARMOR by Deierling et al. (2008) (modified in the sense that membership functions were changed). This version of the NCAR PID has equivalent weightings for the temperature (derived from environmental soundings), Z_h and Z_{dr} . Each of these three categories are weighted at 20%. The remaining categories, K_{dp} , ρ_{hv} , and the standard deviations of Z_{dr} and ϕ_{dp} are weighted each at 10%. The changes for the membership functions are primarily to Z_h and Z_{dr} . These modifications shift the minimum values of Z_h and Z_{dr} upward (from 25 dBZ to 33 dBZ) for the Moderate Rain, and any Hail or Graupel category. Also, thresholds for ρ_{hv} were lowered to account for the resonance at C-band associated with melting hail and large raindrops.

3.9 Quality control of NALMA and NLDN data

NALMA data is downloaded from each VHF antenna site (Fig 3.1) during periods of inactive weather. As noted in section 3.4, the spatial errors associated with VHF sources detected within 150 km from the center of NALMA (NSSTC 34.72, -86.64) is estimated to be on the order of 100s of meters (Koshak et al. 2004). All convective episodes in this study were within this 150 km range. There are several algorithms that can be used for VHF source clustering. For this study, the McCaul VHF source clustering algorithm was preferred as this algorithm was designed specifically for NALMA (McCaul et al. 2005; McCaul et al. 2009). The McCaul VHF source clustering algorithm takes into account distance from NALMA center when clustering VHF sources. Within 50 km of the center of NALMA, the algorithm requires a 0.3 s time interval between successive sources to be adjoined together as a single flash. McCaul et al. (2009) and Gatlin and Goodman (2010) state that a 0.05 radian bound is applied to sources based on expected azimuthal errors. These temporal and spatial criteria become more stringent at greater distances from the center of the LMA due to the decrease in detection efficiency with range. For example, McCaul et al. (2009) and Gatlin and Goodman (2010) note that at 100 km, successive sources can be no more than 5 km apart due to uncertainty in position. While filtering of noise points is inherently done during this clustering process, additional constraints are applied to remove any noise that is not filtered out. Murphy (2006) noted that the number of sources necessary for a flash can impact the flash count (and resultant flash rate calculations). As a result, sensitivity tests were conducted in order to determine an appropriate criterion for the amount of sources necessary for a flash. Figures A.2 and A.3 summarize these sensitivity studies. These two case events

were chosen given their proximity to the center of NALMA. The 18 May 2012 case event was approximately 20 km from the center of NALMA, while the 11 June 2012 case event was nearly 80 km from the center of NALMA. From these sensitivity studies, it is apparent that varying the source criteria by 5, 10, and 15 VHF sources had negligible impact on the trend of total lightning. More importantly, varying the number of VHF sources had very little influence on the magnitude of the total lightning flash count *for this dataset* due to the low flash rate nature of DMC across DC3 AL. Following Wiens et al. (2005), Murphy (2006), Schultz et al. (2009) and Gatlin and Goodman (2010), the number of VHF sources required to compose a flash was ≥ 10 . It should be stated that there is no upper threshold on the number of sources per flash.

Mentioned previously, the NLDN will be as a detector of CG lightning flashes. Flash data was obtained from Vaisala via the Global Hydrology Resource Center (GHRC) located at NASA's Marshall Space Flight Center. Cummins et al. (1998) notes that because the NLDN detects return strokes across the LF to VLF spectrum associated with CG lightning; a clustering algorithm must be used in order to determine actual CG flashes. This clustering algorithm has spatiotemporal constraints that require subsequent return strokes to occur within 10 km of the first NLDN detected return stroke. In addition, these return strokes must occur within 500 millisecond (ms) of said NLDN detected return stroke to be considered as part of the flash (Cummins et al. 1998). If the return stroke does not meet this criterion, it is considered a different flash. Also, the peak current and polarity reported in the flash data corresponds to that of the first return stroke. While NLDN does attempt to discriminate between IC and CG flashes, Cummins et al. (1998, 2006) and Wiens et al. (2005) recommends that a +15 kA threshold be applied for

positive CG (+CG) flashes. Furthermore, this dataset uses a 15 kA absolute magnitude threshold to determine CG flashes in general, including negative polarity ground flashes (Fleenor et al. 2009).

3.10 Quality control of UAH Mobile Radiosonde Observation Data (RAOB)

A majority of the quality control of the UAH Mobile RAOB data was completed by specialists at NCAR. Techniques that were developed during TOGA COARE that involved both automated and manual inspection of data were employed on DC3 data for all regions (Loehrer et al. 1996). During the automated QC process, six data flags were used. Each flag was encoded with a corresponding numerical value for easy storage in an ASCII file; good (1.0), questionable (2.0), bad (3.0), estimated (4.0), missing (9.0), or unchecked (99.0). The meanings of these encoded values are summarized in a table adapted from Loehrer et al. (1996) in Table B.3. These flags are applied to the pressure, temperature, relative humidity, U and V components of the wind and the change in height between the two successive data points. Vertical consistency checks were also performed to ensure quality data. Data (e.g., temperature and relative humidity) in which pressure increased with time or altitude was marked as questionable or bad. Also, excessive temperature lapse rates and/or unrealistic balloon ascension rates were marked as questionable or bad. Finally, a human element was involved in the quality control process. Visual inspection of all data was performed. If data seemed unrealistic to the human quality control specialist, data could be flagged. Loehrer et al. (1996) provides an exhaustive examination of QC procedures employed during the TOGA COARE. The QC procedures employed during TOGA COARE were similar to those used for the DC3 RAOB dataset.

3.11 Cell Identification and Tracking

Cell identification and tracking was done on a purely subjective basis. Based on personal communication with users of automated cell tracking algorithms, it was decided that the multicellular nature of DMC events across DC3 AL would pose a problem for automated cell tracking algorithms. Problems such as cell “drop out”, merging, splitting and the inability to distinguish between adjacent cells would undoubtedly result in inaccurate microphysical, kinematical, and electrical cell-based computations. As a result, a subjective Lagrangian approach was employed to track the multicellular DMC. In this approach, an analysis box was constructed around the complex of interest and advected in time and a space along with the DMC. Within this analysis box, calculations of various microphysical, kinematic and electrical quantities were performed.

3.12 Calculation of Microphysical, Kinematic and Electrical Quantities

Output from the NCAR PID allows for the explicit calculation of various precipitation masses. In order to apply a radar reflectivity-ice water content (Z-IWC) relationship, information from Table B.4 is used to determine the type of hydrometeor identified by the NCAR PID. The use of a Z-IWC requires that one accounts for the differences in dielectric strengths between water and ice as noted by Smith (1984). Equation 3.1 shows that by taking the product of the ratio of dielectric factors (water $[\text{K}|_w]^2$ and ice $[\text{K}|_i]^2$) and the measured equivalent horizontal radar reflectivity factor (Z_e), one can compute the corrected horizontal radar reflectivity factor (Z_h) [$\text{mm}^6 \text{m}^{-3}$].

$$Z_h = \frac{|K|_w^2}{|K|_i^2} \times Z_e \quad (3.1)$$

The primary method for the calculation of precipitation ice mass in this study uses a Rayleigh approximation following CR00. This method assumes an inverse exponential size distribution for all Rayleigh scatters. Also, an assumption about the slope parameter (N_0), and the density of ice (ρ_i) is also necessary. This study assumed a typical slope parameter of $4 \times 10^6 \text{ m}^{-4}$, a value typically used when examining tropical convection (Petersen 1997). Also, the density of graupel was assumed to approach that of solid ice or 917 kg m^{-3} . The value of Z_e where the NCAR PID determines graupel/small hail between $-10 \text{ }^\circ\text{C}$ to $-40 \text{ }^\circ\text{C}$ layer is then used to compute Z_h following Eqn. 3.1. This value of Z_h (in units of $\text{mm}^6 \text{ m}^{-3}$), is then multiplied by a factor of 10^{-18} such that the appropriate units are satisfied.

$$M_{\text{ice}} = \Sigma \left(x \times y \times z \times \pi \times \rho_i \times N_0^{\frac{3}{7}} \times \left(\frac{1 \times 10^{-18} \times Z_h}{720} \right)^{\frac{4}{7}} \right) \quad (3.2)$$

The product of the grid volume (x, y, z), in meters, and the density of ice, slope parameter and horizontal radar reflectivity yield the ice mass at a given point. For the total precipitation ice mass, the sum of this product is taken. Equation 3.2 shows the complete formulation for the computation of precipitation ice mass.

The hydrometeor echo volume is defined as the product of the count of a given NCAR PID hydrometeor pixel within the $-10 \text{ }^\circ\text{C}$ to $-40 \text{ }^\circ\text{C}$ layer and the three dimensional grid spacing. This value summed across this layer yields the hydrometeor echo volume. Equation 3.3 reveals the formulation for the graupel echo volume in m^3 .

$$\text{Graupel}_{Vol} = \Sigma (x \times y \times z \times \text{Graupel Pixel Count}) \quad (3.3)$$

The updraft volume is defined as the product of the count of a given pixel associated with a given vertical motion value (e.g. 3 or 5 m s⁻¹) within the -10 °C to -40 °C layer and the three dimensional grid spacing. Equation 3.4 reveals the formulation for the updraft volume in m³, in which the W pixel count corresponds to a given threshold for W (e.g. W > 3 m s⁻¹ or W > 5 m s⁻¹).

$$\text{Updraft}_{EchoVol} = \Sigma (x \times y \times z \times W \text{ pixel count}) \quad (3.4)$$

Lightning flash rate calculations were performed by summing the total number of lightning flashes and then dividing by the elapsed radar volume time (in minutes).

CHAPTER FOUR

RESULTS

There are four case days (with four events) that will be examined from an environmental, radar, and electrical perspective. An overview of the environment will include a brief discussion of large-scale synoptic features via archived upper air charts from the Storm Prediction Center (SPC) and an examination of pre-convective radiosonde observations. Tables of important convective parameters for each case day will be provided for each case event examined. Surface features thought to influence convective initiation or morphology will be highlighted. Information on the environment is necessary in order to anticipate and understand the controls on the convective mode. Moreover, numerical models will attempt to accurately simulate identical environmental conditions observed across DC3 AL. This requires a detailed overview of the environment. In general, the AL region could be characterized as one with low to moderate CAPE and deep layer (0-6 km) wind shear environment (less than 1000 J kg^{-1} of CAPE and less than $10\text{-}15 \text{ m s}^{-1}$). The exception to this generalization is the 14 June 2012 case day. This environment could be characterized as one having high CAPE and extremely low deep layer wind shear.

Radar summaries of each convective episode will also be provided. These radar summaries will be used to discuss microphysical and kinematic processes that manifest themselves in polarimetric and Doppler velocity signatures. These signatures will be used to help better understand the microphysical and kinematic controls on electrical

properties of DMC. Qualitative information from computations mentioned in chapter 2 will also be discussed to help bridge the relationships between convective morphology and electrical behavior. This will result in the ability to examine the co-evolution of microphysical, kinematic and electrical behavior. Physical interpretation of the various polarimetric and kinematic signatures and how they relate to electrical properties of DMC will be examined in depth. Quantitative relationships between the total lightning flash rate and radar inferred kinematic and microphysical properties will be established and compared to prior results. Ultimately, these qualitative and quantitative relationships should allow for the parameterization of flash rate in numerical cloud models that do not explicitly include electrification processes.

4.1 18 May 2012 Case Day

4.1.1 Meteorological Overview

The 18 May 2012 case day presented numerous challenges to the forecasting process due to the lack of large scale synoptic forcing. The 1200 UTC upper air charts at 300 hPa and 500 hPa depicted a closed upper low across the Savannah River valley as seen in Fig. 4.1. This resulted in weak northwesterly flow aloft. Also seen in Fig. 4.1, low-level (850 and 700 hPa) winds were light and variable around 5 m s^{-1} . Figure 4.2 provides a comparison between the 1200 UTC RAOB from Redstone Arsenal, AL (KQAG) and the 1800 UTC UAH mobile RAOB. Figure 4.2a depicts the 1200 UTC KQAG RAOB. The 1200 UTC RAOB from KQAG suggested that the low-levels were quite stable with a stout capping inversion within the 1000-920 hPa layer. Information from Fig. 4.2a also revealed that Convective Inhibition (CIN) values around -250 J kg^{-1} .

Above this, however, lapse rates were steep and were generally on the order of $-7.6\text{ }^{\circ}\text{C km}^{-1}$.

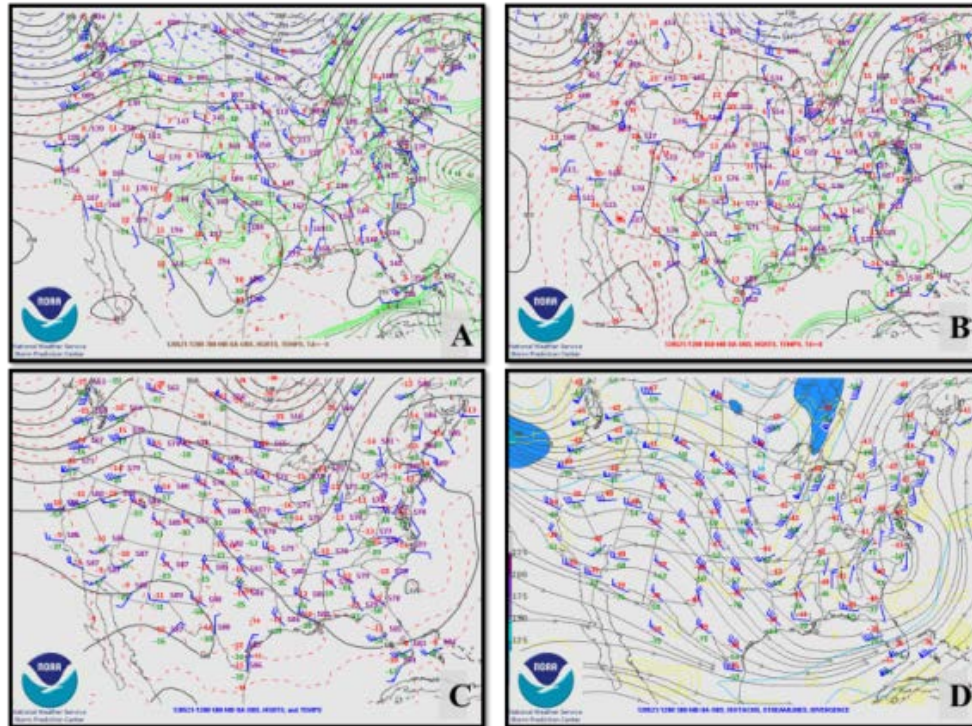


Figure 4.1. 1200 UTC objective upper air analysis from the NOAA Storm Prediction Center. Panel A represents the 700 hPa pressure surface, Panel B represents the 850 hPa pressure surface, Panel C represents the 500 hPa pressure surface and Panel D represents the 300 hPa pressure surface.

The capping inversion limited convection across the TN valley through the afternoon hours. Sufficient solar insolation and boundary layer mixing resulted in steep low-level lapse rates as evident by the 1800 UTC UAH mobile RAOB (Fig. 4.2b) from near Fayetteville, TN. The solar insolation resulted in an increase in the amount of surface based CAPE (SBCAPE). Per the 1800 UTC UAH mobile RAOB, SBCAPE values were around 1270 J kg^{-1} . Deep layer wind shear was very weak, with values less than 5 m s^{-1} on this case day. The environmental $0\text{ }^{\circ}\text{C}$ level was located around a height of 3.5 km. A listing of important environmental parameters can be found in Table 4.1.

Table 4.1. A summary of convective parameters for the 18 May 2012 case day from the 1800 UTC UAH mobile RAOB. The RAOB was taken at Fayetteville, TN.

Convective Parameter	Value
850-700 hPa lapse rate	-7.4 °C km ⁻¹
850-500 hPa lapse rate	-5.6 °C km ⁻¹
SFC-3 km lapse rate	-9.3 °C km ⁻¹
SBCAPE	1270 J kg ⁻¹
SBCIN	0 J kg ⁻¹
DCAPE	950 J kg ⁻¹
Lifted Index	-3 °C
0-6 km shear	3.2 m s ⁻¹
0 °C level	3.5 km
-10 °C level	4.4 km
-40 °C level	9.2 km

The 1800 UTC UAH mobile RAOB also resembled similar traits to that of a Miller type IV or inverted-V sounding. It is thought that sufficient boundary layer mixing resulted in a near dry adiabatic lapse rate and a near constant profile of moisture in the lowest 200 hPa. This RAOB suggested that downdraft CAPE (DCAPE) values were just below 1000 J kg⁻¹.

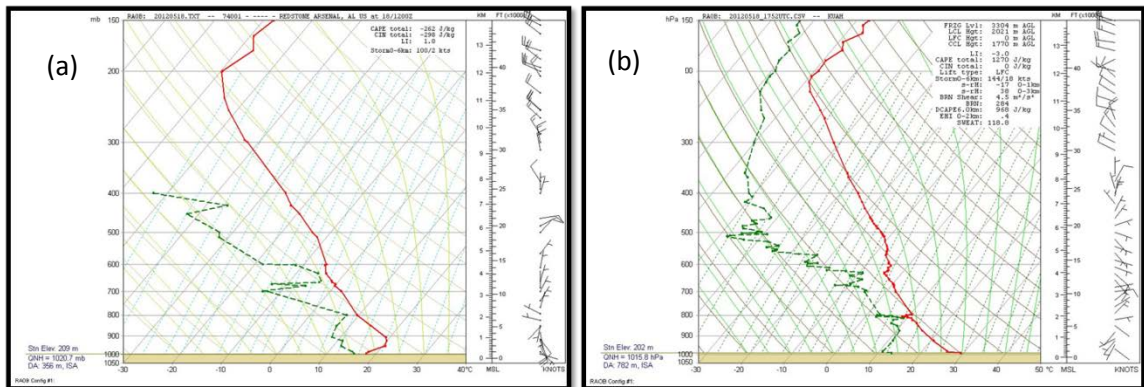


Figure 4.2. Comparison of 1200 UTC RAOB from Redstone Arsenal, AL (a) on 18 May 2012 and 1800 UTC UAH (b) mobile RAOB taken from Fayetteville, TN.

Differential heating along the Cumberland Plateau was evident based on the presence of a cumulus field from satellite imagery (not shown). 850-700 hPa lapse rates from the 1800 UTC UAH mobile RAOB were nearly the same as those observed from KQAG with values on the order of $-7.4 \text{ }^{\circ}\text{C km}^{-1}$. By 2000 UTC, the Rapid Refresh (RAP) mesoanalysis (not shown) suggested that SBCAPE values approached 1500 J kg^{-1} across DC3 AL. This increase in SBCAPE was coincident with the generation of scattered DMC across southern TN and northern AL. From KHTX, precipitation echoes around 2000 UTC were widespread and weak across the TN valley with 10 dBZ radar storm tops generally below 10 km (not shown). Through 2200 UTC, DMC across the region intensified and 10 dBZ echo tops extended up to 12 km at this time. Of particular interest were the convective cells located 10-15 km north of the ARMOR site. As these convective cells decayed, their downdrafts generated an outflow boundary (OFB). Given the DCAPE values, DMC on this case day was efficient at producing numerous OFBs. Enhanced low-level convergence along the OFB generated by decaying cells resulted in the birth of complex A1. As depicted in Fig 4.3, the first echoes of A1 initiated approximately 20 km north and 5 km west of ARMOR just after 2200 UTC.

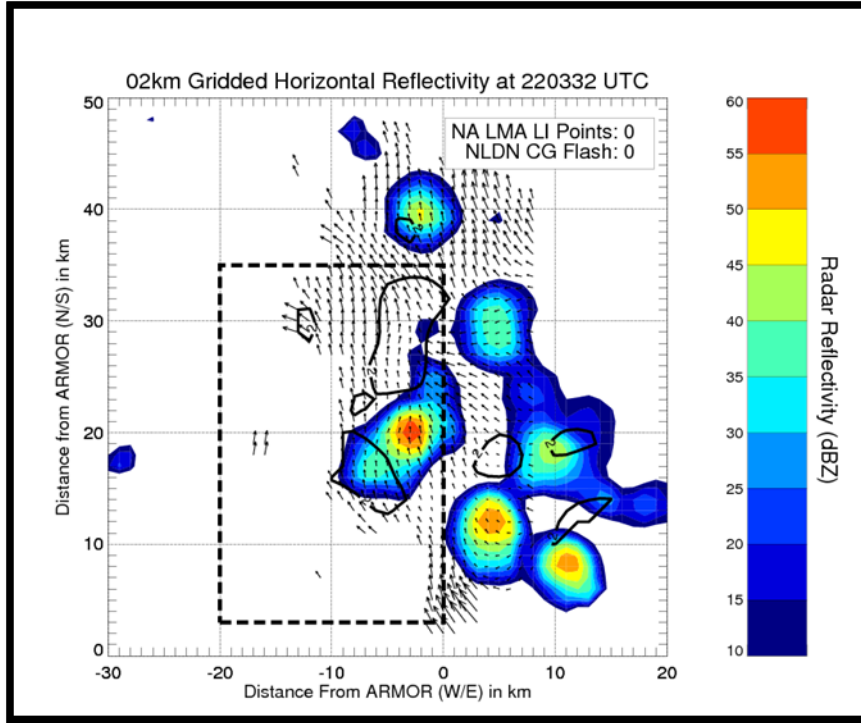


Figure 4.3. Constant Altitude Plan Position Indicator (CAPPI) at 2 km from ARMOR at 2203 UTC. Contour filled image represent Z_h in dBZ and solid lines represents the vertical motion field in intervals of 2, 5, 10, 15, 20, and 25 m s^{-1} . Horizontal wind vectors are plotted.

4.1.2 Developing Phase of Complex A1 2203-2211 UTC

During the first 5-7 minutes of its lifecycle, A1 showed no sign of lightning per NALMA or NLDN observations despite the presence of precipitation ice particles (e.g. graupel). The 3 km CAPPI from the 2203 UTC ARMOR (Fig. 4.4) volume reveal that maximum Z_h values were around 60 dBZ below the 0 °C level (3.5 km).

The ARMOR PPI during the 2203 UTC radar volume revealed that corresponding values of ρ_{hv} were as low as 0.85 (Fig. 4.5a) around 3 km. The combination of the high Z_h , high Z_{dr} and low ρ_{hv} values suggested a diversity of millimeter sized liquid and frozen hydrometeors. As highlighted by Hall et al. (1984), the large Z_{dr} values, shown later in this subsection at the 2203 UTC ARMOR volume, suggested large oblate particles.

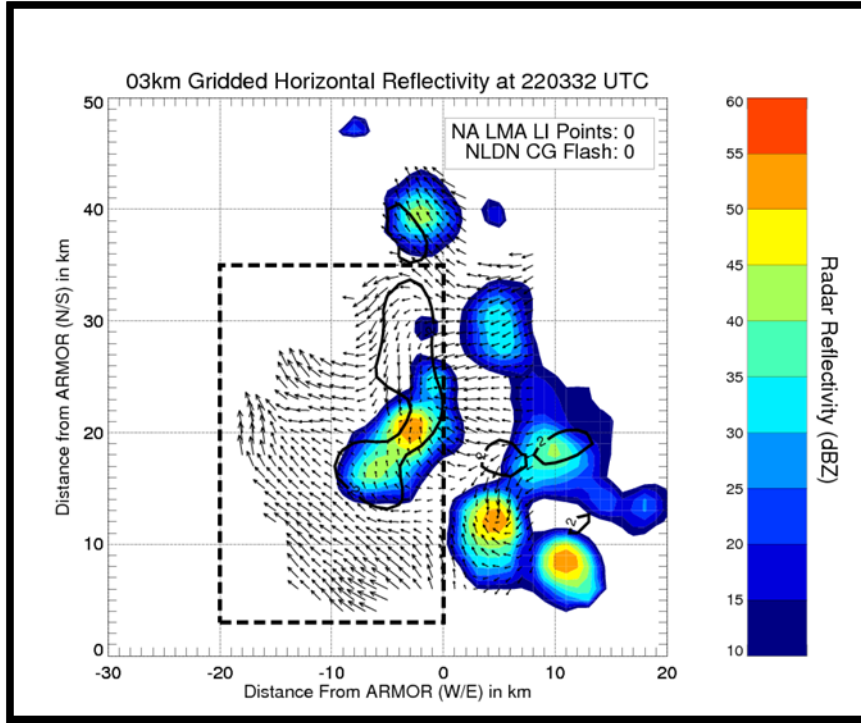


Figure 4.4. CAPPI at 3 km from ARMOR at 2203 UTC. Contour filled image represents Z_h in dBZ and the solid lines represent the vertical motion field in intervals of 2, 5, 10, 15, 20, and 25 m s^{-1} . Horizontal winds are plotted.

As noted previously, large liquid hydrometeors are typically more oblate owing to the drag and gravitational forces along the major axis. This deformation of a water drop results in the increase in the axis ratio. As a result, Z_{dr} increases for larger liquid hydrometeors. Collision and coalescence of rain drops was the dominant factor that resulted in the increase in the size and number concentration of large rain drops. Enhancements in Z_{dr} can also be attributed to the melting of hail stones. Rasmussen and Heymsfield (1987) and Anderson et al. (2011) noted that a water shell can accumulate along the surface of melting hail stones which increases the value of Z_{dr} .

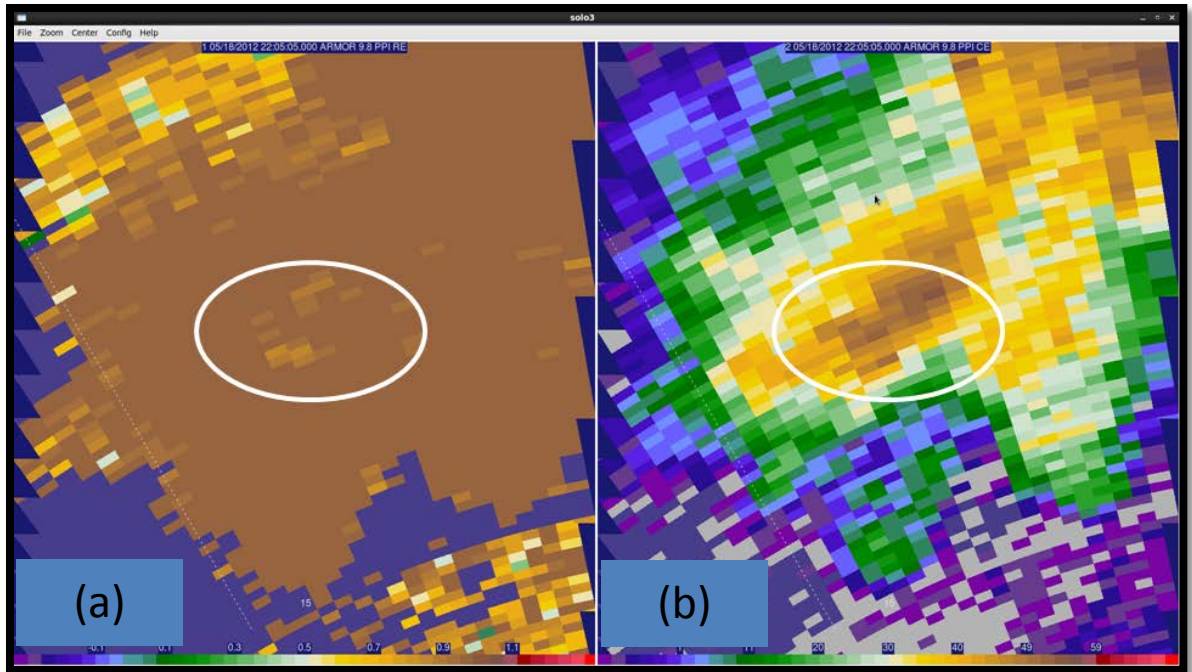


Figure 4.5. Corresponding ARMOR PPI of A1 from 2203 UTC on 18 May 2012. Left panel (a) is ρ_{hv} from 2203 UTC and right panel (b) is Z_h from 2203 UTC. The elevation angle is around 9.8° or just over 3 km. The circled region highlights regions in which ρ_{hv} drops to around 0.85. The level of 0°C is at 3.5 km.

As the hailstones fall, simulations have shown that most of the water accumulates along the major axis. This leads to an enhancement in Z_{dr} . Furthermore, this water shell can help to effectively stabilize hailstones and thus minimize tumbling. Anderson et al. (2011) noted that enhanced Z_{dr} values could also be in response to resonance effects at C-band, as the diameter of the melting hailstones (including the water shell) are no longer an order of magnitude smaller than the radar wavelength (e.g., diameter ≥ 5 mm). Large raindrops can generate enhanced Z_{dr} at C-band when they are in the resonant regime or larger than 5 mm in diameter (Bringi and Chandrasekar 2001).

The aforementioned values of Z_h , Z_{dr} , and ρ_{hv} observed during the 2203 UTC ARMOR volume around 3 km likely resulted in the NCAR PID diagnosing regions of large rain drops and rain hail mixtures. The vertical motion fields derived from multi-

Doppler wind synthesis revealed that the low-level (0-3 km) updraft was fairly weak only on the order of 2-3 m s⁻¹ (Figs. 4.3, 4.4). Terminal fall velocities derived for raindrops by Gunn and Kinzer (1949) in combination with estimates of vertical motion suggest that raindrops below one millimeter in diameter would be lofted upward while raindrops larger than one millimeter would likely fall downward. Figure 4.6a depicts a CAPPI at 5 km, while Fig. 4.6b depicts a vertical cross-section of A1 from ARMOR at 2203 UTC. Estimates of vertical motion just above the level of 0 °C revealed a broad 2-4 m s⁻¹ swath of upward velocities as seen in Fig. 4.6b from the 2203 UTC ARMOR X-Z cross-section.

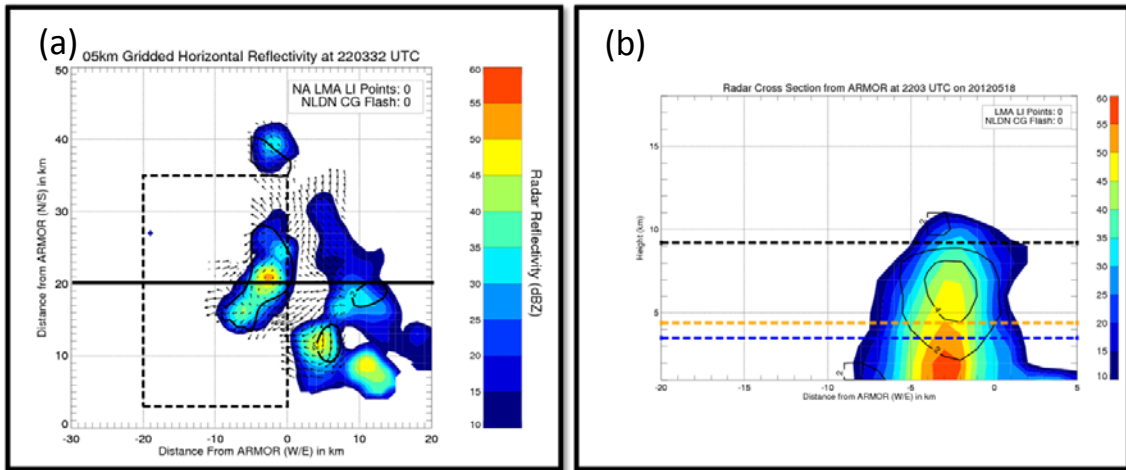


Figure 4.6. Left panel (a) represents a CAPPI at 5 km from ARMOR at 2203 UTC. The contour filled image represents the Z_h in dBZ and solid lines represent the vertical motion field in intervals of 2, 5, 10, 15, 20, and 25 m s⁻¹. Horizontal wind vectors are plotted. The solid black line at 20 km represents the location of the X-Z cross-section. The right panel (b) is a vertical cross-section in the X-Z plane taken at 20 km north of ARMOR. Contour filled image represents Z_h in dBZ and solid lines represent regions of upward vertical motion. Contour intervals for vertical motion are 2, 4, 6, 8, 10, 15, 20, 25 m s⁻¹.

Z_h and Z_{dr} values both showed a general decrease with height. Z_h values of 50-55 dBZ were common with occasional values around 60 dBZ. This peak was likely associated with the strongest vertical motion (closer to 4 m s⁻¹) (Fig. 4.7a). The areal extent of the higher Z_h values (60 dBZ) decreased substantially from the lower levels as

evidenced in the ARMOR cross-section (Fig. 4.7b) at 2203 UTC. Output from the NCAR PID (not shown) suggested that graupel, hail, and graupel/rain mixtures were all possible around 4 km at 2203 UTC. It should be mentioned that while the NCAR PID does explicitly discriminate between supercooled liquid drops and liquid drops, this functionality was not made available for the analysis of this case. As a result, supercooled water drops identified in this study were done using a subjective method using observed Z_h , Z_{dr} and temperature information from a sounding. Based on careful comparison of NCAR PID with these subjective analyses, it is concluded that the graupel/rain and hail/rain mix category above the level of 0 °C likely contains supercooled drops as well. The development of supercooled drops is critical to the growth of graupel particles via riming. This riming process occurs as supercooled cloud drop contacts an ice particle and freezes. Near the -10 °C level (4.5 km), it is hypothesized that the production of graupel via riming of supercooled raindrops increases. Since relatively large Z_h (45-50 dBZ) and Z_{dr} (~ 1 dB) values persisted within the 0 °C to -10 °C layer, it is likely that relatively large drops existed within this region. This region of higher Z_h in between the 0 °C and -40 °C layer likely corresponded to the updraft where conditions are likely warmer due to latent heat release associated with the updraft. It is interesting to note, that while necessary particles for NIC are present in the radar sample volume, no lightning yet occurred. One plausible explanation would be that the updraft was simply too weak to loft sufficiently large particles upward such that rebounding collisions between graupel and ice particles could occur. In fact, Zipser and Lutz (1994) note that maximum updraft speeds of at least 6-12 m s⁻¹ are required for significant electrification and lightning production.

Across the $-10\text{ }^{\circ}\text{C}$ to $-40\text{ }^{\circ}\text{C}$ region, Z_h values decreased slowly with maximum values on the order of 40-45 dBZ per Fig. 4.7b from the 2203 UTC ARMOR volume. Z_{dr} values showed a decrease from approximately 1.5 dB to 1 dB above the $-10\text{ }^{\circ}\text{C}$ level. This decline in Z_{dr} was indicative of a transition from wet oblate particles (suggested by the Z_{dr} in excess of 3 dB below the melt layer as seen in Fig 4.7b) such as supercooled rain drops to spherical ice particles such as graupel and small hail. The relatively smaller Z_{dr} values were around or below 1 dB. Moreover, lowered ρ_{hv} values near 0.85 suggested a mixture of hydrometeors across this layer (not shown). Estimates of vertical motion showed that the maximum in upward vertical motion was collocated with a relative maximum in Z_h .

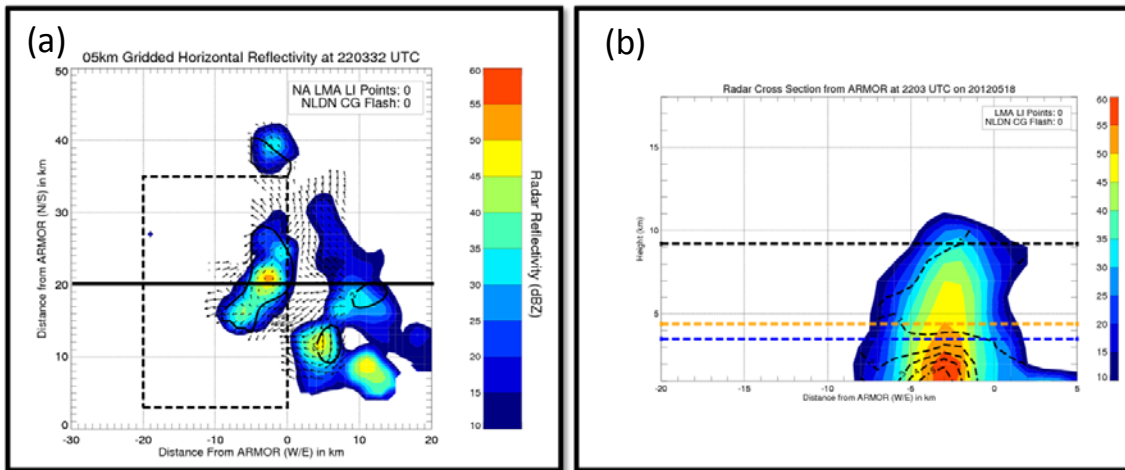


Figure 4.7. Left panel (a) represents a CAPPI at 5 km from ARMOR at 2203 UTC. Contour filled image represents Z_h in dBZ and solid vertical lines represent vertical motion in intervals of 2, 5, 10, 15, 20, and 25 m s^{-1} . The solid black line at 20 km represents the location of the X-Z cross-section. Horizontal wind vectors are plotted. The right panel (b) is a vertical cross-section in the X-Z plane taken at 20 km north of ARMOR. Contour filled image represents the horizontal radar reflectivity in dBZ and dashed line contour represents differential radar reflectivity greater than 0 dB at 1 dB increments.

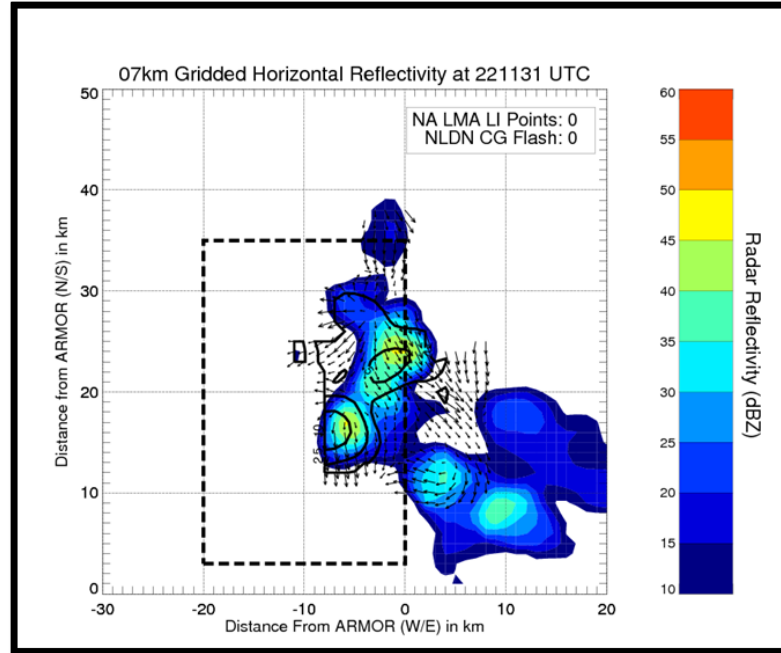


Figure 4.8. CAPPI at 7 km from ARMOR at 2211 UTC. Contour filled image represents Z_h in dBZ, solid vertical lines represent vertical motion in intervals of 2, 5, 10, 15, 20, and 25 m s^{-1} . Horizontal wind vectors are plotted.

During the 2211 UTC ARMOR volume scan additional updrafts developed. As seen in the CAPPI at 7 km (Fig. 4.8) it is apparent that the two regions of upward vertical motion likely corresponded to two separate updrafts. The mid-level updrafts (7 km) during this time period (2211 UTC) both extended upward into the $-20\text{ }^\circ\text{C}$ level (around 6.5 km) with peak upward velocities of around 3-10 m s^{-1} . At these colder temperatures, the NCAR PID indicated that graupel and hail dominated the radar sample volume (not shown). Despite this increase in upward vertical motion, the lack of relatively larger graupel particles, as will be shown in a time series, may have resulted in inefficient charging for lightning production.

4.1.3 Initial Lightning Activity of Complex A1 2215 UTC

With time, A1 grew quite rapidly between the 2203 UTC (Fig. 4.6) and 2215 UTC (Fig. 4.9) ARMOR volume. Typical of multicellular convection across DC3 AL, complex A1 initially consists of two distinct updrafts (Fig. 4.9a). Figure 4.9b shows a vertical slice through the northern updraft, approximately 28 km north of ARMOR. During the 2215 UTC ARMOR volume, NALMA detected 4 flashes with the NLDN detecting 1 negative CG. Three of these flashes were associated with the updraft roughly 15 km north of ARMOR while one lone flash was a result of the updraft located 25 km north of ARMOR. Estimates of vertical motion from multi-Doppler wind synthesis during the 2215 UTC ARMOR volume indicated that this northern updraft strengthened. This updraft located at 15 km north of ARMOR will be discussed later in this section. Maximum updraft velocities increased to 10-13 m s⁻¹, with the northern updraft, as seen in the X-Z ARMOR cross-section at 2215 UTC (Fig. 4.9b). Likely in response to the increased vertical motion, the extension of the 60 dBZ echo suggested that larger ice hydrometeors were being lofted into the colder region of the convective cloud (Fig. 4.9b).

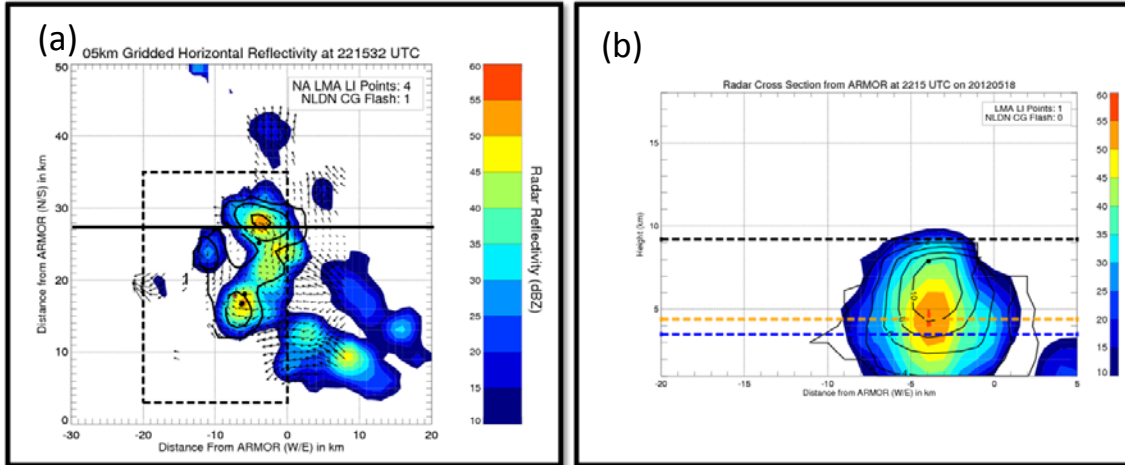


Figure 4.9. Left panel (a) represents a CAPPI at 5 km from ARMOR at 2215 UTC. The contour filled image represents the Z_h in dBZ and the solid lines represent the vertical motion field in intervals of 2, 5, 10, 15, 20, and 25 m s^{-1} . NALMA Lightning Initiation (LI) points are denoted in the solid black circle and NLDN CG Flashes are denoted in the solid brown circle. Horizontal wind vectors are plotted. The right panel (b) is a vertical cross-section in the X-Z plane taken at 28 km north of ARMOR. Contour filled image represents the horizontal radar reflectivity in dBZ and solid lines represent regions of upward vertical motion. Contour intervals for vertical motion are 2, 4, 6, 8, 10, 15, 20, 25 m s^{-1} .

Accretional growth of hydrometeors likely occurred during the 2215 UTC ARMOR volume. Moreover, the stronger updraft re-supplied this region of the cloud with additional condensate. This additional condensate (likely supercooled) may have aided in the continued growth of graupel and hail. From Fig. 4.10a and Fig. 4.10b, there appeared to be a decrease in Z_{dr} (< 1 dB) above the -10 °C level. This may have suggested the presence of spherical ice particles. Moreover, this increase in the magnitude of this updraft is apparent in the time series.

The time series in Fig. 4.11 reveals that the updraft volume greater than 5 m s^{-1} reached a local maximum during the 2215 UTC ARMOR volume with an updraft volume on the order of 10^{11} m^3 . While the calculation of the updraft volume is performed over two convective updrafts, it is likely that the northernmost updraft provided the higher contribution to this peak. It should be noted that the updraft velocities are likely an

underestimate due to inadequate sampling of the entire storm or relatively coarse 1 km resolution. This inadequate sampling results in an ambiguous upward boundary condition (e.g. divergence is non-zero) while the coarse resolution could under-estimate the peaks of some convective-scale features of the updraft. Regardless, the increasing trend in upward vertical velocities suggests that larger particles were growing and being lofted upwards. Increases in both the graupel echo volume and graupel mass (Fig. 4.12) accompanied this increase in the updraft volume (Fig. 4.11). During this phase, growth of graupel was likely enhanced as the updraft, visible in contours of vertical motion (Fig. 4.10a), lofts new condensates that readily take place in the freezing process. This was confirmed via the presence of a noticeable Z_{dr} column up through 3-4 km as seen in Fig. 4.10b. Maximum Z_{dr} values of around 2-3 dB were collocated with $Z_h > 60$ dBZ and ρ_{hv} values down to near 0.85. The large values of Z_h and Z_{dr} that extended well into the mixed phase region suggested the possibility of a mixture of large supercooled drops, large hail, and graupel particles. While the 1800 UTC UAH mobile RAOB (Fig. 4.2b) indicated that temperatures at this height (4 km) were around -4 °C, it is very likely that modification of the thermodynamic profile occurred in response to the warm bubble associated with the updraft.

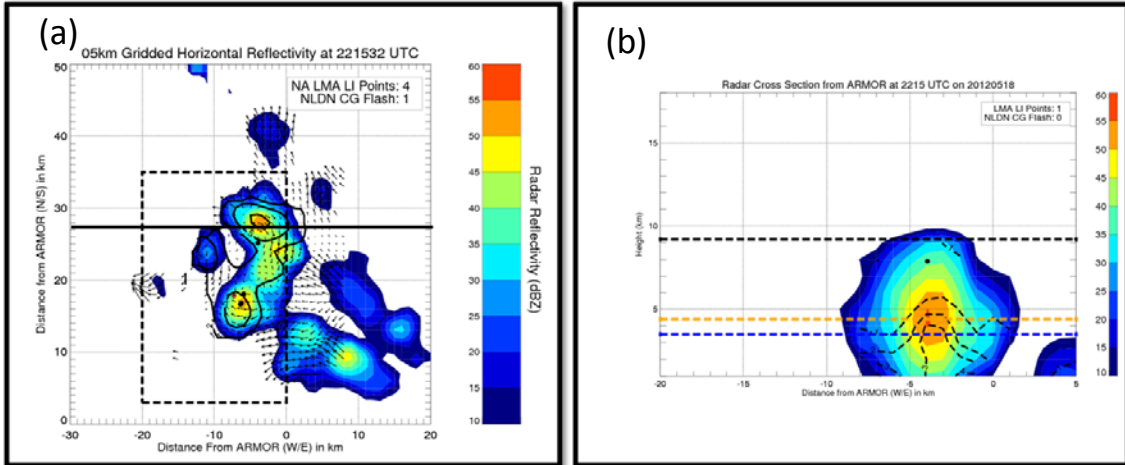


Figure 4.10. Left panel (a) represents a CAPPI at 5 km from ARMOR at 2215 UTC. The contour filled image represents Z_h in dBZ and the solid vertical lines represent vertical motion in intervals of 2, 5, 10, 15, 20, and 25 $m s^{-1}$. NALMA Lightning Initiation (LI) points are denoted in the solid black circle and NLDN CG Flashes are denoted in the solid brown circle. Horizontal wind vectors are plotted. The right panel (b) is a vertical cross-section in the X-Z plane taken at 28 km north of ARMOR. The contour filled image represents the horizontal radar reflectivity in dBZ and dashed line contour represents differential radar reflectivity greater than 0 dB at 1 dB increments.

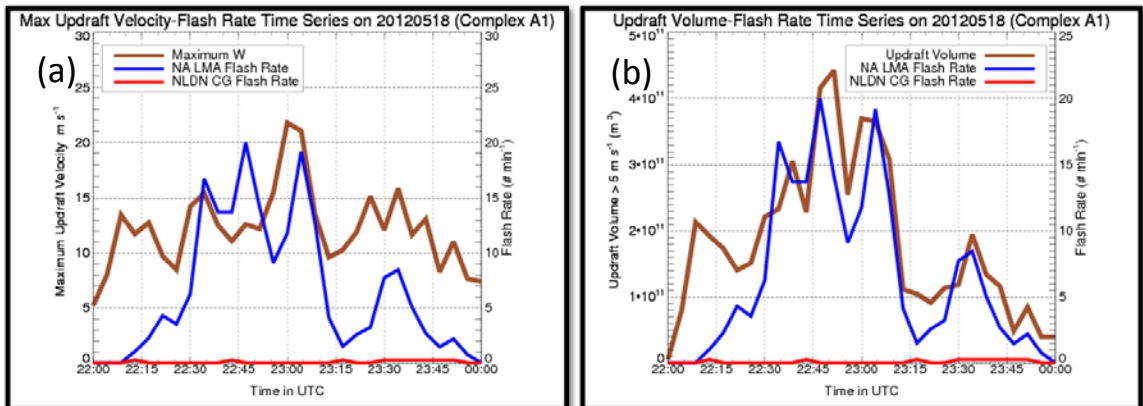


Figure 4.11. Co-evolution of kinematic and electrical properties for A1 on 18 May 2012. Left panel (a) represents the time series evolution of the maximum updraft velocity (solid brown line) as determined from multi-Doppler wind synthesis within the $-10^{\circ}C$ and $-40^{\circ}C$ temperature levels. The right panel (b) represents the time series evolution of the updraft volume greater than $5 m s^{-1}$ (solid brown line) within the $-10^{\circ}C$ and $-40^{\circ}C$ temperature levels and the total lightning flash. In (a) and (b) the total lightning flash rate (solid blue line) as inferred from NALMA and the CG flash rate (solid red line) as inferred from the NLDN are both depicted.

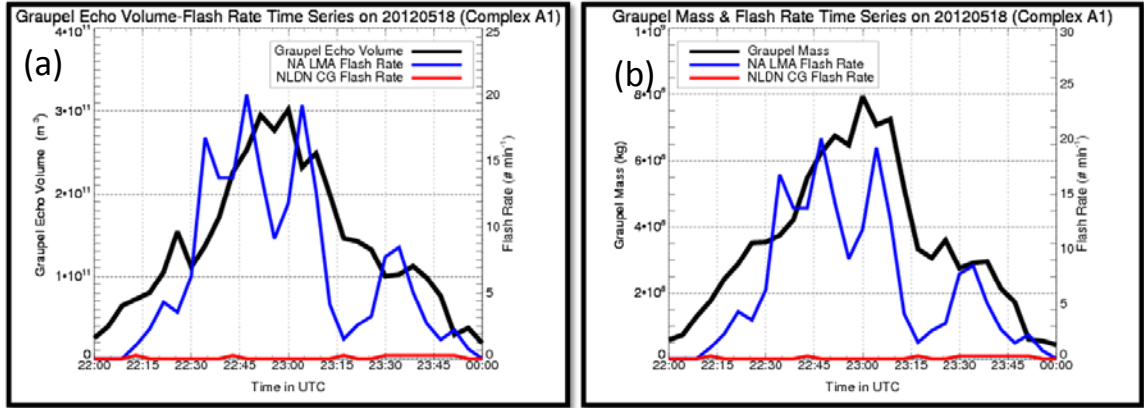


Figure 4.12. Co-evolution of kinematic and electrical properties for A1 on 18 May 2012. Left panel (a) represents the time series evolution of the graupel echo volume (solid black line) as determined from the NCAR PID within the -10 °C and -40 °C temperature levels. The right panel (b) represents the time series evolution of the graupel mass (solid black line) within the -10 °C and -40 °C temperature levels and the total lightning flash. In (a) and (b) the total lightning flash rate (solid blue line) as inferred from NALMA and the CG flash rate (solid red line) as inferred from the NLDN are both depicted.

The southernmost updraft associated with A1 was located approximately 15 km north of ARMOR (Fig. 4.13a) around 2215 UTC. This updraft aloft at 5 km exhibited maximum Z_h near 50-55 dBZ and maximum Z_{dr} values closer to 1 dB. The lower Z_h and Z_{dr} values at 5 km likely supported high density ice particles. While it is difficult to provide an actual size of hydrometeors lofted by the updraft it is apparent that the increase in Z_h (dependent on the size of hydrometeor) and the decrease in ρ_{hv} is evidence that a mixture of relatively larger volume of hydrometeors had been lofted upward. The increase in the number and size of graupel particles as indicated by the time series (Figs. 4.11 and 4.12) likely resulted in the increase in the gradient of the electric field, the rate of graupel electrification (based on empirical relationships derived by Takahashi (1978)) and hence the total lightning flash rate. The NCAR PID did indicate the presence of non-precipitation ice particles (e.g. ice crystals). A sufficient number of rebounding collisions between graupel and ice crystals further supported a likely increase in the magnitude of

the electric field (not measured). As a result of different terminal fall velocities between graupel and ice particles and the addition of the stronger updraft aloft, charge separation likely ensued. The ice crystals (smaller terminal fall velocity) were transported higher into the convective cloud via the updraft as opposed to the larger graupel (larger terminal fall velocity) particles. It is suspected that the breakdown field necessary for a discharge was approached and thus resulted in the first NALMA detected flash. The first flash detected by NALMA was around 2215 UTC at a height of 7 km just atop a gradient in Z_{dr} (not shown), which is similar to the results by Bruning et al. (2007). These initial flashes were associated with the updraft located approximately 15 km north of ARMOR (Fig. 4.13a). The flashes were detected by NALMA around a height of 7-8 km as well (Fig. 4.13b). In addition, NALMA detected an initial VHF radiation source around 3 km. Observations from the NLDN detected a –CG flash around the same location and time.

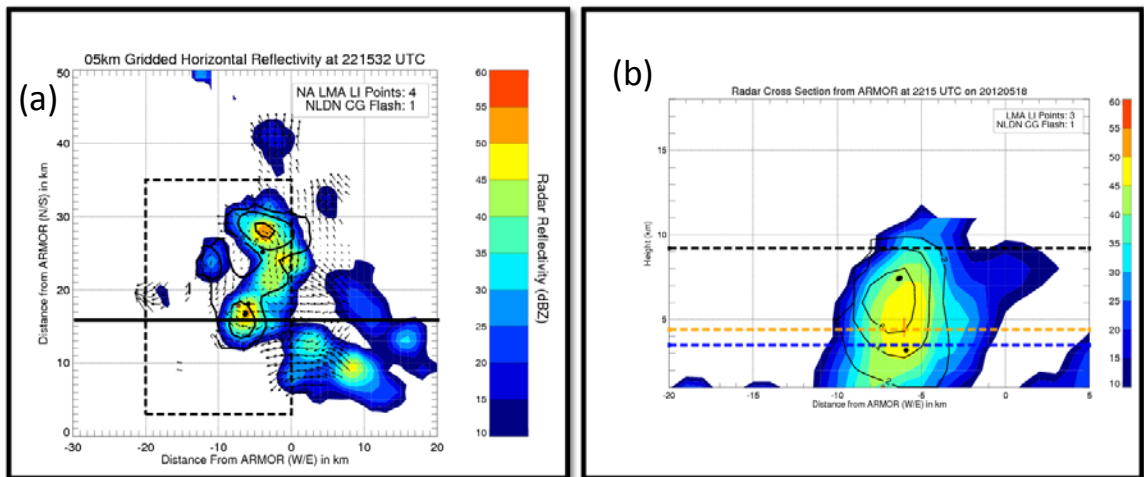


Figure 4.13. Left panel (a) represents a CAPPI at 5 km from ARMOR at 2215 UTC. Contour filled image represents the Z_h in dBZ and the solid lines represent the vertical motion fields in intervals of 2, 5, 10, 15, 20, and 25 $m s^{-1}$. Horizontal wind vectors are also plotted with the NALMA Lightning Initiation (LI) points are denoted in the solid black circle and NLDN CG Flashes are denoted in the solid brown circle. The right panel (b) is a vertical cross-section in the X-Z plane taken at 15 km north of ARMOR. Contour filled image represents Z_h in dBZ and solid lines represent regions of upward vertical motion. Contour intervals for vertical motion are 2, 4, 6, 8, 10, 15, 20, 25 $m s^{-1}$.

4.1.4 Increasing Lightning Part I 2231-2243 UTC

Further strengthening of complex A1 from a kinematic, microphysical, and electrical standpoint occurred through the ARMOR volume times of 2231 and 2235 UTC. Over these 3-4 minute volumes, the NALMA inferred total lightning flash rate increased from 6 flashes per min (during the 2231 UTC volume) to around 20 flashes per minute (during the 2235 UTC volume). During the 2231-2235 UTC ARMOR volume, the NLDN records no CG flashes. This absence of NLDN detected CG flashes during the initial and mature phases of A1 will be discussed in further detail during the dissipation phase section for A1. An increase in low-level convergence along the leading edge gust front as inferred from multi-Doppler analysis during the 2231 and 2235 UTC ARMOR volume likely contributed to the strengthening of one of the main updraft cores in the convective complex. This was accomplished by lifting of additional warm and moist air along the gust front. This higher equivalent potential air or theta-e air was then likely transported via air parcels upward and into the thunderstorm updraft. The additional buoyancy would explain the increase in peak updraft velocities. These strong updrafts were likely of sufficient magnitude to lift additional condensates through the warm cloud layer and ultimately into the mixed phase region.

This process is manifested in the increase in Z_h (3 km) when comparing the 2231 UTC and 2235 UTC ARMOR volumes (Fig. 4.14a and Fig. 4.14b, respectively). During the 2231 UTC ARMOR volume at 3 km, maximum Z_h and Z_{dr} values were around 50-55 dBZ and $\sim 2-4$ dB, respectively. During the 2235 UTC ARMOR volume, however, maximum 3 km Z_h values increased to around 60 dBZ and showed a much larger vertical extend throughout the entire depth of the storm. This process is best seen when

examining gridded radar cross-sections provided in Fig. 4.14a and Fig. 4.14b. Figures 4.14a and 4.14b show an increase in the overall precipitation echo volume as the 50 dBZ contour protruded above the -40 °C level. The time series (Fig. 4.11) reveals that the upward motion associated with this convective complex increased to above 10 m s⁻¹ within the -10 °C to -40 °C layer during the 2231 and 2235 UTC time periods. The X-Z cross-sections for both 2231 UTC and 2235 UTC are both taken approximately 30 km north of ARMOR in the X-Z plane. Of particular importance is the decrease in the height of the Z_{dr} (< 1 dB) column while Z_h increases (> 60 dBZ) in vertical extent (Fig 4.14). This processes likely signaled the onset of rapid freezing of drops.

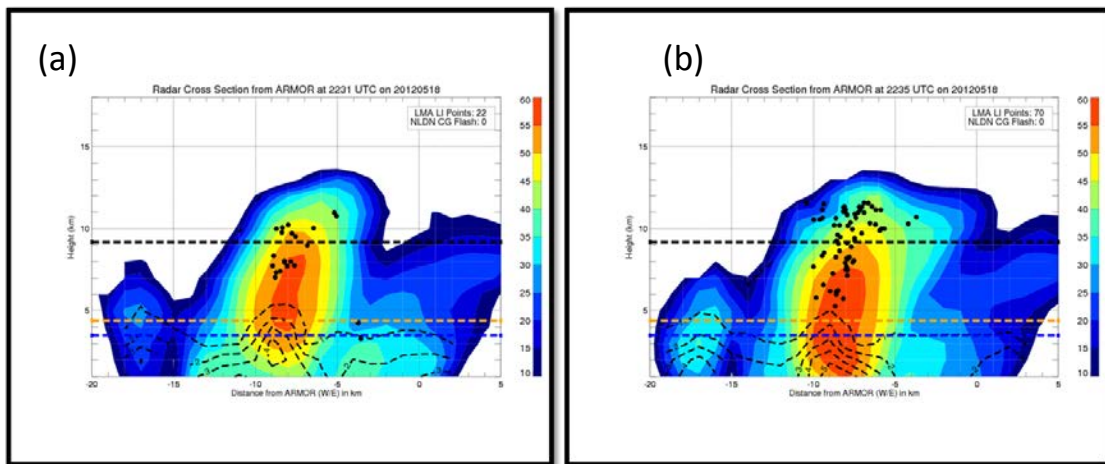


Figure 4.14. Gridded radar cross-section in the X-Z plane 30 km north of ARMOR at 2231 UTC (left [a]) and 2235 UTC (right [b]). Both images depict Z_h (dBZ) in the color fill. The dashed contours represent Z_{dr} > 0 dB in intervals of 1 dB. The solid black circles present NALMA VHF initiation sources while the solid brown circles represent NLDN CG flashes. Also in each plot, the dashed blue line corresponds to the 0 °C isotherm, the dashed orange line represents the -10 °C temperature level and the dashed black line represents the -40 °C level

The values of ρ_{hv} were relatively low, varying from 0.82 to 0.98 (not shown), in the mixed-phase region. These lowered values of ρ_{hv} indicate a variety of hydrometeors (e.g. graupel, hail, and supercooled water drops) were likely present across this mixed-phase region of the convective cloud (PID not shown but confirmed). During the 2231

and 2235 UTC ARMOR volumes, a hail flare or three-body scatter spike (TBSS) signature appeared (Fig. 4.15).

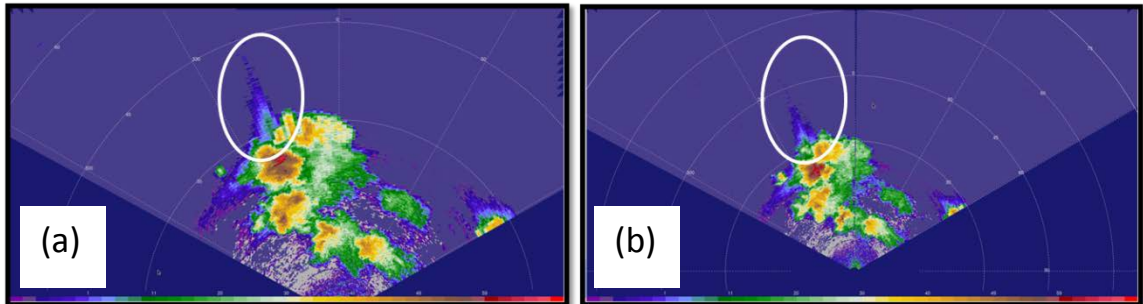


Figure 4.15. The left pane (a) depicts an ARMOR PPI during the 2231 UTC ARMOR scan volume. The right pane (b) depicts an ARMOR PPI during the 2235 UTC ARMOR scan volume. The approximate height of the radar beam is around 6 km in both panes. The solid white circle highlights the three body scatter spike (TBSS) signature.

This phenomenon, thought to be an indicator of large hail (Lemon 1998), appears primarily at upper levels of A1 (4.5 km to 9 km). Numerous studies have highlighted the relatively unimportance of large hail in terms of NIC (Williams et al. 2001; Deierling et al. 2008). Williams et al. (2001) speculated that the integrated surface area of large hail particles was smaller than that of graupel and small hail. As a result, the amount of charge generated via the NIC mechanism for large hail would likely prove to be insufficient. Deierling et al. (2008) also showed in a sensitivity test that hail has a relatively poorer correlation with total lightning flash rate when compared to graupel and total lightning flash rate. Again, the low concentration of large hail, when compared to graupel, resulted in a relatively smaller contribution to NIC. Similar to Deierling et al. (2008), sensitivity tests conducted on this data set when examining NCAR PID diagnosed graupel in isolation versus NCAR PID diagnosed graupel *and* hail mass exhibited very little difference from a correlation standpoint with total lightning. From the results of the sensitivity tests herein, it was revealed that the explicitly NCAR PID diagnosed large hail

versus total lightning flash rate revealed a poorer correlation as in Deierling et al. (2008). The appearance of the TBSS and resultant hail, however, could still prove to be important from a microphysical and kinematic standpoint. Graupel is often thought of as a predecessor to the growth of hail. This formation requires a strong updraft to keep millimeter sized precipitation particles lofted upward for additional riming of graupel particle. With the TBSS it is likely that large hail developed. This development of large hail was likely a direct result of a sufficiently larger number of graupel particles. In addition, the number of big graupel particles may have also increased. The increase in the number and perhaps size of graupel particles would result in an increase in the vertical gradient of the electric field (not measured) and rate of charge of graupel particles, and would likely result in a higher frequency of electric breakdown and ultimately larger total lightning flash rates.

This relatively higher production of lightning was noticeable during the 2235 UTC ARMOR volume. During this radar volume, NALMA suggested that flash rates were near 16 flashes per minute. Inspection of the trends (Figs. 4.11 and 4.12) in graupel mass, graupel echo volume and updraft volume all increased nearly simultaneously with this increase in the total lightning flash rate. The hail flare echo persisted through this volume scan time suggesting large hail aloft. The updraft volume $> 5 \text{ m s}^{-1}$ (W_5) began to show a larger vertical extent with the height of the 10 m s^{-1} above 11 km (not shown) (-40°C is at 9.2 km). Near 40 dBZ, Z_h and Z_{dr} less than 1 dB at 11 km would certainly suggest graupel and/or hail. From the estimates of vertical motion, velocities near or just above 5 m s^{-1} supported the lofting of graupel to such heights.

Perhaps of equal importance are the ρ_{hv} values near 0.99 (not shown) during the 2239 UTC ARMOR volume. This high value of ρ_{hv} often suggests widespread uniformity of a given hydrometeor in this radar sample volume; nearly all of the hydrometeors are graupel. Total lightning flash rate decreased slightly to near 13 flashes per minute during the 2239 UTC ARMOR volume. This is coincident with a slight decrease in the W_5 volume. Through the 2239 and 2243 UTC ARMOR volume, the total lightning flash rate remained steady with a flash rate of around 13 flashes per minute. During this time, however, additional low-level convergence along the leading edge gust front resulted in the generation of new low- and mid-level updrafts. Similar to the updrafts highlighted in the initial phases, these updrafts transported additional condensates upward into the mixed phase region. Through riming and freezing of supercooled water drops, the amount of graupel increased and this is evident in the time series of the graupel echo volume and lightning flash rate. NLDN detected a single +CG flash along the northern edge of complex A1.

4.1.5. Increasing Lightning Part II 2248 UTC

Through the 2243 UTC ARMOR volume, a sharp increase in the W_5 volume and graupel echo volume occurred (Figs., 4.11, 4.12). Graupel mass, however, only experienced a modest increase with the total lightning flash rate (Fig. 4.12). The first of two maxima in the total lightning flash rate occurred during the 2248 UTC ARMOR radar volume with a peak total lightning flash rate around 20 flashes per minute. An examination of a CAPPI at 3 km (Fig. 4.16a) from the 2248 UTC ARMOR volume suggested a strong low-level updraft developed along the convergence zone associated with the OFB (Fig. 4.16a). Peak updraft velocities were estimated to be around 5 m s^{-1} .

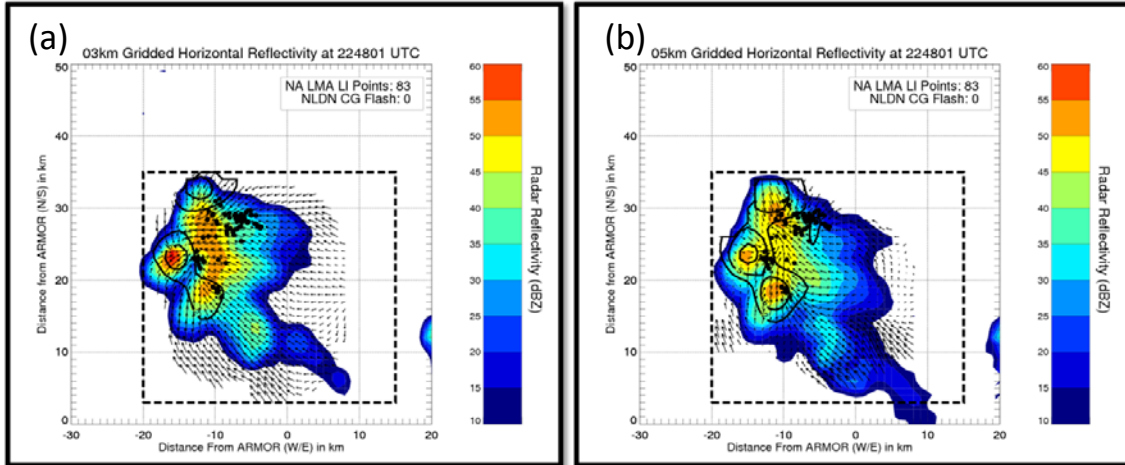


Figure 4.16. Left panel (a) represents a CAPPI at 3 km from ARMOR at 2248 UTC on 18 May 2012. Right panel (b) represents a CAPPI at 5 km from ARMOR at 2248 UTC on 18 May 2012. For both images, contour filled regions represent Z_h in dBZ and solid lines represent the vertical motion field in intervals of 2, 5, 10, 15, 20, and 25 m s^{-1} . In (a), horizontal wind vectors are plotted. NALMA Lightning Initiation (LI) points are denoted in the solid black circle and NLDN CG Flashes are denoted in the solid brown circle.

Inspection of CAPPI's aloft at 5km (Fig. 4.16b) during the 2248 UTC ARMOR volume, however, suggested three local maxima in vertical motion were likely associated with three distinct updrafts. Each updraft had peak velocities ranging from 8-10 m s^{-1} . Z_h values were typically in excess of 50-55 dBZ and Z_{dr} values were low and generally less than 1 dB. This combination of Z_h and Z_{dr} in conjunction with ρ_{hv} values around 0.90 (not shown) suggested that there was likely some variety in hydrometeors. Furthermore the NCAR PID confirmed the presence of a graupel and hail mixture. The time series of the W_5 volume (Fig. 4.11) indicated that the maximum updraft volume occurred during the 2348 UTC ARMOR volume. Continuity of the three local maxima in updraft persisted up through 11 km (not shown). As such, graupel and hail particles were likely suspended for longer times. This likely resulted in continued growth of precipitation ice. This continued, albeit modest, growth of graupel was evident in the time series of total storm graupel mass and flash rate (Fig 4.12). A gradual decrease in the total lightning

flash rate occurred from 2252 UTC through 2256 UTC. The time series evolution of the W_5 volume showed a quick decrease during this time (Fig 4.11). While not nearly as drastic of a decrease, the graupel echo volume and graupel mass each exhibited a slight decline. It is evident that there is some sensitivity regarding the microphysical and kinematic properties of DMC and total lightning. As the magnitude of the updraft decreased, it is likely that the supply of fresh condensates for supercooled cloud water decreased. As a result, the ability for NIC was likely hindered and this is manifest by the decrease in the total lightning flash rate.

4.1.6 Increasing Lightning Part III 2304 UTC

The second maximum in the total lightning flash rate occurred during the 2304 UTC ARMOR volume. A resurgence of the W_5 volume, graupel mass and graupel echo volume occurred during this time period as highlighted in their respective time series evolution with the total lightning flash rate (Figs. 4.11, 4.12). The total lightning flash rate during this time period was nearly 20 flashes per minute. A few low-level updrafts matured as additional convergence along the OFB continued. Mid-level updrafts (5-6 km) during this time period were stronger than in previous stages with updraft velocities on the order of $12-15 \text{ m s}^{-1}$. From a charge structure standpoint, it may be plausible to suggest that the lack of CG lightning during this intense portion of the cells lifetime was a result of an elevated dipole (MacGroman et al. 1989). Based on the placement of the NALMA initiation sources during the 2304 UTC ARMOR volume, it would appear that this elevated dipole was located around 8-10 km aloft (Fig. 4.17a). The 2304 UTC ARMOR cross-section and CAPPI at 6 km (Fig. 4.17b) revealed that Z_h remained high with values around 60 dBZ.

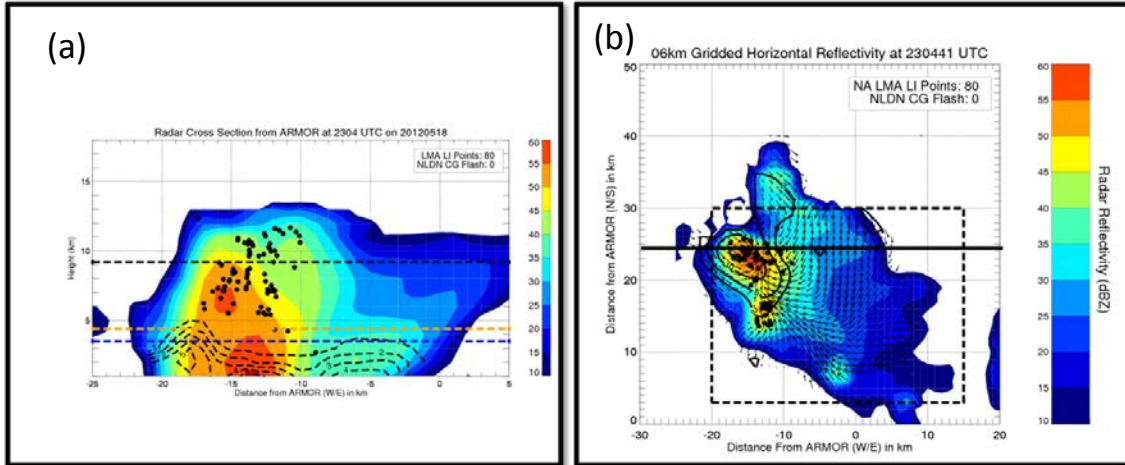


Figure 4.17. The left panel (a) is a vertical cross-section in the X-Z plane taken around 25 km north of ARMOR at 2304 UTC. The contour filled image represents the Z_h in dBZ and dashed line contour represents differential radar reflectivity greater than 0 dB at 1 dB increments. Also, the dashed blue line corresponds to the 0 °C isotherm, the dashed orange line represents the -10 °C temperature level and the dashed black line represents the -40 °C level. Right panel (b) represents a CAPPI at 6 km from ARMOR at 2304 UTC. The contour filled image represents Z_h in dBZ and the solid black lines represent the vertical motion field in intervals of 2, 5, 10, 15, 20, and 25 m s^{-1} . NALMA Lightning Initiation (LI) points are denoted in the solid black circle and NLDN CG Flashes are denoted in the solid brown circle.

With maximum Z_h values near 60 dBZ, Z_{dr} values near 0 dB and ρ_{hv} values close to unity, large spherical objects such as hail and graupel were likely. Maximum updraft velocities from the multi-Doppler wind synthesis exceeded 20 m s^{-1} (Fig. 4.17b). The strongest regions of upward vertical motion (W of at least 5 and 10 m s^{-1}) extended upwards from 2 km (Fig. 4.18a) up through 12 km (Fig. 4.18b). This type of vertical motion likely supported the lofting of graupel and large hail upward into much colder regions of the convective cloud. A quasi-persistent updraft is observed during this time period would have kept the larger particles relevant to NIC (graupel and ice crystals) lofted higher in the storm and supported an elevated dipole. As such, the strongest gradient in the electric field may have occurred somewhere near the mid-level updraft (6 km). Low-level radial convergence and strong radial storm summit divergence as seen in Fig. 4.18b may have suggested that a very well ventilated convective updraft occurred during the 2304 UTC

ARMOR volume. These type of airflow patterns may have some utility for atmospheric modelers as it could be used to help verify numerical simulations of DMC.

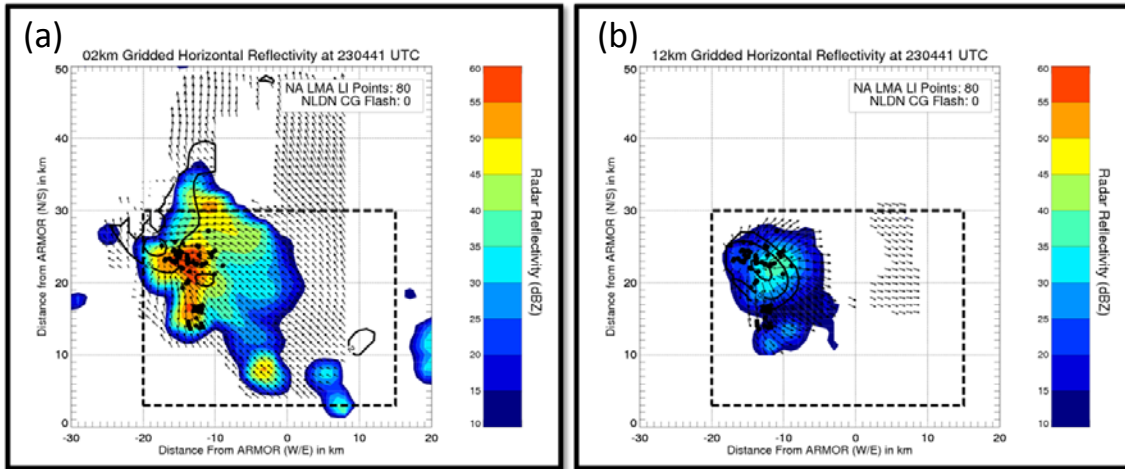


Figure 4.18. Left panel (a) represents a CAPPI at 2 km from ARMOR at 2248 UTC on 18 May 2012. Right panel (b) represents a CAPPI at 12 km from ARMOR at 2304 UTC on 18 May 2012. For both images, contour filled regions represent Z_h in dBZ and the solid black lines represent the vertical motion field in intervals of 2, 5, 10, 15, 20, and 25 m s^{-1} . NALMA Lightning Initiation (LI) points are denoted in the solid black circle and NLDN CG Flashes are denoted in the solid brown circle. Horizontal wind vectors are plotted.

4.1.7 Dissipation Phase of Complex A1

The initial decline in kinematic, microphysical and electric quantities began shortly after the 2308 UTC ARMOR radar volume scan (Figs. 4.11, 4.12). A slight recovery in all quantities occurred just after 2330 UTC as one last updraft developed along the OFB (not shown). The monotonic decrease in all quantities ensued shortly thereafter with no lightning detected by either NALMA or NLDN just before 0000 UTC. Due to the weakly sheared environment, the leading edge gust front propagated out ahead of the main convective line (not shown). As shown in simulations and observations, the inability to lift additional parcels to the LFC often resulted in the demise of the multicellular complex. Moreover, the generation of negative buoyancy via melting or

evaporation likely resulted in the generation of a strong downdraft. The onset of either of these processes likely resulted in the decay of A1. Maximum updraft speeds decreased from near 21 m s^{-1} down to 13 m s^{-1} (Fig. 4.11) between the 2308 and 2330 UTC. Additional evidence of this decrease in vertical motion can be found aloft, where the extent of the 5 m s^{-1} decreased (Figs. 4.19a and 4.19b). As the updraft weakened, the amount of graupel mass and graupel echo volume decreased (Fig. 4.12). The IC lightning activity decreased quickly from $12 \text{ flashes min}^{-1}$ to $4 \text{ flashes min}^{-1}$. The decrease in the lightning flash rate was likely tied to the decrease in processes critical to NIC. The smaller number and size of graupel particles as suggested by the dual-polarization radar analysis would support a weaker vertical electric field gradient and smaller charging rates. This would have ultimately led to a reduction in the amount of total lightning being generated.

A slight increase in the total lightning flash rate occurred shortly during the 2329 UTC ARMOR volume as one last convective cell developed along the gust front. Lightning flash rates peak around 8 flashes per minute during the 2333 UTC ARMOR volume. Vertical motion recovered slightly during this time period as peak velocities approached 15 m s^{-1} . As the OFB moved westward (not shown), this short-lived updraft decayed. Interestingly, it was during this time period between 2329 and 2349 UTC that the most CG lightning occurred. Over the prior 80 minutes, only 3 CG flashes were recorded by the NLDN. During this 20-minute time span from 2329 through 2349 UTC, 6 CG additional flashes were observed by the NLDN. Similar to CR00 and Kuhlman (2006), it is likely that this increase towards the end of the convective complex was associated with the descent of graupel below the melting layer (Fig 4.12). Also of interest

are the long extensive flashes that occurred in the large anvil that extended nearly 40 km to the east of the most vigorous vertical motion (Fig 4.19). Residual charge likely existed in this thick cirrus canopy, as suggested by the areal extent of the 10 dBZ echo in Figs. 4.19a and 4.19b. Most of these large extensive flashes (of around 20-30 km) typically originated near the updraft region, as inferred from the NALMA. Upon initiation, these flashes spread rapidly out into the anvil with nearly hundreds of sources as illustrated in Fig. 4.20.

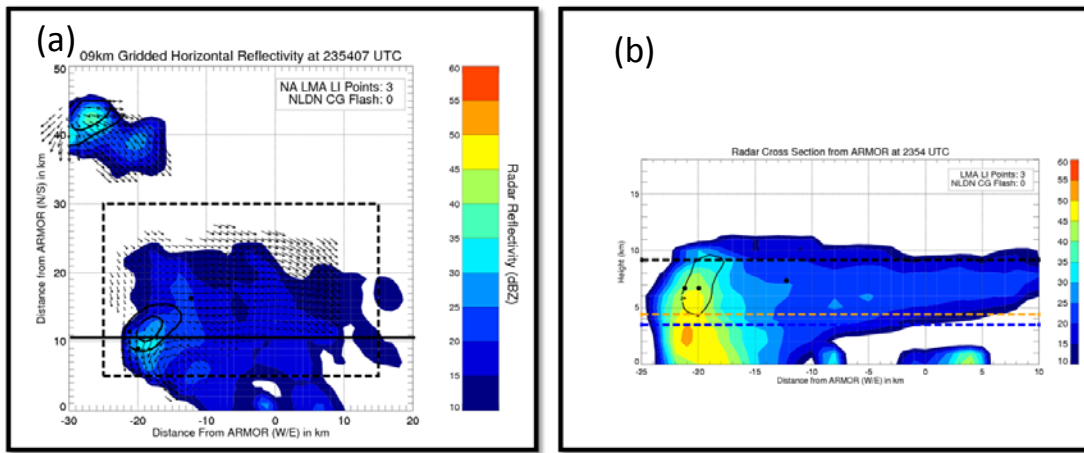


Figure 4.19. Left panel (a) represents a CAPPI at 9 km from ARMOR at 2354 UTC. Contour filled image represents Z_h in dBZ and the solid black lines represent the vertical motion field in intervals of 2, 5, 10, 15, 20, and 25 $m s^{-1}$. NALMA Lightning Initiation (LI) points are denoted in the solid black circle and NLDN CG Flashes are denoted in the solid brown circle. Horizontal wind vectors are plotted. The right panel (b) is a vertical cross-section in the X-Z plane taken at 10 km north of ARMOR during the same time. The contour filled image Z_h in dBZ and solid lines represent regions of upward vertical motion. The contour intervals for vertical motion are 2, 4, 6, 8, 10, 15, 20, 25 $m s^{-1}$. Also, the dashed blue line corresponds to the 0 °C isotherm, the dashed orange line represents the -10 °C temperature level and the dashed black line represents the -40 °C level.

One expansive flash propagated nearly 20 km. As shown by Barthe and Barth (2010), these expansive flashes are thought to be important to the production of NO_x . The rapid decrease in all kinematic, microphysical, and kinematic quantities continued through 0000 UTC (19 May 2012) where all lightning activity ceased (Figs. 4.11, 4.12).

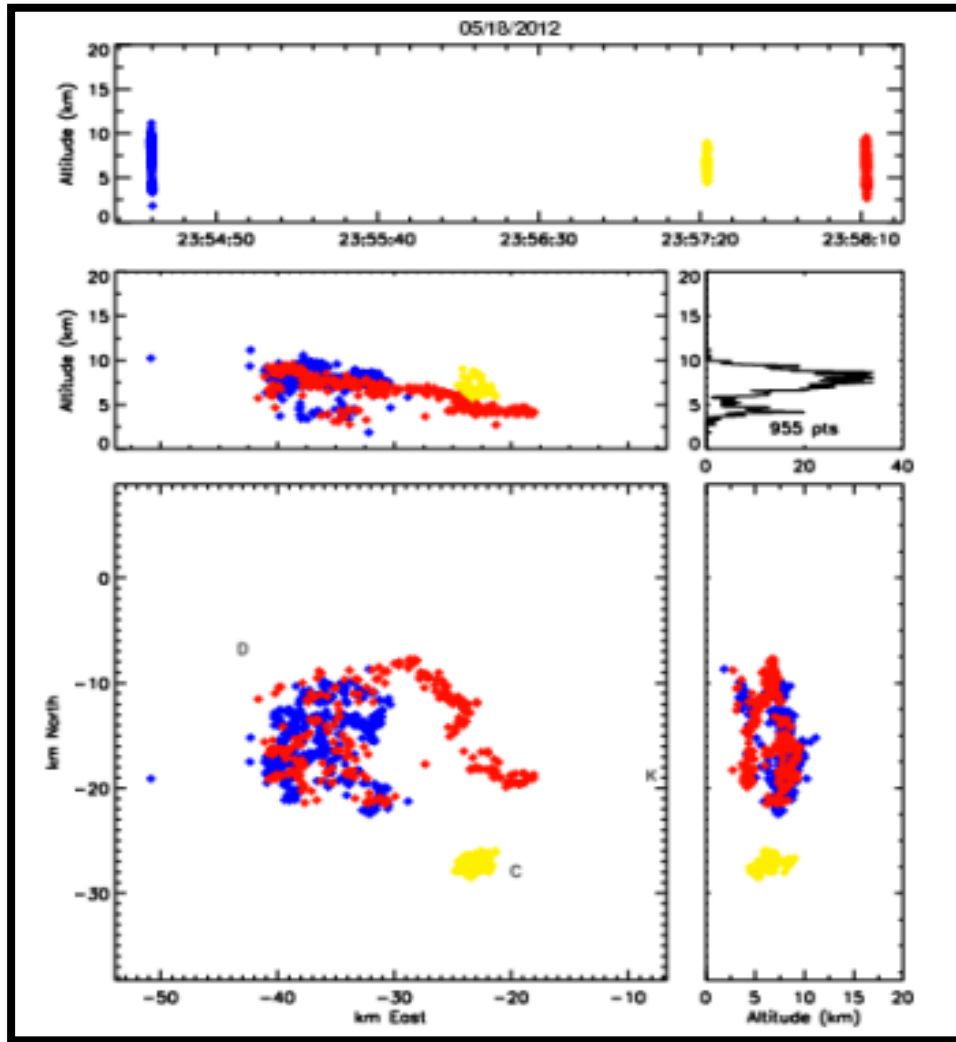


Figure 4.20. Graphical representation of three flashes detected by NALMA between 2252 UTC and 2258 UTC. The top panel is a time series plot showing the approximate time and vertical extent of the VHF sources. The middle left panel is an X-Z cross-section with the right left panel representing a VHF source frequency histogram with height. The bottom left panel shows the X-Y plan view of VHF sources and the bottom right panel shows the Y-Z view of the VHF sources. Distances are relative to the NSSTC.

4.2 21 May 2012 Case Day

4.2.1 Meteorological Overview

The 21 May 2012 case day featured two rounds of DMC across DC3 AL. Early in the morning, areas of convection developed upstream of the TN valley across portions of the mid-Mississippi river valley. At the 300 hPa (1200 UTC analysis) level a neutral

trough extended down from the western Great Lakes region southward towards the mid MS river valley (Fig 4.21a). Figure 4.21b depicts the 0600 UTC surface analyses that revealed that a cold front stretched from portions of MO, southward into TX. The feature of most importance, however, was the prefrontal trough east of the front that stretched from western OH through western KY and TN.

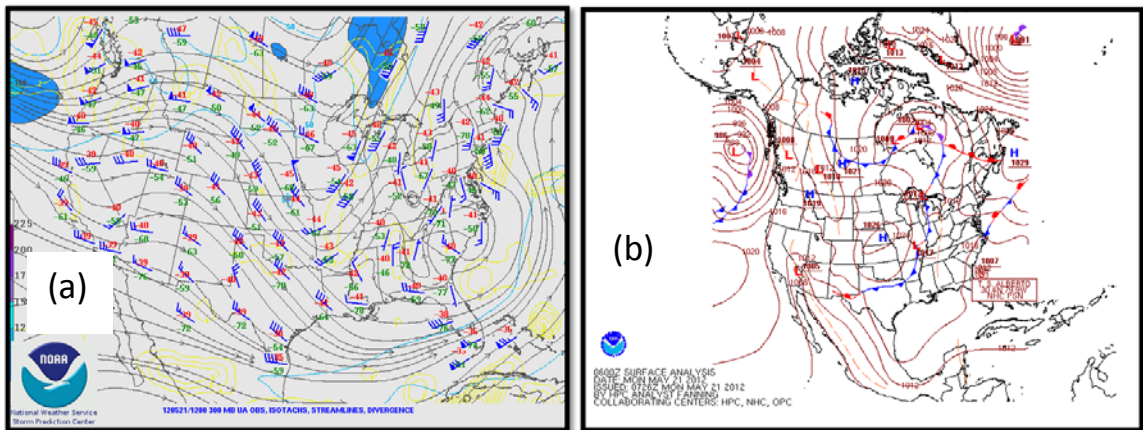


Figure 4.21. The left panel (a) depicts the 1200 UTC objective analysis from SPC on 21 May 2012 at 300 hPa. The right panel (b) is the subjective surface analysis from the Hydrometeorological Prediction Center (HPC) at 06 UTC on 21 May 2012.

It is likely that low-level convergence in conjunction with the weak large scale ascent beneath the entrance region of the trough was sufficient for the generation of nocturnal DMC. This DMC trekked towards the DC3 AL domain during the early morning time period on 21 May 2012. This complex produced numerous outflow boundaries downstream that served to initiate new convection. Around 11 UTC, a small complex moved through the center portion of the DC3 AL network, effectively stabilizing the region as seen in the 1200 UTC KQAG RAOB (Fig. 4.22a). This convection gradually weakened as it moved across eastern portions of the DC3 AL network. Analysis of satellite imagery shortly before 1930 UTC revealed a very transient mesoscale convective

vortex (MCV) across southeastern portions of TN (not shown). Weak westerly upslope flow combined with weak ascent from the MCV and differential heating along the Cumberland Plateau likely resulted in convective initiation.

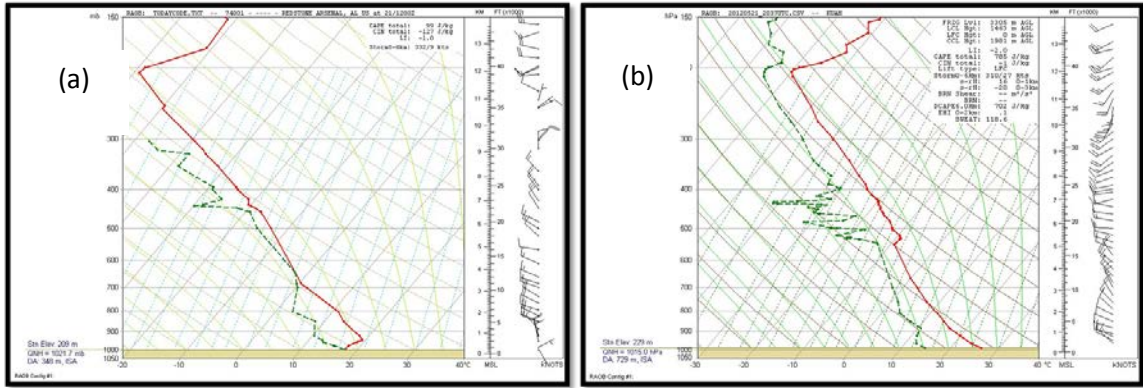


Figure 4.22. Comparison of 1200 UTC RAOB from Redstone Arsenal, AL (a) on 21 May 2012 and 2037 UTC UAH mobile RAOB (b) taken from Capshaw, AL.

The 2037 UTC UAH mobile RAOB (Fig. 4.22b) from near Capshaw, AL revealed that the airmass across the TN valley had continued to destabilize as SBCAPE values increased to around 785 J kg^{-1} and SBCIN values approached -1 J kg^{-1} . Deep layer wind shear was weak with values in the $1\text{-}2 \text{ m s}^{-1}$ range. The 2037 UAH mobile RAOB (Fig. 4.22b) revealed modest low-level (surface-3 km) lapse rates on the order of $-7.5 \text{ }^\circ\text{C km}^{-1}$. A summary of environmental parameters obtained from the 2037 UTC UAH mobile RAOB near Capshaw, AL, can be found in Table 4.2. Under the influence of west to northwest flow, convection generally travelled to the east and southeast. Low-level convective outflow, however, progressed towards the west and southwest (not shown). This resulted in the generation of new convective cells along the western flanks of multicellular complexes. Initially two distinct updrafts developed as seen in two relative

maxima in Z_h (Fig 4.23). Their individual morphology will be examined before both elements merge around the 2015 UTC ARMOR radar volume.

Table 4.2. A summary of convective parameters for the 21 May 2012 case day from the 2037 UTC UAH mobile RAOB. The RAOB was taken near Capshaw, AL, approximately 18 km NW of KHSV.

Convective Parameter	Value
850-700 hPa lapse rate	-3 °C km ⁻¹
850-500 hPa lapse rate	-6.2 °C km ⁻¹
SFC-3 km lapse rate	-7.3 °C km ⁻¹
SBCAPE	785 J kg ⁻¹
SBCIN	-1 J kg ⁻¹
DCAPE	702 J kg ⁻¹
Lifted Index	-2 °C
0-6 km shear	1.2 m s ⁻¹
0 °C level	3.5 km
-10 °C level	5.5 km
-40 °C level	9.5 km

4.2.2 Development of two separate updrafts (1945 UTC-2001 UTC)

As previously mentioned, convective elements of what would eventually become B2 developed nearly 80 km north of the ARMOR radar site located at KHSV around 1945 UTC. Explosive development of a mature updraft was hindered as a result of the poor 850-700 hPa lapse rate (Table 4.2). Initially, echoes were confined to below the -10 °C (5.5 km) level with very weak vertical motion. During the 2001 UTC ARMOR radar volume, however, two distinct maxima in the vertical motion field were observed (Fig. 4.23a). At the 2001 UTC ARMOR volume, both the northern (approximately 76 km north of ARMOR) and southern (approximately 65 km north of ARMOR) updraft regions exhibited peak velocities of around 6 and 2 m s⁻¹, respectively, per multi-Doppler wind synthesis (Fig 4.23a). A vertical cross-section through the northernmost updraft at 2001 UTC (around 76 km north and 5 km east of ARMOR) indicated that vertical motion as

high as 4 m s^{-1} extended up to 7-8 km (Fig. 4.23b). This vertical motion associated with the northern updraft was of a sufficient magnitude such that it was able to loft hydrometeors upwards. These hydrometeors exhibited Z_{dr} values on the order of 2-3 dB and were therefore likely raindrops (Fig. 4.24). From Figs. 4.23 and 4.24, it is apparent that supercooled raindrops were lofted upward into the $0 \text{ }^{\circ}\text{C}$ (3.5 km) to $-10 \text{ }^{\circ}\text{C}$ (5.5 km) layer.

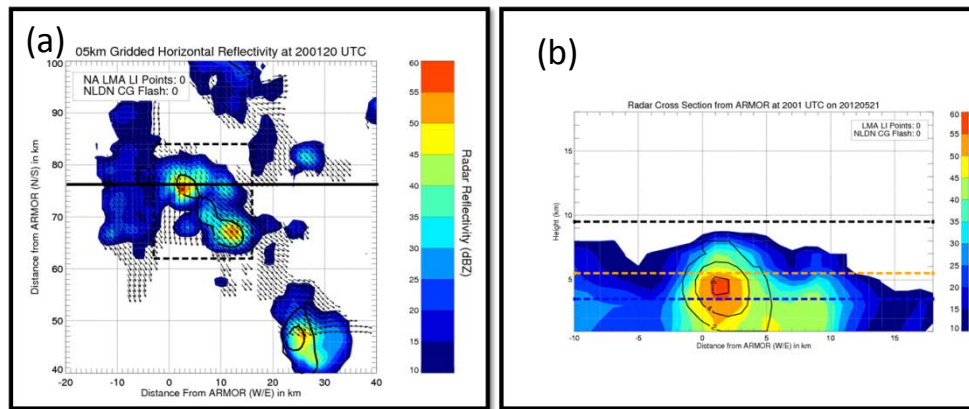


Figure 4.23. Left panel (a) represents a CAPPI at 5 km from ARMOR at 2001 UTC on 21 May 2012. Contour filled image represents the Z_h in dBZ and the solid black lines represent the vertical motion field in intervals of 2, 5, 10, 15, 20, and 25 m s^{-1} . The solid black line denotes the X-Z cross-section location (around 76 km north of ARMOR). Horizontal wind vectors are plotted. The right panel (b) is a vertical cross-section in the X-Z plane taken at 76 km north of ARMOR during the same time. Contour filled image represents the horizontal radar reflectivity in dBZ and solid lines represent regions of upward vertical motion. Contour intervals for vertical motion are 2, 4, 6, 8, 10, 15, 20, 25 m s^{-1} . Also, the dashed blue line corresponds to the $0 \text{ }^{\circ}\text{C}$ isotherm, the dashed orange line represents the $-10 \text{ }^{\circ}\text{C}$ temperature level and the dashed black line represents the $-40 \text{ }^{\circ}\text{C}$ level.

Moderate to high Z_h around 55-60 dBZ in this same layer confirmed the presence of large hydrometeors associated with the northernmost updraft. Slightly lowered values of ρ_{hv} (around 0.93) (not shown) also suggested some mixture of hydrometeors toward the top of the Z_{dr} column. The combination of environmental and polarimetric radar data indicated a mixture of supercooled liquid drops, hail and graupel in this region. Above the $-10 \text{ }^{\circ}\text{C}$ level, a gradient in both Z_h and Z_{dr} exists. Given the values of Z_h and Z_{dr}

decreasing to 40-45 dBZ and 1-2 dB (Fig. 4.24), respectively, as well as ρ_{hv} values remaining around 0.93 (not shown), the number of frozen particles was increasing with height above the $-10\text{ }^{\circ}\text{C}$ level.

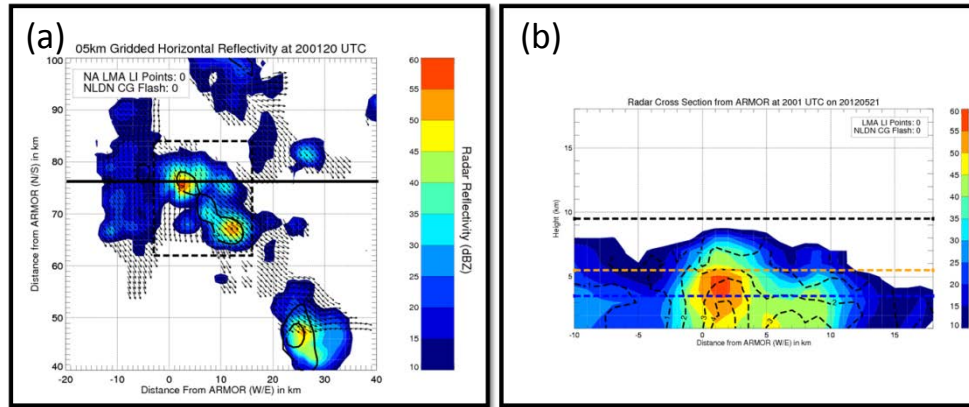


Figure 4.24. Left panel (a) represents a CAPPI at 5 km from ARMOR at 2001 UTC on 21 May 2012. Contour filled image represents the Z_h in dBZ and the solid black lines represent the vertical motion field in intervals of 2, 5, 10, 15, 20, and 25 m s^{-1} . The solid black line denotes the X-Z cross-section location (around 76 km north of ARMOR). Horizontal winds are plotted. The right panel (b) is a vertical cross-section in the X-Z plane taken at 76 km north of ARMOR during the same time. Contour filled image represents Z_h in dBZ and dashed lines represent Z_{dr} greater than 0 dB with increments of 1 dB. Also, the dashed blue line corresponds to the $0\text{ }^{\circ}\text{C}$ isotherm, the dashed orange line represents the $-10\text{ }^{\circ}\text{C}$ temperature level and the dashed black line represents the $-40\text{ }^{\circ}\text{C}$ level.

Specifically, this gradient in Z_{dr} suggested a transition to slightly more precipitation ice (likely graupel and/or small hail). NCAR PID output confirmed the presence of graupel aloft in the $-10\text{ }^{\circ}\text{C}$ to $-40\text{ }^{\circ}\text{C}$ layer (not shown). The increase in the graupel echo volume (Fig. 4.25a) and graupel mass (Fig. 4.25b) with time was coincident with the increase in maximum updraft (Fig. 4.26a) and updraft volume (Fig. 4.26b), thus underscoring the physical and statistical relationship between the microphysics and kinematics.

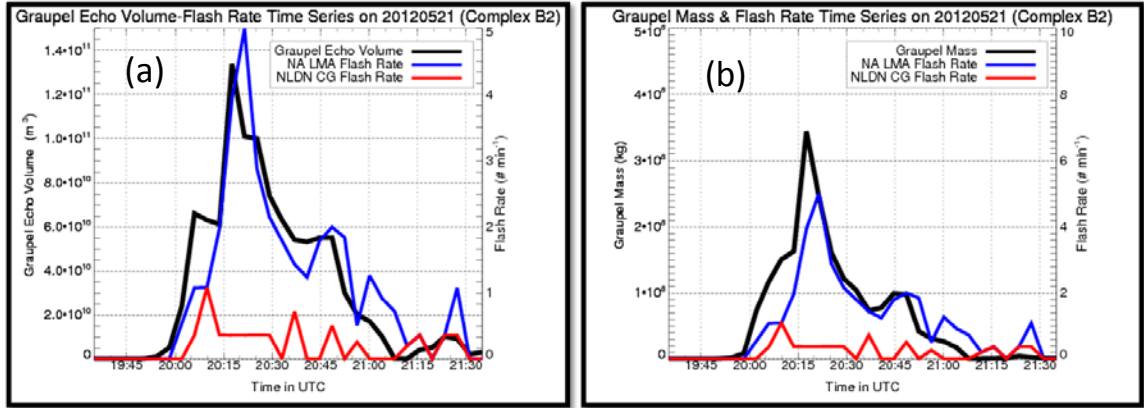


Figure 4.25. Time series evolution of DMC microphysics and electrical properties for complex B2 on 21 May 2012. The left panel (a) represents the time series evolution of graupel echo volume (solid black line) within the -10°C and -40°C temperature layer. The right panel (b) represents the graupel mass (solid black line) within the -10°C and -40°C temperature level. In both (a) and (b) the total lightning flash rate as inferred from NALMA (solid blue line) and the CG lightning flash rate (solid red line) are both depicted.

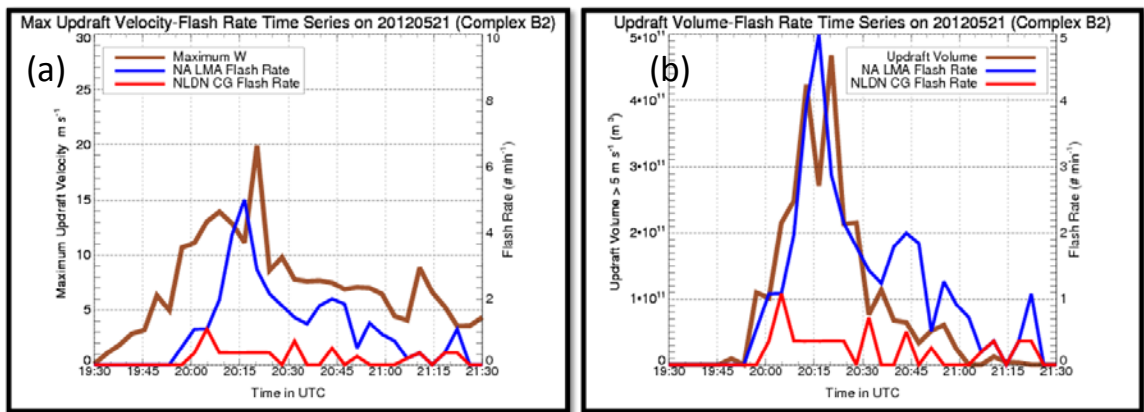


Figure 4.26. Time series evolution of DMC kinematic and electrical properties for complex B2 on 21 May 2012. The left panel (a) represents the time series evolution of the maximum updraft velocity (solid brown line) within the -10°C and -40°C temperature layer. The right panel (b) represents updraft volume $> 5\text{ m s}^{-1}$ (solid brown line) within the -10°C and -40°C temperature level. In both (a) and (b) the total lightning flash rate as inferred from NALMA (solid blue line) and the CG lightning flash rate (solid red line) are both depicted.

4.2.3 Lightning Production in the Northernmost Updraft (2004-2012 UTC)

During the 2004 UTC ARMOR radar volume, the northernmost updraft located around 76 km north of ARMOR produced its first flashes (Fig. 4.27). Two of the three initiation VHF sources originated just below 8.5 km along a region characterized by low Z_h (20-30 dBZ) and low Z_{dr} (~ 1 dB). NCAR PID suggested that this region contained a

mixture of graupel and ice crystals (not shown). The diagnosed hydrometeors in this radar sample volume supported the theory that these flashes were likely a result of NIC. The first VHF radiation source associated with the third flash was detected at an altitude of around 5.2 km. This source was located in an area of higher Z_h (45 dBZ) and low Z_{dr} (< 1 dB) indicative of graupel and/or small hail, which likely resulted from the freezing of supercooled raindrops shown at this altitude earlier at 2001 UTC (Fig. 4.23). The increase in graupel and vertical motion is apparent in Figs. 4.25 and 4.26. Through 2012 UTC, NALMA detected 6 additional flashes and NLDN detected 4 CG flashes, all of which were associated with the northern updraft. At 2012 UTC, further strengthening of the southern updraft occurred as peak velocity values exceeded 10 m s^{-1} .

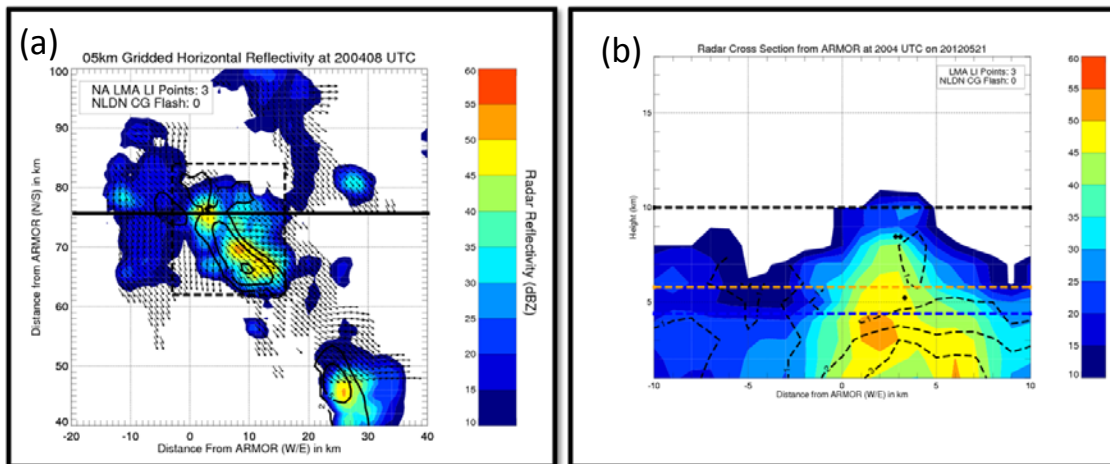


Figure 4.27. Left panel (a) represents a CAPPI at 5 km from ARMOR at 2004 UTC on 21 May 2012. The contour filled image represents the Z_h in dBZ and the solid black lines represent the vertical motion field in intervals of 2, 5, 10, 15, 20, and 25 m s^{-1} . NALMA Lightning Initiation (LI) points are denoted in the solid black circle and NLDN CG Flashes are denoted in the solid brown circle. The solid black line denotes the X-Z cross-section location (around 77 km north of ARMOR). Horizontal wind vectors are plotted. The right panel (b) is a vertical cross-section in the X-Z plane taken at 77 km north of ARMOR during the same time. Contour filled image represents Z_h in dBZ and dashed lines are contours of $Z_{dr} > 0$ dB in intervals of 1 dB. Also, the dashed blue line corresponds to the 0°C isotherm, the dashed orange line represents the -10°C temperature level and the dashed black line represents the -40°C level.

4.2.4 Lightning Production in the Southernmost Updraft (2004-2015 UTC)

The southernmost updraft exhibited a slower rate of electrification than the northern updraft. Through 2012 UTC, neither NALMA nor NLDN detected any type of lightning activity. Figures 4.28a and 4.28b are vertical cross-sections of Z_h with w and Z_{dr} overlaid, respectively during the 2004 UTC ARMOR volume. At 2004 UTC (Fig. 4.28a and 4.28b), the southern updraft (located ~ 65 km north of ARMOR) showed some development of a Z_{dr} column. (Z_{dr} values ~ 2 -4 dB). Collocated within the Z_{dr} column was also moderate reflectivity (45-50 dBZ) in the southern updraft (Fig. 4.28b). These values of Z_h and Z_{dr} suggested large oblate hydrometeors. The values ρ_{hv} during this volume were near unity (not shown), which indicates little to no diversity of hydrometeors. Moreover, this Z_{dr} column was confined below the 0°C level and was therefore most certainly comprised of raindrops. As a result, no supply of fresh condensate to the mixed phase region occurred. Also, it was very unlikely that any freezing of particles occurred. Furthermore, these large raindrops continued to grow due to warm cloud collision-coalescence processes. These processes have been proven to be ineffective for significant charging or lightning production (CR00). Figure 4.28a revealed that weak vertical motion ($\sim 2\text{ m s}^{-1}$) was ineffective at lofting hydrometeors into the mixed phase region and thus minimized the chance for freezing of particles. During the 2012 UTC ARMOR volume, the Z_{dr} column (3-4 dB) observed at 2004 UTC (Fig. 4.28b) extended into the 0°C to -10°C layer during the 2012 UTC ARMOR volume discussed next. The 2012 UTC ARMOR volume revealed that this region of enhanced Z_{dr} was collocated with relatively higher Z_h (55-60 dBZ) and much stronger vertical motion (~ 6 -8 m s^{-1}) (Fig. 4.29a). As a result, large oblate supercooled raindrops were lofted above the 0

°C level and the freezing processes ensued (Fig. 4.29b). Perhaps of even greater importance is the appearance of 6-8 m s⁻¹ upward vertical motion above the -10 °C level. This region is characterized by moderate Z_h (40-45 dBZ) and decreasing Z_{dr} (1-2 dB) (Fig. 4.29b). The onset of this stronger vertical motion would have supported the suspension of liquid raindrops in between the 0 °C and -10 °C layer.

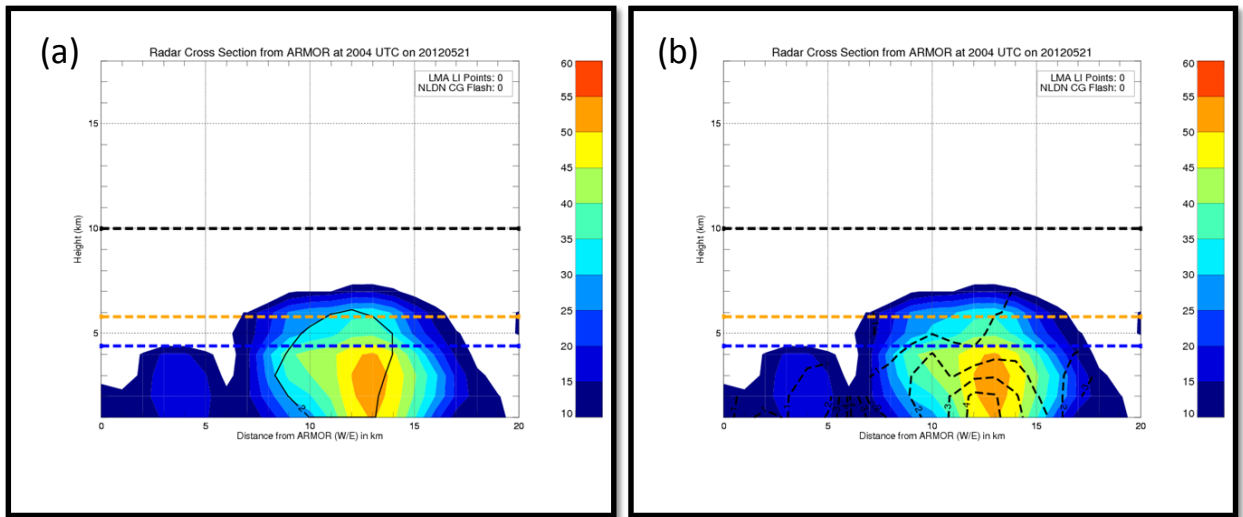


Figure 4.28. Gridded radar cross-sections in the X-Z plane roughly at 65 km north of ARMOR. The time stamps for these cross-sections are around 2004 UTC. In the left panel (a), Z_h in dBZ is the contour fill, solid black lines represent the vertical motion field in intervals of 2, 4, 6, 8, 10, 15, 20, and 25 m s⁻¹. In the right panel (b) time, the contour filled figure represents Z_h in dBZ and dashed lines represent Z_{dr} greater than 0 dB with increments of 1 dB. Also, the dashed blue line corresponds to the 0 °C isotherm, the dashed orange line represents the -10 °C temperature level and the dashed black line represents the -40 °C level.

Furthermore, a supply for condensates could be transported upward into this region of the convective cloud. Despite the appearance of this large Z_{dr} column and the improved vertical motion field, electrification of the southernmost updraft does not occur until the 2015 UTC ARMOR volume. The time series evolution of microphysics and kinematics both show a large increase in both the graupel echo volume and graupel mass (Fig. 4.25) as well as an increase in the updraft volume (Fig. 4.26) during the beginning around the 2012 UTC ARMOR volume. With a mixture of relevant ice hydrometeors

(both large in size and amount) for the NIC, efficient charging of the southern updraft likely occurred. The first lightning flash per NALMA and NLDN observations, does indeed occur within several minutes of the 2012 UTC volume time (or by 2015 UTC). Using Eqn. 2.2, CR96 demonstrated that the production of sufficient charge for lightning via NIC is possible within several minutes of first graupel in typical convective conditions.

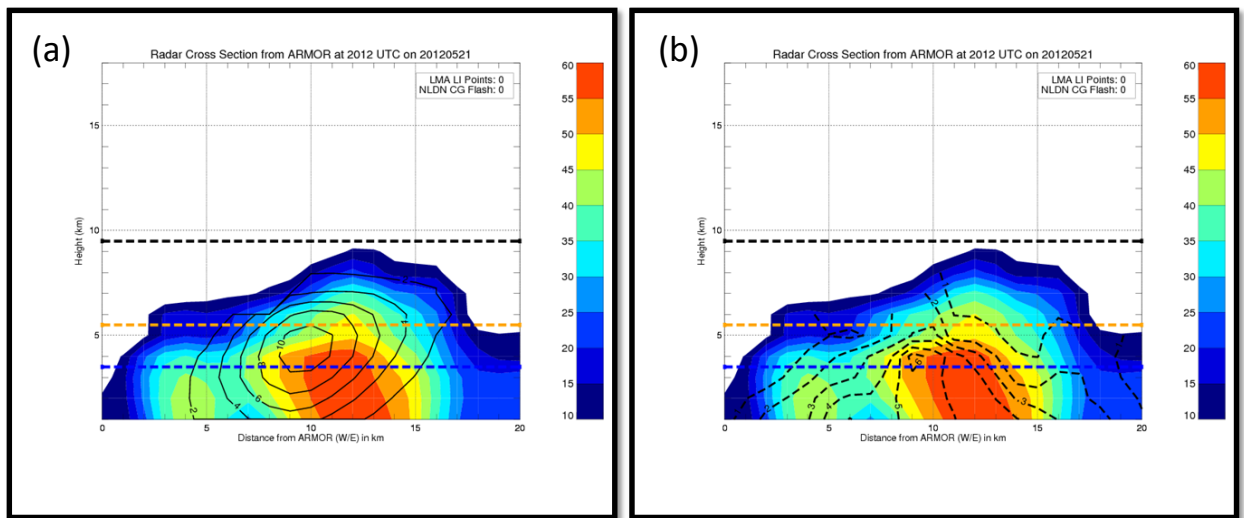


Figure 4.29. Gridded radar cross-sections in the X-Z plane roughly at 65 km north of ARMOR. The time stamps for these cross-sections are around 2012 UTC. In the left panel (a), Z_h in dBZ is the contour fill, solid black lines represent the vertical motion field in intervals of 2, 5, 10, 15, 20, and 25 m s^{-1} . In the right panel (b) time, the contour filled figure represents Z_h in dBZ and dashed lines represent Z_{dr} greater than 0 dB with increments of 1 dB. Also, the dashed blue line corresponds to the 0 °C isotherm, the dashed orange line represents the -10 °C temperature level and the dashed black line represents the -40 °C level.

4.2.5 Rapid Lightning Increase Post Updraft Merger (2015- 2023 UTC)

Over the course of the 2015 UTC ARMOR volume, the northern and southern updraft merged. As a result of the merger, the complex will now be referred to as B2. The result of this merger between the two updrafts appeared to have been constructive, as vertical motion and the total lightning increased. Peak total lightning flash rates, as inferred by NALMA, of around 5 flashes per minute occurred during this time frame

(Fig. 4.26). Peak upward vertical motion associated with the strongest updrafts ranged between 11 and 20 m s^{-1} (Fig. 4.26). More impressively, very strong upward vertical motions were observed above the $-10\text{ }^{\circ}\text{C}$ level (Fig. 4.30). Around 2015 UTC, a very rapid increase in the graupel mass and graupel echo volume occurred per the time series (Fig. 4.25).

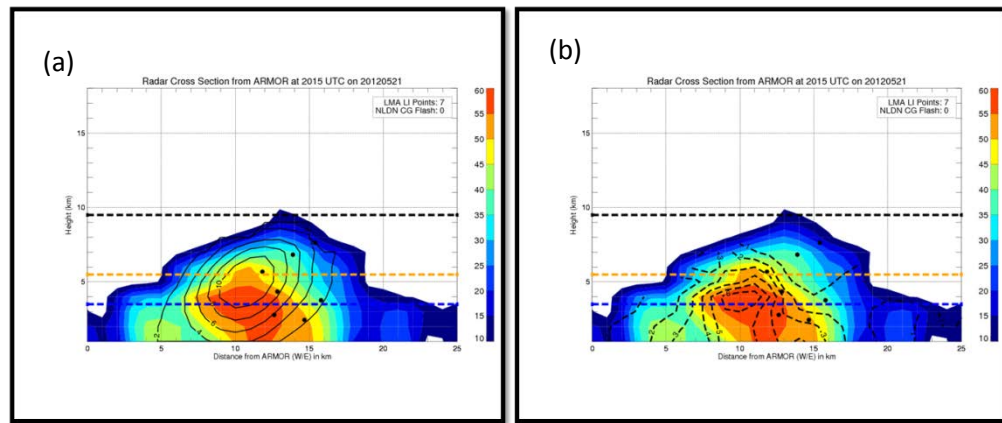


Figure 4.30. Gridded radar cross-sections in the X-Z plane roughly at 65 km north of ARMOR. The time stamps for these cross-sections are around 2015 UTC. In the left panel (a), Z_h in dBZ is the contour fill and the solid black lines represent the vertical motion field in intervals of 2, 5, 10, 15, 20, and 25 m s^{-1} . In the right panel (b), the contour filled figure represents Z_h in dBZ and dashed lines represent Z_{dr} greater than 0 dB with increments of 1 dB. Also, the dashed blue line corresponds to the $0\text{ }^{\circ}\text{C}$ isotherm, the dashed orange line represents the $-10\text{ }^{\circ}\text{C}$ temperature level and the dashed black line represents the $-40\text{ }^{\circ}\text{C}$ level. In both panels, NALMA Lightning Initiation (LI) points are denoted in the solid black circle and NLDN CG Flashes are denoted in the solid brown circle.

During this period of intensification, the amount of graupel echo volume increased by one order of magnitude with nearly a factor of four increase in the graupel mass. Radar cross-sections during 2015 UTC (Fig. 4.30a) and 2020 UTC (Fig. 4.31a) from the ARMOR radar revealed a very robust updraft, with peak velocities around 10 m s^{-1} . Estimates of strong upward vertical motion extended well into the $0\text{ }^{\circ}\text{C}$ and $-10\text{ }^{\circ}\text{C}$ layer.

An impressive Z_{dr} column, with Z_{dr} values in excess of 5 dB, through the $0\text{ }^{\circ}\text{C}$ level suggested that the updraft during the 2015 UTC ARMOR volume (Figs. 4.30a and

4.30b) was efficient at lofting large particles upward. Even more impressive was the appearance of the 50 dBZ Z_h contour through the $-10\text{ }^\circ\text{C}$ level (Figs. 4.30a and 4.30b). While strong upward vertical motions extend deeper into the mixed phase region (Fig. 4.31a), the large Z_{dr} values observed earlier above the $-10\text{ }^\circ\text{C}$ level are non-existent by 2020 UTC (Fig. 4.31b). In fact, Z_{dr} values rapidly decreased above the $-10\text{ }^\circ\text{C}$ level between the 2012 to 2020 UTC ARMOR volume (e.g., see evolution of Z_{dr} in Figs. 4.29, 4.30, and 4.31).

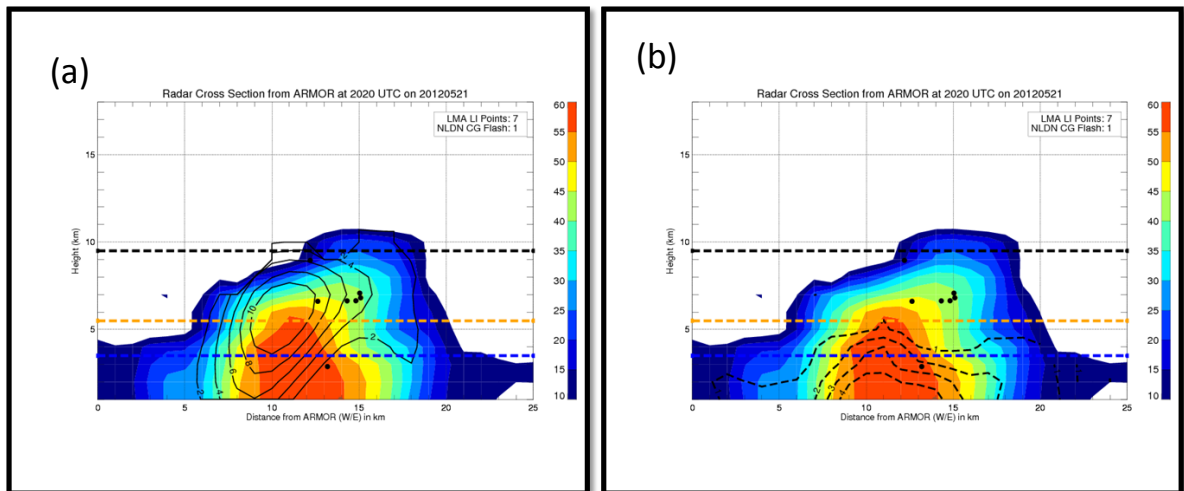


Figure 4.31. Gridded radar cross-sections in the X-Z plane roughly at 65 km north of ARMOR. The time stamps for these cross-sections are around 2020 UTC. In the left panel (a), Z_h in dBZ is the contour fill and the solid black lines represent the vertical motion field in intervals of 2, 5, 10, 15, 20, and 25 m s^{-1} . In the right panel (b), the contour filled figure represents Z_h in dBZ and dashed lines represent Z_{dr} greater than 0 dB with increments of 1 dB. Also, the dashed blue line corresponds to the $0\text{ }^\circ\text{C}$ isotherm, the dashed orange line represents the $-10\text{ }^\circ\text{C}$ temperature level and the dashed black line represents the $-40\text{ }^\circ\text{C}$ level. In both panels, NALMA Lightning Initiation (LI) points are denoted in the solid black circle and NLDN CG Flashes are denoted in the solid brown circle.

This may have suggested that a transition to all spherical and large ice particles (e.g. graupel and large hail) occurred. Moreover, the suppressed values of ρ_{hv} (not shown, but ρ_{hv} values around 0.87 at the 4.1° CAPPI from ARMOR or around 4.7 km AGL) during

this radar volume were likely a result of the Mie resonance associated with the larger ice particles. Given such large Z_h values (50 dBZ), it is likely that high density hail (perhaps large) existed in the sample volume. While the presence of large hail is not necessarily a requirement for NIC, its presence alone may be enough to infer that an increase in the size of graupel particles has occurred. This increase in the size and number of graupel particles is captured well by ARMOR and resultant diagnosis by the NCAR PID (not shown). At the 2023 UTC, B2 reached its peak in terms of total lightning flash rate from NALMA (5 flashes per minute). As expected from the NIC, there is an observed peak in both the graupel echo volume and graupel mass (Fig. 4.25) coincident with the peak in the total lightning flash rate. Radar cross-sections during the 2023 UTC frame (Figs. 4.32a and 4.32b) revealed that the mid and upper level updraft continued to strengthen with upward motions of 10 m s^{-1} well into the $-10 \text{ }^\circ\text{C}$ to $-40 \text{ }^\circ\text{C}$ layer.

Interestingly, the contours of vertical motion continued to take on a wedge shape and slope from the west to east per Figs. 4.31a and 4.32a. This likely resulted when surface outflow outpaced the main convective line. Consistent with inferences from theory from Rutunno, Klemp, and Weisman (RKW), it would appear that the updraft became less and less vertically erect (Rotunno et al. 1988). Before the complete collapse of B2, however, the stronger vertical motions become collocated with low to moderate Z_h and with Z_{dr} less than zero (Fig. 4.32b). The orientation of Z_h and Z_{dr} contours takes on a similar shape as the contours of vertical motion. It is possible that ice crystals and perhaps small graupel particles were still transported upward into colder regions of the convective cloud while larger graupel and hail particles fall under the influence of gravity. The aforementioned phenomenon would prove to be highly efficient at

separating the particles with varying terminal fall speeds and thus reinforce the already pre-existing electric field. This charge separation would result in the enhancement of the electric field and continued robust flash rates.

4.2.6 Decay and Dissipation Stages of B2 (2026 UTC-2057 UTC)

Consistent with RKW theory, the weak environmental shear resulted in an unbalanced vorticity budget between the cold pool and the ambient environment. As a result, the OFB surged south and westward ahead of the main line of convection. The inability of new parcels to be lifted up and over the gust front to their LFC resulted in a rapid decrease in vertical motion as inferred from the time series evolution of the maximum updraft velocity and updraft volume greater than 5 m s^{-1} (Fig. 4.26).

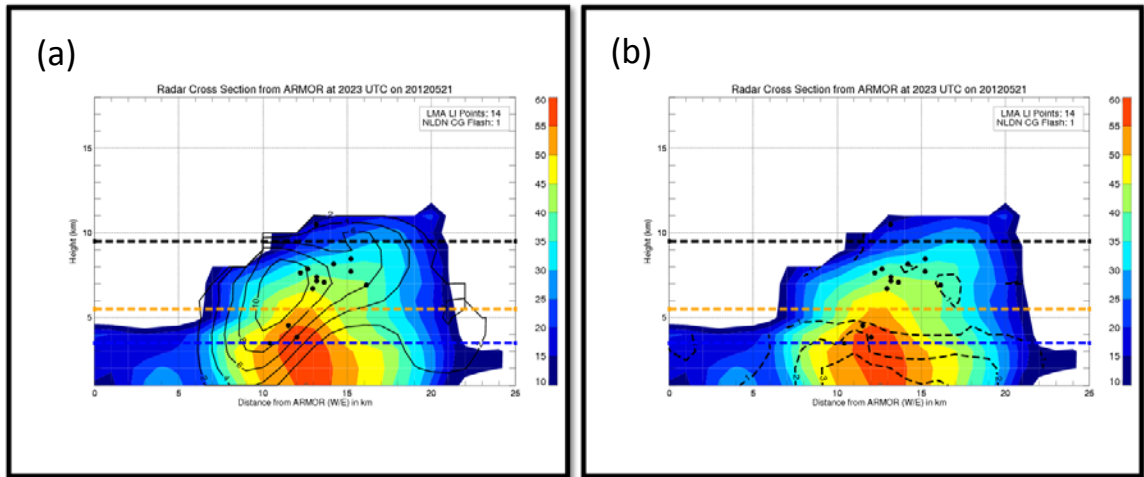


Figure 4.32. Gridded radar cross-sections in the X-Z plane roughly at 60 km north of ARMOR. The time stamps for these cross-sections are around 2023 UTC. In the left panel (a), Z_h in dBZ is the contour fill and the solid black lines represent the vertical motion field in intervals of 2, 5, 10, 15, 20, and 25 m s^{-1} . In the right panel (b), the contour filled figure represents Z_h in dBZ and dashed lines represent Z_{dr} greater than 0 dB with increments of 1 dB. Also, the dashed blue line corresponds to the $0 \text{ }^\circ\text{C}$ isotherm, the dashed orange line represents the $-10 \text{ }^\circ\text{C}$ temperature level and the dashed black line represents the $-40 \text{ }^\circ\text{C}$ level. In both panels, NALMA Lightning Initiation (LI) points are denoted in the solid black circle and NLDN CG Flashes are denoted in the solid brown circle.

This weaker convergence along the leading edge gust front appeared to be insufficient at generating additional updrafts. As a result, the weaker updrafts failed to loft and suspend larger hydrometeors. Subsequently, both Z_h and Z_{dr} decreased with time over the depth of the weakening complex. This likely decrease in hydrometeor size and concentration is manifest in the time series of graupel echo volume and graupel mass (Fig. 4.25).

Similar to complex A1, this rapid decrease is not monotonic as weak NIC or other secondary charging mechanisms may still occur within weaker upward vertical motion. The time series evolution of graupel echo volume and graupel mass (Fig. 4.25) indicate that the rate which the graupel echo volume and graupel mass decreased slowed around the 2040 UTC ARMOR volume. A very subtle increase in the total lightning flash rate, graupel echo volume and graupel mass occurred between 2040-2044 UTC. Maximum updraft velocities also exhibited a slower rate of decline when compared to that of the updraft volume. This latter point illustrates that small-scale pulses in the updrafts were enough for continued lightning production. Examination of 2044 UTC ARMOR radar cross-sections (Fig. 4.33) reveals that some residual vertical motion within the -10 °C to -40 °C layer may have supported NIC.

Furthermore, Z_{dr} values within this region characterized by Z_h of 30-40 dBZ, were less than 1 dB (Fig. 4.33 but Z_{dr} not shown). This would indicate that residual graupel and or ice particles may remain. While not as impressive as earlier in B2's lifecycle, sufficient graupel and ice particles in conjunction with vertical motion were present to produce three flashes. Deeper in the decayed convection, multi-Doppler wind synthesis revealed that vertical motion around 4 m s^{-1} still existed during the 2044 UTC ARMOR

volume (Fig. 4.33). Polarimetric radar information from ARMOR also revealed that low to moderate Z_h (30-40 dBZ) within the -10 °C to -40 °C layer and Z_{dr} less than 1 dB persisted (not shown). The latter combined with the vertical motion likely resulted in enough NIC for electrification.

Also of interest is the areal extent of these lightning flashes. The presence of precipitation-sized ice in the region of decayed convection perhaps resulted in a large reservoir of residual charge as observed in the anvils of large mesoscale convective systems (MCS) (Carey et al. 2005). As a flash was initiated within a region of weak vertical motion, it likely propagated through this region of residual charge. As the convective complex decayed, between 2048 UTC and 2114 UTC, 20 additional flashes were detected by NALMA before all lightning activity decreases. Most of these flashes occur in weaker convection and propagated back to the north, likely within residual charge layers of the decayed convection (not shown). Similar to A1, flashes that occurred toward the latter stages of B2 exhibited a much larger areal extent (20-30 km). In general, these flashes initiated outside any region of appreciable vertical motion and typically occurred in regions of low to moderate reflectivity (30-50 dBZ) and low Z_{dr} (<1 dB).

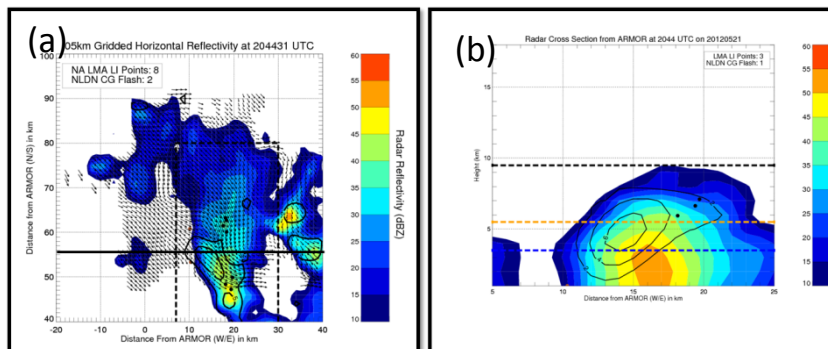


Figure 4.33. Left panel (a) represents a CAPPI at 5 km from ARMOR at 2044 UTC on 21 May 2012. The contour filled image represents Z_h in dBZ and the solid black lines represent the vertical motion field in intervals of 2, 5, 10, 15,

20, and 25 m s⁻¹. NALMA Lightning Initiation (LI) points are denoted in the solid black circle and NLDN CG Flashes are denoted in the solid brown circle. The solid black line denotes the X-Z cross-section location (around 55 km north of ARMOR). Horizontal wind vectors are plotted. The right panel (b) is a vertical cross-section in the X-Z plane taken at 55 km north of ARMOR during the same time. Contour filled image represents the horizontal radar reflectivity in dBZ and solid lines represent regions of upward vertical motion. Contour intervals for vertical motion are 2, 4, 6, 8, 10, 15, 20, 25 m s⁻¹. Also, the dashed blue line corresponds to the 0 °C isotherm, the dashed orange line represents the -10 °C temperature level and the dashed black line represents the -40 °C level.

4.3 11 June 2012 Case Day

4.3.1 Meteorological Overview

Typical of most DC3 AL days, the 11 June 2012 case day featured modest synoptic scale forcing. The 1200 UTC upper air objective analysis of the 300 hPa (Fig. 4.34) surface revealed a shortwave trough across the southern MS river valley. Upper level flow was modest with a 20-30 m s⁻¹ jet downstream from this feature. Mid-level flow weakened dramatically with observations at Nashville, TN (OHX) and Birmingham, AL (BMX) supporting around 5 m s⁻¹ winds at 500 hPa (Fig. 4.34). A deep plume of moisture as evident by the 1200 UTC KQAG RAOB (Fig. 4.35a) resulted in widespread cloud cover that infiltrated the TN valley through the early morning hours on 11 June 2012. Visible satellite imagery revealed that the expansive cloud deck began to erode just before 1600 UTC (not shown). The erosion of the cloud deck resulted in pockets of solar insolation and thus localized regions of higher instability. The 1836 UTC UAH mobile RAOB (Fig. 4.35b) was taken at NSSTC in Huntsville, AL. The RAOB revealed that sufficient solar insolation yielded SBCAPE values around 1210 J kg⁻¹ across the region. As inferred from observations at OHX and BMX, deep layer wind shear was meager and the 1836 UAH RAOB revealed that values were only on the order of 5.2 m s⁻¹. Furthermore, the 1836 UAH RAOB displayed similar characteristics to those of a tropical maritime RAOB. As a result mid-level lapse rates were typically around 5.5 °C km⁻¹.

Similar to 18 and 21 May, low-level lapse rates were steeper than those observed at the mid-levels. The sounding displayed here on 11 June 2012 is very similar to that observed by Smith et al. (1999) during the Convection and Precipitation Experiment (CaPE) across Florida. Little to no convective inhibition was observed, and given the moist regime, only sufficient solar insolation was required for thunderstorm initiation. The relatively higher 0 °C, -10 °C, and -40 °C levels, however, likely required sufficient vertical motion to loft liquid hydrometeors such that freezing subsequent electrification and lightning production could occur.

A summary of convective parameters and environmental information can be examined in Table 4.3. In general, upward motion associated with tropical like convection was generally weaker, largely in part to water loading and additional drag associated with the higher liquid water content (Rutledge et al. 1992; Williams et al. 1992). Convective complex C1 developed roughly 90 km to the north of ARMOR across eastern Marshall and western Bedford counties in southern TN. During the developing phase, ARMOR operations were primarily focused to regions south of Huntsville. As a result, no information from ARMOR is available during the developing phase of C1 from 1815 UTC through approximately 1839 UTC. During this initial phase, microphysical inferences will be made solely from the perspective of KHTX.

Table 4.3. A summary of convective parameters for the 11 June 2012 case day from the 1836 UTC UAH mobile RAOB. The RAOB was taken at the NSSTC located in Huntsville, AL.

Convective Parameter	Value
850-700 hPa lapse rate	-5.7 °C km ⁻¹
850-500 hPa lapse rate	-5.5 °C km ⁻¹
SFC-3 km lapse rate	-7.4 °C km ⁻¹
SBCAPE	1216 J kg ⁻¹
SBCIN	0 J kg ⁻¹
DCAPE	776 J kg ⁻¹
Lifted Index	-4 °C
0-6 km shear	5.2 m s ⁻¹
0 °C level	4.6 km
-10 °C level	6.2 km
-40 °C level	10.6 km

4.3.2 Developing and Initial Lightning Phase (1815-1845 UTC)

During the initial phases of C1, it is likely that very weak vertical motion, combined with a large number of small drops resulted in low Z_h and Z_{dr} values. Z_h from KHTX during the 1815 UTC volume (Fig. 4.36) revealed maximum values around 35-40 dBZ with Z_{dr} values between 0 and 0.5 dB. Values of ρ_{hv} near unity (not shown) indicated a homogenous hydrometeor volume. Given the aforementioned values of Z_h and Z_{dr} as well as environmental data from the UAH RAOB, it is likely that small water drops were present. With the maximum height of the 10 dBZ echo barely extended above the -10 °C level (6.2 km), it is possible that little to no ice particles existed during the 1815 UTC KHTX radar volume (Fig 4.36).

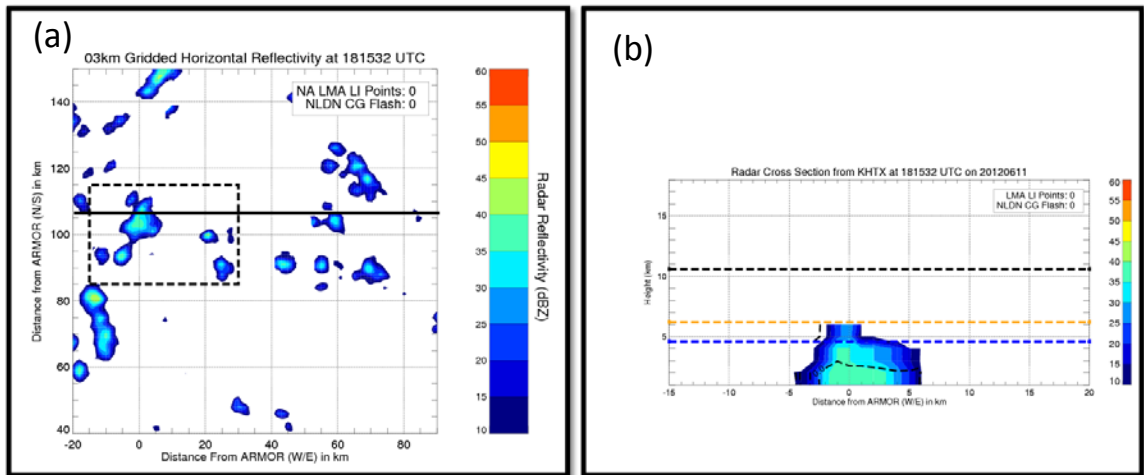


Figure 4.36. Left panel (a) represents a CAPPI at 3 km from KHTX at 1815 UTC on 11 June 2012. Right panel (b) represents a vertical cross-section at $y = 105$ km from ARMOR at 1815 UTC on 11 June 2012. For both panels contour filled regions represent Z_h in dBZ. On the right panel (b), contours of Z_{dr} (dashed line) are plotted beginning at 0 dB with 0.5 dB increments. NALMA Lightning Initiation (LI) points are denoted in the solid black circle and NLDN CG Flashes are denoted in the solid brown circle. In panel (b), the dashed blue line corresponds to the 0°C isotherm, the dashed orange line represents the -10°C temperature level and the dashed black line represents the -40°C level.

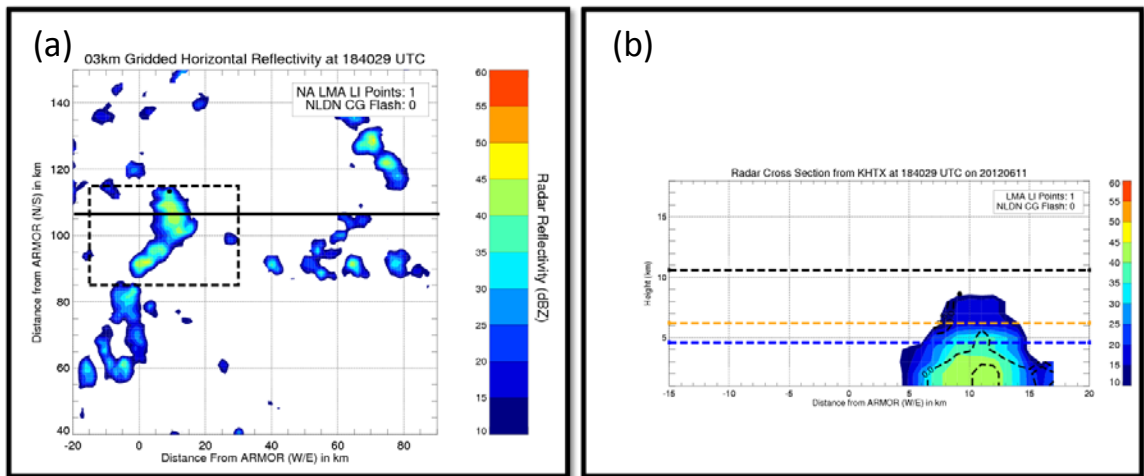


Figure 4.37. Left panel (a) represents a CAPPI at 5 km from KHTX at 1840 UTC on 11 June 2012. Right panel (b) represents a vertical cross-section at $y = 105$ km from ARMOR at 1815 UTC on 11 June 2012. For both panels, contour filled regions represent Z_h in dBZ. On the right panel, contours of Z_{dr} (dashed line) are plotted beginning at 0 dB with 0.5 dB increments. NALMA Lightning Initiation (LI) points are denoted in the solid black circle and NLDN CG Flashes are denoted in the solid brown circle. In panel (b), the dashed blue line corresponds to the 0°C isotherm, the dashed orange line represents the -10°C temperature level and the dashed black line represents the -40°C level.

This lack of ice would certainly hinder NIC and electrification. Up until the 1840 UTC KHTX volume (Fig. 4.37), C1 exhibited no lightning activity as inferred by neither

NALMA nor the NLDN. The 10 dBZ echo tops are finally beginning to reach into the -10 °C to -40 °C layer during the 1840 UTC KHTX volume. While estimates from multi-Doppler wind synthesis are not available, it may be sufficient to argue that based on the vertical extension of the 10 dB echo top that the updraft is strengthening based on KHTX radar cross-section (Fig. 4.37). Low-level Z_h and Z_{dr} values still remain on the order of 40-45 dBZ and are likely between 0.5 and 1 dB, respectively. Furthermore, the 40 dBZ Z_h contour now extends upward into the 0 °C to -10 °C layer. Z_{dr} values near 0-0.5 dB in conjunction with ρ_{hv} values near unity suggest a fairly homogenous radar sample volume of spherical hydrometeors. Closer inspection, however, of environmental data and polarimetric radar information revealed that perhaps small supercooled liquid water drops were present. Nearly instantaneous freezing of water drops over the sample radar volume would likely not occur in warm base convection at such relatively warm temperatures. Just below the -10 °C level (6 km), relatively low Z_h (35-40 dBZ) and low Z_{dr} would suggest some graupel, however.

During this phase, very subtle hints of the presence of graupel appear aloft within a region characterized by moderate Z_h (~ 40 dBZ) and low Z_{dr} . Estimates of vertical motion across this region of initial lightning activity were weak and less than 2 m s^{-1} as seen in the 5 km ARMOR CAPPI (Fig. 4.38). While speculative, it is possible that this lightning occurred in response to residual motion from an aged updraft. Moreover, this region appeared to have residual graupel and ice particles as suggested by the NCAR PID. NALMA flash rates were low during this time with less than a flash per minute. Around 1844 UTC vertical motion increased within the 0 °C to -10 °C layer.

Polarimetric information across this region also revealed that this region was characterized by moderate Z_h on the order of 40 to 45 dBZ with Z_{dr} between 0.5 to 1 dB. A subtle decrease in ρ_{hv} (0.97) would suggest a mixture of hydrometeors (not shown). It may be plausible that very small ice particles such as graupel existed.

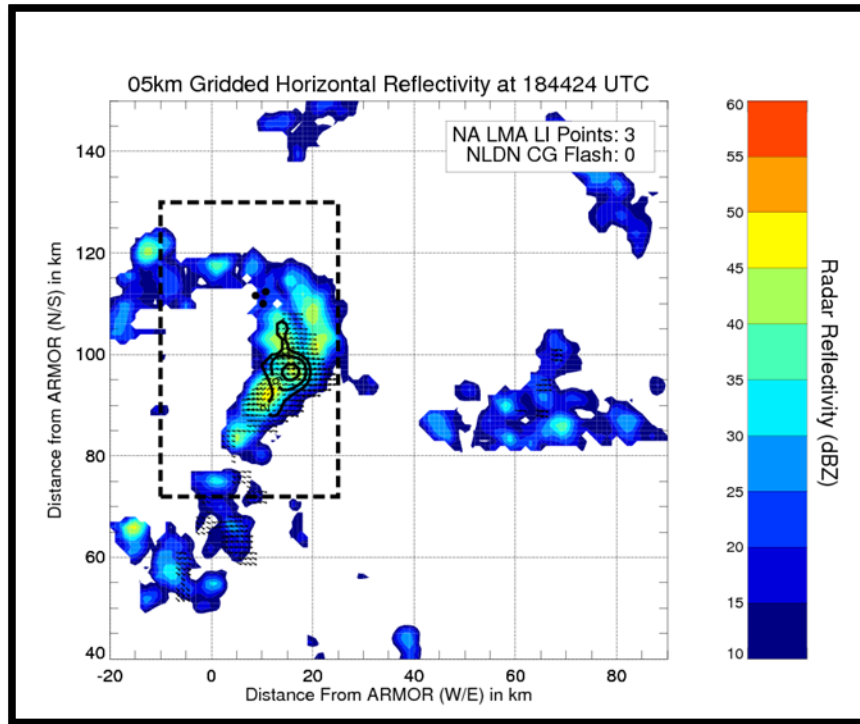


Figure 4.38. This figure depicts a CAPPI at 5 km from ARMOR at 1844 UTC on 11 June 2012. Contour filled regions represent Z_h in dBZ, solid black lines represent the vertical motion field in intervals of 2, 5, 10, 15, 20, and 25 m s^{-1} . NALMA Lightning Initiation (LI) points are denoted in the solid black circle and horizontal wind vectors are plotted.

4.3.3 Continued Lightning (1854 UTC)

New graupel production in conjunction with possible residual charge from previous convective updrafts may be sufficient enough to explain the continued electrical activity in this region. During the 1854 UTC ARMOR volume, NALMA detected a cluster of 7 flashes along the northern edge of the updraft that developed roughly 100 km north and 20 km east of ARMOR. Comparison of the 5 and 9 km CAPPI's (Fig. 4.39)

during the 1854 UTC ARMOR volume revealed a slight northward tilt of the region of greatest vertical motion. Multi-Doppler wind synthesis revealed that airflow at 5 km was generally out of the west and southwest, while aloft (9 km) the winds backed to the south.

The 5 km updraft was broad with a large area of $2\text{-}5\text{ m s}^{-1}$. Aloft, however, the areal extent of the maximum in the vertical motion was much more compact. The relatively higher $0\text{ }^{\circ}\text{C}$ and $-10\text{ }^{\circ}\text{C}$ level both suggested a large warm cloud depth, typical of tropical environments. Intuitively, these updrafts were likely not as efficient at transporting large quantities of new condensates upward into the mixed phase region owing to their weaker vertical motions (Rutledge et al. 1992; Williams et al. 1992). As the flow aloft backed to the south, it appears that a large quantity of ice particles were likely advected towards the north and northeast. It is likely that amongst these charged ice particles that lightning was the most prevalent during this radar volume.

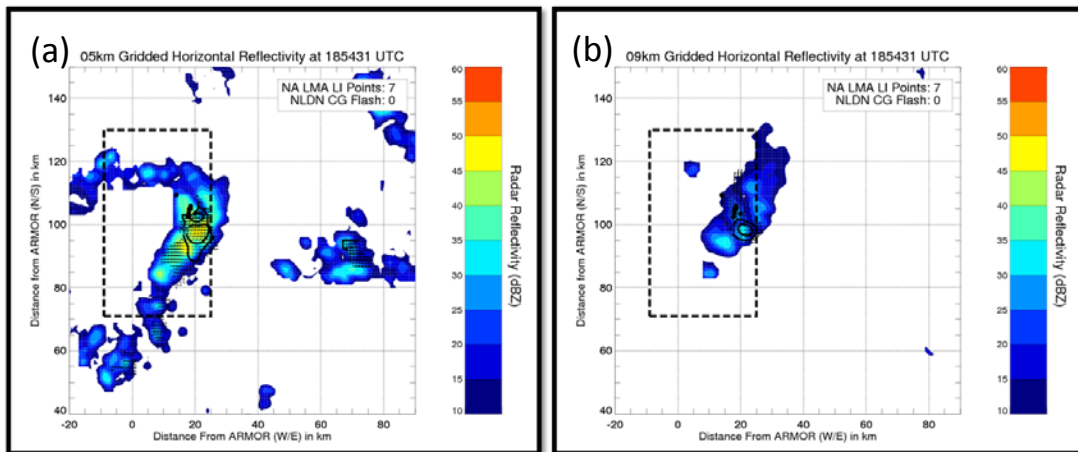


Figure 4.39. Left panel (a) represents a CAPPI at 5 km from ARMOR at 1854 UTC on 11 2012. Right panel (b) represents a CAPPI at 9 km from ARMOR at 1854 UTC on 11 June 2012. For both images, contour filled regions represent Z_h in dBZ, solid black lines represent the vertical motion field in intervals of 2, 5, 10, 15, 20, and 25 m s^{-1} . NALMA Lightning Initiation (LI) points are denoted in the solid black circle and horizontal wind vectors are plotted.

4.3.4 Increasing Lightning (1859-1928 UTC)

During the 1859 UTC and 1904 UTC ARMOR radar volumes, a quick increase in the graupel echo volume and graupel mass occurred in concert with an increase in the vertical motion (Figs. 4.40, 4.41). Maximum updraft velocities and updraft volume $> 5 \text{ m s}^{-1}$ in the mixed phase region both show an increase by a factor of two with total lightning flash rates increasing to just under 2 flashes per minute. Trends between kinematic and microphysical parameters and lightning can be examined in the time series plots provided in Figs. 4.40 and 4.41.

Through the 1859 UTC ARMOR volume, convective complex C1 moved eastward and became more much more energetic with a large increase in the radar reflectivity echo volume through the mixed phase region and an increase in the upward vertical motion (Figs. 4.40, 4.41). Stronger updrafts have resulted in enhanced Z_{dr} of around 2 dB with Z_h as high as 50 dBZ as high as 2 km into the mixed phase zone (not shown). This would suggest lofting of medium to large liquid rain drops occurred from the warm cloud layer to around 2 km into the mixed phase region. From Fig. 4.41, it would appear that freezing and riming of graupel is delayed as the sharp increase in both the graupel echo volume and mass occurred closer to the 1904 UTC and 1914 UTC ARMOR volume. The graupel echo volume continued to increase rapidly during this time period with a change of more than a factor of six between 1909 UTC and 1928 UTC. Similarly, the graupel mass increased by an order of magnitude during this same time frame (Fig 4.41).

C1 continues to grow through the 1909 UTC ARMOR volume (Fig. 4.42a). The vertical cross-section (Fig. 4.42b) through a portion of C1 (located around 100 km north of ARMOR) revealed that a rapid decrease of Z_{dr} to near 0 dB with low to moderate Z_h around 25-30 dBZ in the mixed phase zone occurred during the 1909 UTC ARMOR volume. The NLDN also detected a few CG flashes within the main convective core during this time as well. Just before 1930 UTC, C1 attained one of its maxima in total lightning flash rate. Coincident with this peak in the total lightning flash rate is a peak in the graupel echo volume and graupel mass (Fig 4.41).

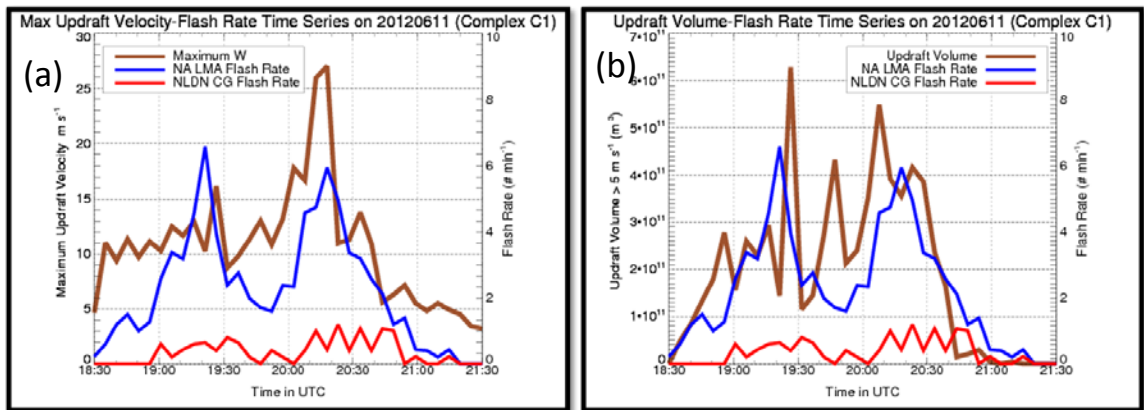


Figure 4.40. Co-evolution of kinematic and electrical properties for C1 on 11 June 2012. Left panel (a) represents the time series evolution of the maximum updraft velocity (solid brown line) as determined from multi-Doppler wind synthesis within the $-10\text{ }^{\circ}\text{C}$ and $-40\text{ }^{\circ}\text{C}$ temperature levels and the total lightning flash rate as inferred from NALMA. The dashed brown line represents the maximum updraft velocity within the $-10\text{ }^{\circ}\text{C}$ and $-40\text{ }^{\circ}\text{C}$ temperature layer and the solid blue line represents the total lightning flash rate as inferred from NALMA. The solid red line represents the NLDN inferred CG flash rate. The right panel (b) represents the time series evolution updraft volume greater than 5 m s^{-1} (solid brown line) within the $-10\text{ }^{\circ}\text{C}$ and $-40\text{ }^{\circ}\text{C}$ temperature levels and the total lightning flash rate (solid blue line) as inferred from NALMA. The solid red line represents the NLDN inferred CG flash rate.

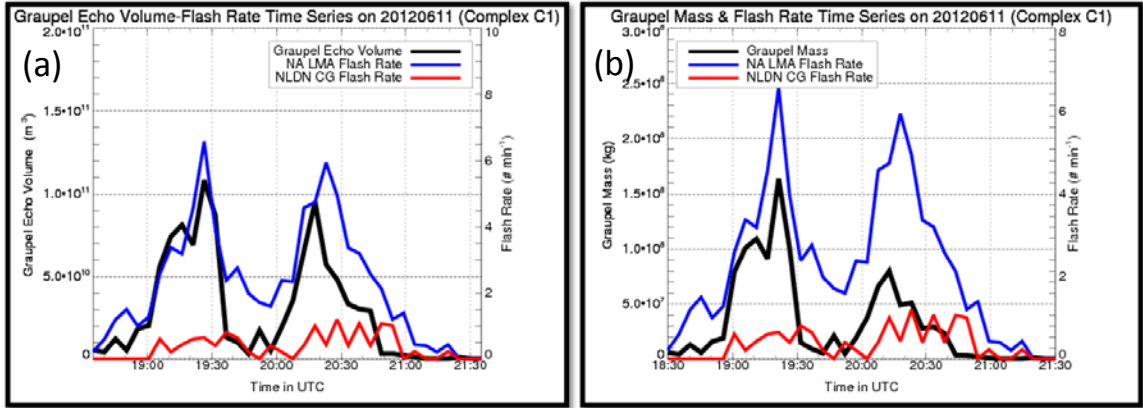


Figure 4.41. Time series evolution of DMC microphysics and electrical properties for complex C1 on 11 June 2012. The left panel (a) represents the time series evolution of graupel echo volume (solid black line) within the -10°C and 40°C temperature layer and total lightning flash rate as inferred from NALMA (solid blue line). The solid red line denotes the CG lightning flash rate as determined by NLDN. The right panel (b) represents the graupel mass (solid black line) within the -10°C and -40°C temperature layer and the total lightning flash rate as inferred from NALMA (solid blue line). The solid red line denotes the CG lightning flash rate as determined by NLDN.

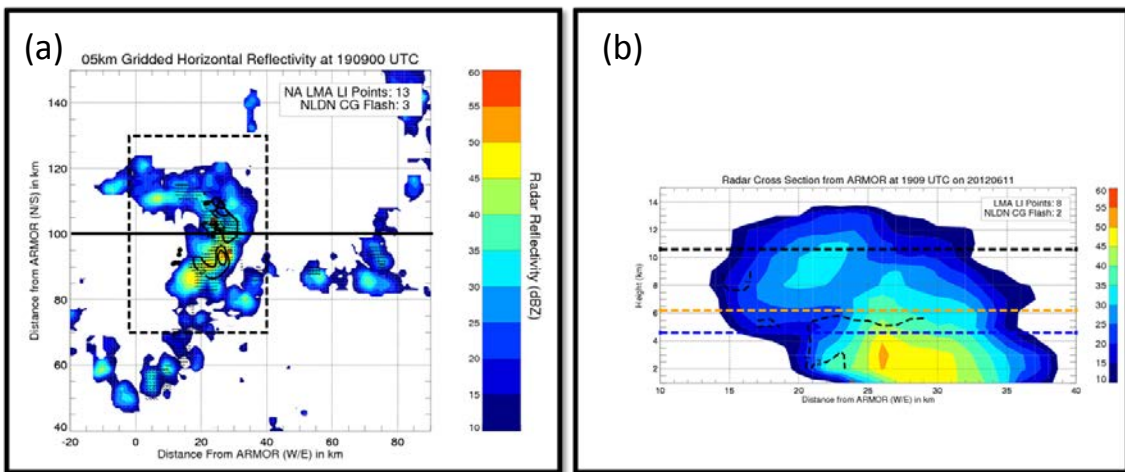


Figure 4.42. Left panel (a) represents a CAPPI at 5 km from ARMOR at 1909 UTC on 11 June 2012. The contour filled image represents the horizontal radar reflectivity in dBZ and the solid black lines represent the vertical motion field in intervals of 2, 5, 10, 15, 20, and 25 m s^{-1} . NALMA Lightning Initiation (LI) points are denoted in the solid black circle and NLDN CG Flashes are denoted in the solid brown circle. The solid black line denotes the X-Z cross-section location (around 100 km north of ARMOR). Horizontal wind vectors are plotted. The right panel (b) is a vertical cross-section in the X-Z plane taken at 100 km north of ARMOR during the same time. Contour filled image represents the horizontal radar reflectivity in dBZ and solid lines represent regions of upward vertical motion. Contour intervals for vertical motion are 2, 4, 6, 8, 10, 15, 20, 25 m s^{-1} . Also, the dashed blue line corresponds to the 0°C isotherm, the dashed orange line represents the -10°C temperature level and the dashed black line represents the -40°C level.

4.3.5 Decreasing Lightning Activity (1933- 1958 UTC)

A decrease in the lightning activity of C1 occurred between 1933 UTC and 1958 UTC time period. Observations from NALMA indicate that the flash rate decreased from a relative maximum of 6 flashes per minute to below 2 flashes per minute during this 25-minute window. As expected from the NIC mechanism, this decrease in total lightning corresponded with a decrease in the graupel mass and volume (Fig 4.41). Outside of a large “pulse” around 1950 UTC, the updraft volume showed a steady decline indicative of a weakening vertical motion field (Fig 4.40). In fact, a rapid decrease in the maximum updraft velocity and updraft volume occurred nearly simultaneously with the decrease in the graupel mass and graupel echo volume (Figs 4.40 and 4.41). The lack of upward vertical motion in combination with the lack of large ice particles (specifically graupel) would likely explain the decrease in the total lightning flash rate. Low-level radar reflectivity values are modest with peak values through 1948 UTC around 50-55 dBZ (not shown). While maximum updraft values appeared to remain around 10 m s^{-1} the large decrease in graupel mass and graupel echo volume likely hindered sufficient NIC necessary to maintain the relatively higher flash rates observed during the earlier stages of C1’s lifecycle. Specifically, the graupel mass and graupel echo volume plummeted quite rapidly (Fig 4.41). These relative minima in graupel echo volume and graupel mass corresponded to the minimum in NALMA inferred lightning activity. Observations from the NLDN suggest that occasional cloud-to-ground flashes occur during this time period (Fig 4.41).

4.3.6 Increasing Lightning Part II (2000 UTC – 2030 UTC)

Around the 2003 UTC ARMOR volume, the upward vertical motion field increased rapidly (Fig. 4.40). Similarly, the graupel echo volume also showed an increase (Fig. 4.41). Upward vertical motion along the main convective line and within the lower Z_h region increased up to 10-15 m s^{-1} , which is capable of lofting liquid hydrometeors upward into the mixed phase region (not shown). Perhaps of equal importance was the increase in the depth of the vertical motion through the $-10\text{ }^{\circ}\text{C}$ to $-40\text{ }^{\circ}\text{C}$ layer. The continued upward vertical motion likely lofted liquid particles into the mixed phase region, allowing coalescence freezing and riming of graupel for NIC. More importantly, the relatively higher displacement of ice crystals when compared to graupel particles likely resulted in sufficient storm-scale charge separation for the continued generation of an electric field and subsequent lightning. During peak flash rates of around 5-6 flashes per minute, the graupel mass showed a quick order of magnitude increase (Fig. 4.41).

4.3.7 Decaying Phase (2030 UTC -2100 UTC)

During the decay phase, the overall depth of the largest vertical motion appeared to decrease. As a result, the suspension of particles within the mixed phase regions gradually ceased and particles began to fall under the influence of gravity. This particle fallout was manifest in the decrease in both the graupel echo volume and graupel mass (Fig. 4.41). Interestingly enough, the NLDN detected CG lightning persisted during this period of decline in both the graupel mass and graupel echo volume in the $-10\text{ }^{\circ}\text{C}$ and $-40\text{ }^{\circ}\text{C}$ level. Consistent with previous studies, it is possible that the descent of graupel and/or

small hail below the melting level enhanced the occurrence of CG lightning. Around 2130 UTC, however, all lightning associated with C1 ended.

4.4 14 June 2012

4.4.1 Meteorological Overview

The final case day examined for this data set will be 14 June 2012. Typical of AL DC3 case days, large scale synoptic forcing was weak. The 1200 UTC objective upper air analysis revealed that a weak shortwave trough extended from southwestern TN down through adjacent portions of MS, AR and northern LA (not shown). The 1200 UTC KQAG RAOB (Fig. 4.43a) revealed a strong surface inversion likely a result of nocturnal cooling.

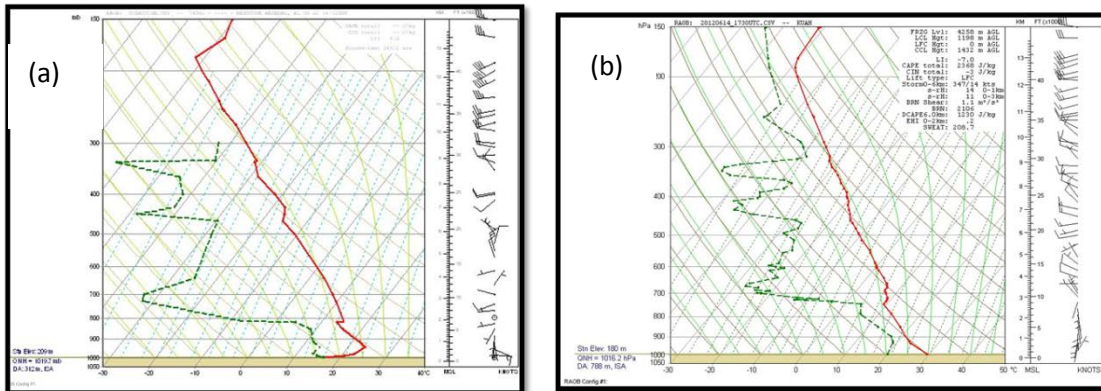


Figure 4.43. Comparison of 1200 UTC RAOB from Redstone Arsenal, AL (a) on 14 June 2012 and 1730 UTC UAH mobile RAOB (b) taken from near Guntersville, AL.

Above this inversion, however, lapse rates were modest and with values on the order of $-6.5 \text{ }^\circ\text{C km}^{-1}$. Southeasterly winds allowed for moisture advection primarily east of Huntsville along the spine of the higher terrain (now shown). The 1730 UTC UAH mobile RAOB (Fig. 4.43b) taken near Guntersville, AL revealed that the air-mass east of Huntsville was conditionally unstable with low-level (0-3 km) lapse rates on the order of

-7.3 C km⁻¹. Deep layer shear was weak and less than 1 m s⁻¹. While vertical wind shear was weak, instability was high with the RAOB indicating that SBCAPE values were in excess of 2,000 J kg⁻¹ across the region (Fig 4.43b). DCAPE values exceeded 1,000 J kg⁻¹ likely supported strong downdrafts efficient at producing outflow conducive for additional cell development. As a result of the kinematic and thermodynamic profiles from the UAH RAOB, multicellular convection was anticipated. Additional information on relevant thermodynamic parameters can be found in Table 4.4.

Table 4.4. A summary of convective parameters for the 14 June 2012 case day from the 1730 UTC UAH mobile RAOB. The RAOB was taken near Guntersville, AL.

Convective Parameter	Value
850-700 hPa lapse rate	-6.2 °C km ⁻¹
850-500 hPa lapse rate	-6.5 °C km ⁻¹
SFC-3 km lapse rate	-7.4 °C km ⁻¹
SBCAPE	2368 J kg ⁻¹
SBCIN	-3 J kg ⁻¹
DCAPE	1230 J kg ⁻¹
Lifted Index	-7 °C
0-6 km shear	0.3 m s ⁻¹
0 °C level	4.4 km
-10 °C level	5.8 km
-40 °C level	10.0 km

The initial cumulus field developed around 1530 UTC across the higher terrain of northern AL. With the strong instability and the weak inhibition observed in the 1730 UTC UAH RAOB, rapid development of DMC ensued shortly before 1600 UTC. Convective complex D1 developed roughly 90-100 km east of ARMOR and began producing lightning very quickly following initiation. It should be noted that throughout the entire lifecycle of D1, KHTX operated in VCP 21 due to maintenance being performed on the radar. Also, for a short time period, VCP 32 was employed for reasons

unknown. Importantly, the large elevation stepping and relatively longer temporal updates result in the inability for accurate estimates of vertical motion. While estimates of vertical motion are unavailable, polarimetric information can be used to make inferences about vertical motion.

4.4.2 Developing Stage and Initial Lightning Activity (1600-1610 UTC)

Explosive growth of cell D1 occurred during the first 5 to 10 minutes of its lifecycle. In between 1610 UTC and 1615 UTC, NALMA detected 5 lightning flashes. Also, NLDN detected 3 CG lightning flashes (Fig 4.44). Relatively moderate Z_h (50-55 dBZ) and moderate Z_{dr} (~ 1 dB) values were observed below the 0 °C level from KHTX. Given environmental information from the 1730 UTC UAH mobile RAOB, the mixture likely consisted of supercooled drops, graupel and hail. With relatively large Z_h aloft, it is likely that sufficient vertical motion was able to loft particles deep into the mixed phase region.

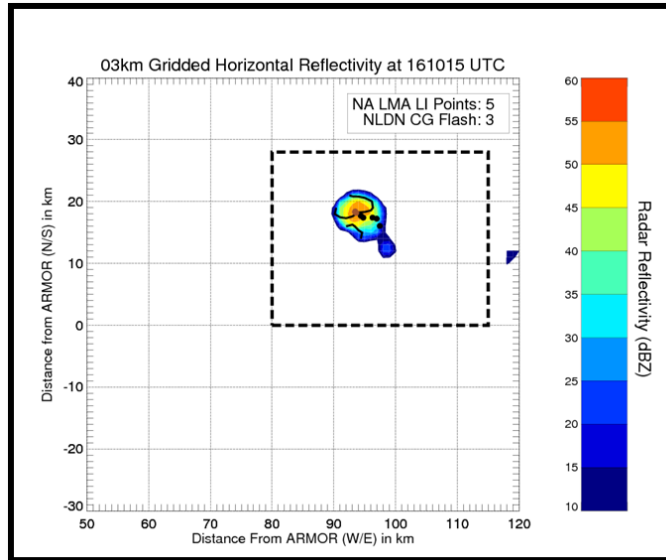


Figure 4.44. A CAPPI at 3 km from ARMOR at 1610 UTC on 14 June 2012. Contour filled image represents the horizontal radar reflectivity in dBZ. NALMA Lightning Initiation (LI) points are denoted in the solid black circle and NLDN CG Flashes are denoted in the solid brown circle.

4.4.3 Rapid increase in Lightning Production (1628 UTC-1652 UTC)

A rapid increase in the lightning production within D1 occurred from 1628 to 1652 UTC as seen in a time series evolution of microphysical and electrical properties (Fig. 4.45). This increase in lightning is thought to have occurred in response to NIC. Just above the 0 °C level, ARMOR Z_h was large around 60-65 dBZ and Z_{dr} less than 1 dB in cell D1 near what appeared to be the updraft at 1628 UTC (Fig. 4.46).

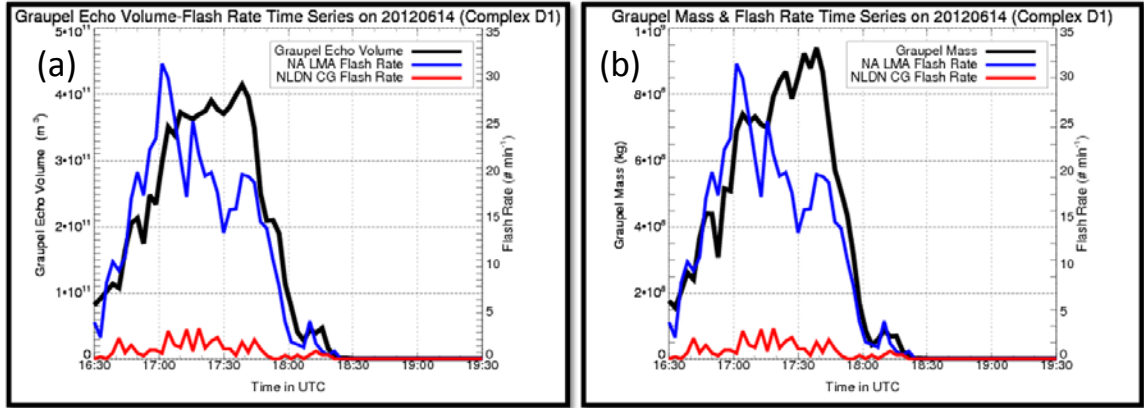


Figure 4.45. Time series evolution of DMC microphysics and electrical properties for complex D1 on 14 June 2012. The left panel (a) represents the time series evolution of graupel echo volume (solid black line) within the -10°C and -40°C temperature layer and total lightning flash rate as inferred from NALMA (solid blue line). The solid red line denotes the CG lightning flash rate as determined by NLDN. The right panel (b) represents the graupel echo volume (solid black line) within the -10°C and -40°C temperature layer and the total lightning flash rate as inferred from NALMA (solid blue line). The solid red line denotes the CG lightning flash rate as determined by NLDN.

Lowered values of ρ_{hv} (0.90) (not shown) were collocated with the aforementioned values of Z_{h} and Z_{dr} that suggested a mixture of hydrometeors. A tight gradient in Z_{dr} existed as the column nudged deeper into the mixed phase region during the 1628 UTC ARMOR volume (Fig. 4.46a and 4.46b). Similar to previous DC3 AL days, this signature in Z_{dr} and ρ_{hv} was indicative of a sharp transition from oblate (supercooled rain drops or a rain and frozen drop mixture) to mostly spherical hydrometeors (purely hail/graupel mixture). During this time period, output from the NCAR PID suggested a mixture of hail, graupel, and supercooled liquid water may have existed in the radar volume. Gridded cross-sections during the 1628 ARMOR volume (Fig. 4.46b) time revealed a persistent Z_{dr} column, which indicated the region of the updraft (Kumjian et al. 2012). While vertical motion was not readily available due to the lack of multi-Doppler wind synthesis, the inferred presence of hail above the 0°C level suggested that an updraft of sufficient

magnitude was present. With the combination of favorable kinematics and microphysical conditions, a rapid increase in lightning production occurred.

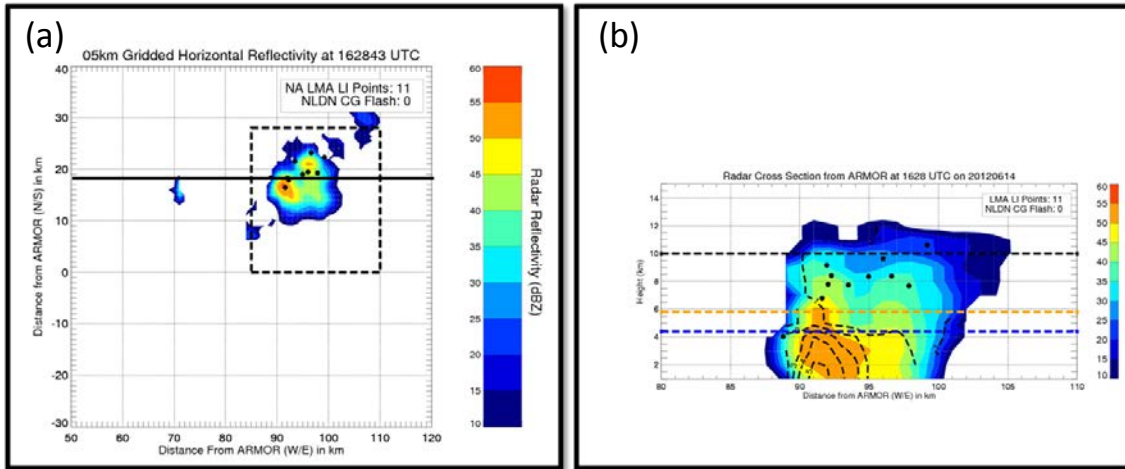


Figure 4.46. Left panel (a) represents a CAPPI at 5 km from ARMOR at 1628 UTC on 14 June 2012. The contour filled image represents the horizontal radar reflectivity in dBZ. NALMA Lightning Initiation (LI) points are denoted in the solid black circle and NLDN CG Flashes are denoted in the solid brown circle. The solid black line denotes the X-Z cross-section location (around 18 km north of ARMOR). The right panel (b) is a vertical cross-section in the X-Z plane taken at 18 km north of ARMOR during the same time. Contour filled image represents the horizontal radar reflectivity in dBZ. Also, the dashed blue line corresponds to the 0 °C isotherm, the dashed orange line represents the -10 °C temperature level and the dashed black line represents the -40 °C level.

Over the course of the 1628 UTC ARMOR volume, NA measured flash rates that were just above 3 flashes per minute. During the 1652 UTC ARMOR volume (Fig. 4.47a and 4.47b), D1 consisted of a few convective elements. The convective element of interest is denoted in Fig. 4.47a. Over the course of the 1652 UTC ARMOR volume, the total lightning flash rate increased to nearly 20 flashes per minute. A large quantity of the lightning during this radar volume (1652-1656 UTC) occurred aloft along a gradient in Z_h around 10 km. This region was comprised of low $Z_{dr} < 1$ dB as well (Fig 4.47b). This gradient in Z_h suggested a change in the size of particles with height. As a result, this gradient is in large part due to the separation between small particles (ice crystals) and larger particles (graupel particles).

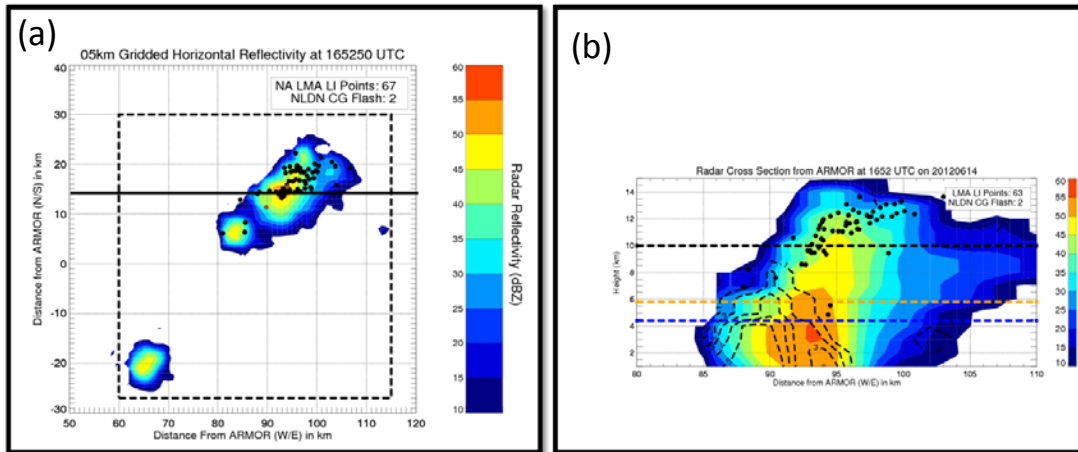


Figure 4.47. Left panel (a) represents a CAPPI at 5 km from ARMOR at 1652 UTC on 14 June 2012. Contour filled image represents the horizontal radar reflectivity in dBZ. NALMA Lightning Initiation (LI) points are denoted in the solid black circle and NLDN CG Flashes are denoted in the solid brown circle. The solid black line denotes the X-Z cross-section location (around 15 km north of ARMOR). The right panel (b) is a vertical cross-section in the X-Z plane taken at 15 km north of ARMOR during the same time. Contour filled image represents the horizontal radar reflectivity in dBZ. Also, the dashed blue line corresponds to the 0 °C isotherm, the dashed orange line represents the -10 °C temperature level and the dashed black line represents the -40 °C level.

During this time period (1652 UTC-1656 UTC) the graupel echo volume and graupel mass (Fig 4.45) both increased by nearly a factor of 3. This increase in graupel echo volume and graupel mass as well as lightning activity was indicative of a strengthening updraft consistent with Deierling and Petersen (2008). During this time period, the NLDN records a total of 19 CG flashes. While a relatively high number of CG flashes were observed during this time frame, it should be pointed out that the total number of IC flashes from NALMA was around 262. This ratio favoring a larger number of IC's was consistent with other storms explored during DC3 AL.

4.4.4. Peak Lightning Production (1703 UTC-1709 UTC)

Lightning activity peaked during this time frame with NALMA indicating that the total lightning flash rate was just over 30 flashes per minute around 1703-1706 UTC. This total lightning flash rate was the highest of any DC3 AL storm analyzed thus far. An

examination of radar information from ARMOR revealed that moderate to high Z_h (60 dBZ) and low Z_{dr} (near 0 dB) extended well into the $-10\text{ }^\circ\text{C}$ to $-40\text{ }^\circ\text{C}$ level. During the 1703 UTC ARMOR radar volume (~ 3 minute radar volume), NALMA detected 108 lightning flashes (Fig. 4.48a). More impressively, is the 50 dBZ Z_h contour that extended up through 12 km during the 1706 UTC ARMOR volume as seen in Fig. 4.48b

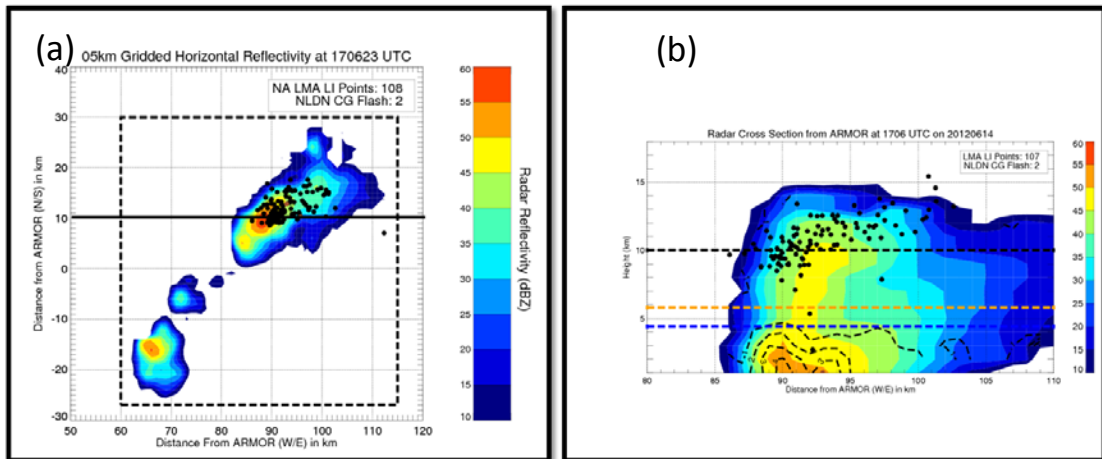


Figure 4.48. Left panel (a) represents a CAPPI at 5 km from ARMOR at 1706 UTC on 14 June 2012. Contour filled image represents the horizontal radar reflectivity in dBZ. NALMA Lightning Initiation (LI) points are denoted in the solid black circle and NLDN CG Flashes are denoted in the solid brown circle. The solid black line denotes the X-Z cross-section location (around 10 km north of ARMOR). The right panel (b) is a vertical cross-section in the X-Z plane taken at 10 km north of ARMOR during the same time. Contour filled image represents the horizontal radar reflectivity in dBZ. Also, the dashed blue line corresponds to the $0\text{ }^\circ\text{C}$ isotherm, the dashed orange line represents the $-10\text{ }^\circ\text{C}$ temperature level and the dashed black line represents the $-40\text{ }^\circ\text{C}$ level.

The Z_h and Z_{dr} structure in Fig 4.48b suggested the presence of a very robust updraft capable of lofting large hydrometeors through the depth of the mixed phase region and well above the level of $-40\text{ }^\circ\text{C}$. In fact, the graupel echo volume and the graupel mass both increase (Fig. 4.45). During this time period, NALMA observed a total 364 flashes with the NLDN recorded a total of 8 CG flashes.

4.4.5 Decline in Lightning Production (1713-1800 UTC)

The total lightning flash rate showed an initial decrease around 1713 UTC. Interestingly enough, the production of graupel echo volume and graupel mass continued to show a steady increase (Fig. 4.45). The decrease in total lightning flash rate suggested a weakening of the updraft per Deierling and Petersen (2008). Moreover, it is plausible that this de-correlation occurred as a result of graupel and other ice particles remaining suspended even after the updraft has weakened. Eventually, as the updraft continued to weaken, the ability to supply fresh condensates into the mixed phase region decreased. As a result, the ability for NIC to take place decreased as well. Also there were several instances in which the total lightning flash rate increased for a short time period (e.g., 1723 UTC, 1744 UTC). It is suggested that the pulse-like nature of this convection resulted in a non-monotonic decrease in lightning properties during these short changes in intensity. At 1747 UTC, a monotonic decrease in the total lightning flash rate and microphysical information was consistent with a decrease in the strength of the updrafts. More importantly, the lack of NIC was clearly manifest in this rapid decline in lightning activity of D1.

CHAPTER FIVE

DISCUSSION

5.1 Discussion of DC3 AL Case Days

As mentioned during the beginning of the results section, most of the DC3 AL case days were weakly forced from a synoptic standpoint with very little shear with similar amounts of instability. Most DC3 case days could be characterized as those having less than 1200 J kg^{-1} of CAPE with the exception to this rule is the 14 June 2012 case in which the instability could be characterized as high ($+2300 \text{ J kg}^{-1}$). As highlighted in the summaries above, the lack of sufficient deep layer shear facilitated primarily ordinary, multicellular convection. Within these multicellular complexes, individual convective elements were short-lived, but often contributed to the overall lightning production of the complex as a whole. This concept was also illustrated in the radar summaries. The overall magnitude of these individual updrafts is likely tied to the amount of instability. Numerous observational studies have related the amount of CAPE to the magnitude of the updraft. Table 4.5 provides a summary of comparisons between observed CAPE values, maximum vertical motion from multi-Doppler wind synthesis and peak observed total lightning flash rate.

Table 4.5. Comparison of thermodynamic, electrical, and kinematic properties during DC3 AL. Estimates of vertical motion are not available from the 14 June 2012 case (D1).

DC3 AL Complex	SBCAPE (J kg ⁻¹)	DCAPE (J kg ⁻¹)	Peak Total Lightning Flash Rate (flash min ⁻¹)	Total Lightning Flash Count (CG)	Peak CG Lightning Flash Rate (flash min ⁻¹)	Maximum Vertical Velocity (m s ⁻¹)	Maximum Updraft Volume > 5 m s ⁻¹ (m ³)
A1	1270	950	20.0	778 (9)	0.25	21.0	4.4 x 10 ¹¹
B1	785	702	1.1	6 (3)	0.36	11.0	1.0 x 10 ¹¹
B2	785	702	5.0	111 (19)	1.1	19.9	4.69 x 10 ¹¹
C1	1216	776	6.57	396 (61)	1.1	27.0	6.28 x 10 ¹¹
D1	2368	1230	31.3	1657(112)	3.2	--	--

As expected, information from Table 4.5 would suggest that there is a correspondence between SBCAPE values and peaks in both the total lightning flash rate and total lightning flash counts. Consistent with observations from Williams (2001), a larger amount of SBCAPE generally resulted in a higher total lightning flash rate (One exception appears to occur when one compares A1 and C1). While similar values of SBCAPE were observed for these two case days (A1 and C1), it should be noted that steeper low- and mid-level lapse rates were evident on 18 May 2012 (A1), which likely facilitated a stronger updraft. This stronger updraft was likely able to loft liquid particles into the mixed phase region for coalescence freezing as well as being able to provide a supply of condensate into the mixed phase region for riming and ultimately NIC. Moreover, the relatively larger warm cloud depth associated with C1 when compared to A1 would likely suggest that the efficiency at generating large precipitation ice particles was generally lower, thereby resulting in a lower total lightning flash rate. Elementary parcel theory notes that square root of the CAPE could be thought of as an idealized upper limit on the maximum updraft velocity. This formulation is idealized due to the fact that parcel theory neglects water loading and mixing with the ambient environment. Numerous observational studies for example, have noted that updrafts tended to be

weaker in tropical like environments as a direct result of the higher liquid water content. While not technically a tropical environment, a few cases here across DC3 AL exhibited tropical convection-like traits. The most dominant trait would be the low flash rates.

In addition, relationships between estimated updraft velocities (from multi-Doppler) and the total lightning flash rate have been explored. As mentioned previously, Deierling and Petersen (2008) showed that total lightning could be a useful indicator of the overall magnitude of the updraft (e.g., updraft volume and total lightning flash rate). From Table 4.5, similar magnitudes of maximum vertical velocities and maximum updraft volume $> 5 \text{ m s}^{-1}$ within the $-10 \text{ }^{\circ}\text{C}$ and $-40 \text{ }^{\circ}\text{C}$ layer occurred across DC3 AL. For this dataset, there does not appear to be a consistent trend across all convective events in terms of peaks in maximum updraft velocity or updraft volume with the peak total lightning flash rate. One reason for this type of performance may be due to the scale in which this type of subjective analysis is performed.

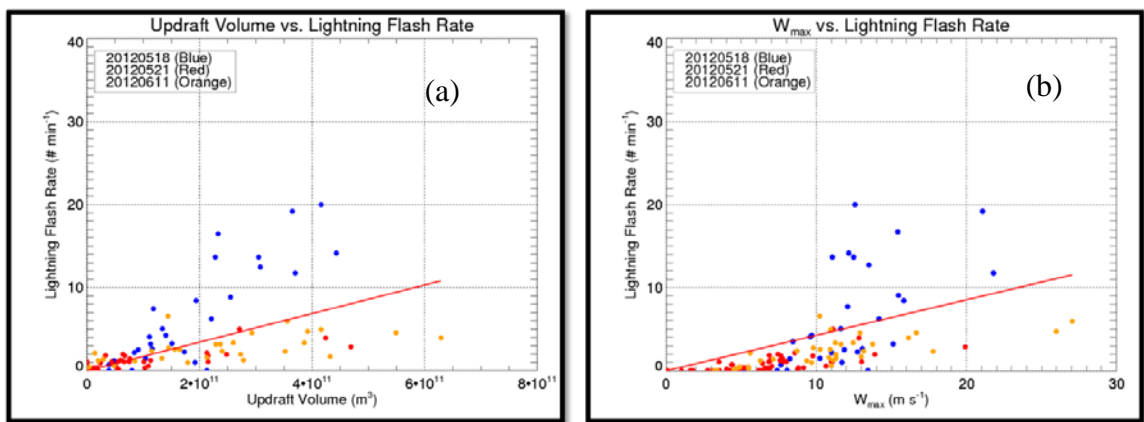


Figure 4.49. A scatterplot updraft volume greater than 5 m s^{-1} within the $-10 \text{ }^{\circ}\text{C}$ and $-40 \text{ }^{\circ}\text{C}$ layer for all DC3 AL cases excluding 14 June 2012 versus the total lightning flash rate is displayed in panel (a), while a scatterplot of the maximum updraft velocity within the $-10 \text{ }^{\circ}\text{C}$ and $-40 \text{ }^{\circ}\text{C}$ layer for all DC3 AL cases excluding 14 June 2012 versus the total lightning flash rate is displayed in panel (b). In each figure, the data points are color coded by date. Solid blue circles correspond to data points of complex A1 (18 May 2012), solid red circles correspond to complex B1 and B2 (21 May 2012), and solid orange circles correspond to complex C1 (11 June 2012). The solid red line represents the best fit line.

For example, the 18 May 2012 event (A1) had a much smaller areal extent in terms of 30 dBZ echo when compared to that of the 21 June 2012 event (C1). While C1 was larger in its areal coverage of updraft $> 5 \text{ m s}^{-1}$, it failed to produce more lightning than that of A1. The scatterplot from Fig. 4.49a explicitly shows this difference. From this plot, this bifurcation in the total lightning flash rate and updraft volume between different events is apparent. Convective complex C1 (orange dot) has the largest updraft volume, but fails to produce a peak total lightning flash rate of greater than $10 \text{ flashes min}^{-1}$, while complex A1 (blue dots) is nearly a factor of two smaller than that of C1. Figure 4.49b also shows this bifurcation in the total lightning flash rate and maximum updraft velocity within the mixed phase region. Consistent with studies conducted by Kuhlman et al. (2006) and Deierling and Petersen (2008), the maximum updraft velocity was the worst performer in terms of the Pearson product moment correlation and had some of the highest error associated with its linear least squares best fit line. Additional discussion on this will be provided in the forthcoming sections.

Key to the idea of NIC is the presence of graupel, supercooled particles and ice crystals. As shown explicitly in the radar coverage, it is apparent that the appearance of graupel often signified the onset of lightning. Specifically, numerous observations (Carey and Rutledge 1996; Wiens et al. 2005; Kuhlman et al. 2006) have explicitly noted that the graupel echo volume performed well consistently. For this data set, the graupel echo volume within the $-10 \text{ }^{\circ}\text{C}$ to $-40 \text{ }^{\circ}\text{C}$ layer was examined and the statistical results are presented herein. Unlike the peak values of the updraft volume $> 5 \text{ m s}^{-1}$, the maximum graupel echo volume appears to capture the peaks in instability and the total lightning flash rate as seen in Table 4.6 and Fig. 4.50.

Table 4.6. Comparison of thermodynamic, electrical, and microphysical properties during DC3 AL. Estimates of vertical motion is not available from the 14 June 2012 case.

DC3 AL Case Event	SBCAPE (J kg^{-1})	DCAPE (J kg^{-1})	Peak Total Lightning Flash Rate (flash min^{-1})	Total Lightning Flash Count (CG)	Peak CG Lightning Flash Rate (flash min^{-1})	Maximum Graupel echo volume (m^3)
A1	1270	950	20.0	778 (9)	.25	3.02×10^{11}
B1	785	702	1.1	6 (3)	.36	1.5×10^{10}
B2	785	702	5.0	111 (19)	1.1	1.0×10^{11}
C1	1216	776	6.57	396 (61)	1.1	1.08×10^{11}
D1	2368	1230	31.3	1657(112)	3.2	4.15×10^{11}

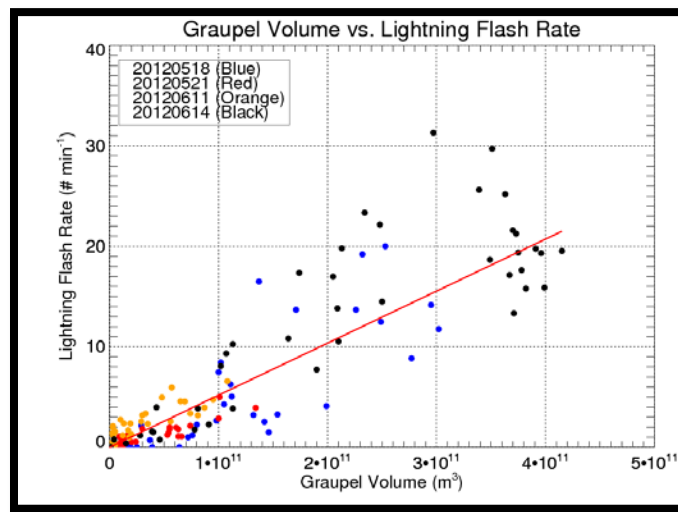


Figure 4.50. Scatterplot of graupel echo volume within the $-10\text{ }^{\circ}\text{C}$ and $-40\text{ }^{\circ}\text{C}$ layer for all DC3 AL cases. The filled circles are radar derived graupel volume within the $-10\text{ }^{\circ}\text{C}$ to $-40\text{ }^{\circ}\text{C}$ layer and corresponding total lightning flash rate. Solid blue circles correspond to data points of complex A1, solid red circles correspond to complex B1 and B2, solid orange circles correspond to complex C1, and solid black circles correspond to complex D1. The solid red line represents the best fit line.

From a physical standpoint, this result is intuitive as it is expected that a stronger updraft would be able to support the lofting of liquid hydrometeors into the mixed phase region, suspend them, and ultimately support coalescence freezing and riming. Williams (2001) alluded to this result in their study of DMC as well. Fig. 4.50 reveals the radar derived graupel echo volume within the $-10\text{ }^{\circ}\text{C}$ to $-40\text{ }^{\circ}\text{C}$ layer from each radar volume plotted against the total lightning flash rate observed. From the plot, it is apparent that

there is a clear distinction between the varying flash rate events across DC3 AL. The higher flash rate events (A1 and D1) corresponded to higher graupel echo volume, while the lower flash rate events (B1, B2 and C1) typically were associated with smaller graupel echo volumes. With such a seemingly favorable correlation, the graupel mass was examined due to the notion that larger graupel particles tended to charge more efficiently than smaller ones (Takahashi 1978). Fig. 4.51 reveals the radar derived graupel mass within the -10 °C to -40 °C layer.

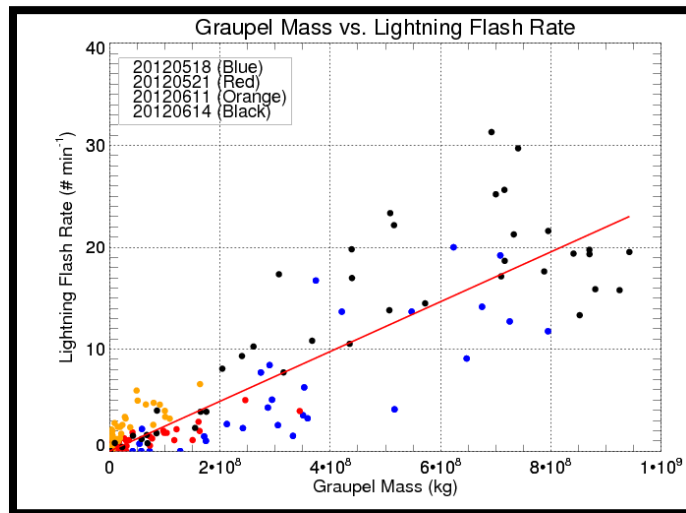


Figure 4.51. Scatterplot of graupel mass within the -10 °C and -40 °C layer for all DC3 AL cases. The filled circles are radar derived graupel masses within the -10 °C to -40 °C layer and corresponding total lightning flash rate. Solid blue circles correspond to data points of complex A1, solid red circles correspond to complex B1 and B2, solid orange circles correspond to complex C1, and solid black circles correspond to complex D1. The solid red line represents the best fit line.

Fig. 4.51 reveals that a similar distinction between relatively high and low flash rate events exists on the basis of the graupel mass. As expected from NIC, A1 and D1 had the higher order of magnitude graupel mass and thus higher total lightning flash rates. Interestingly enough, A1 and D1 both exhibited the TBSS hail signature. While hail is not necessarily a requisite for the generation of lightning, the presence of a large number

of graupel particles could ultimately lead to the development of large hail aloft. This large hail aloft appears to have manifested itself in the three body scatter spike hail signature. These signatures were absent in the weaker convection. An order of magnitude smaller graupel mass within the -10 °C to -40 °C layer was generally observed with the convection that had smaller total lightning flash rates.

In order to quantify these relationships, the use of the Pearson Product moment correlation was used to gauge the degree of correlation between a radar observable and the total lightning flash rate. Ranges for the Pearson Product moment correlation tests are between -1 and 1. A perfect positive linear relationship between two variables would result in a Pearson product moment correlation of 1. For this study, zero-lag Pearson correlation tests were conducted on the graupel echo volume, graupel mass, updraft volume $> 5 \text{ m s}^{-1}$, maximum updraft velocity, 30 dBZ echo volume and total lightning flash rate. The results are presented in Table 4.7. Based on information from the scatter plots in Figs 4.49-4.51., the method of linear least squares was employed to determine a best fit line. The root mean square error and mean errors associated with the expression determined from the method of linear least squares between the radar inferred quantity (e.g. graupel echo volume, graupel mass, etc.) and the total lightning flash rate are summarized in Table 4.7.

Table 4.7. Results from statistical analysis performed on radar observables during DC3 AL.

Radar Observable	Sample Size (# of points)	Pearson Correlation Coefficient (ρ)	Best Fit Line	Root Mean Square Error	Mean Square Error
Graupel Echo Volume	200	0.91	$Y = 5.6 \times 10^{-11} \times X$	2.7	7.29
Graupel Mass	200	0.90	$y = 2.43 \times 10^{-8} \times X$	3.05	9.3
30 dBZ Echo Volume	200	0.83	$Y = 1.73 \times 10^{-11} \times X$	4.14	17.1
Updraft Volume $> 5 \text{ m s}^{-1}$	136	0.65	$Y = 1.72 \times 10^{-11} \times X$	2.8	8.13
Maximum Updraft Velocity	136	0.59	$Y = 0.42 \times X$	3.3	11

From Table 4.7, it is apparent that graupel echo volume within the -10 °C to -40 °C layer performed the best across all event case days. The relatively higher correlation and smaller error suggests that it is a more robust parameter in terms of trending with the total lightning flash rate. Similarly, the graupel mass tended to trend well with the total lightning flash rate with a correlation of around 0.90. While this correlation is similar to that of the graupel echo volume, the slight increase in the RMSE and MSE may suggest that the graupel mass is slightly less reliable when compared to the graupel echo volume. This suggests that graupel mass may not be as useful as graupel echo volume for determining the total lightning flash rate in a numerical cloud model. One possible explanation for the slightly higher RMSE and MSE is the sensitivity of the Z_h - M_{ice} relationship to the varying particle size distribution. In these Z_h - M_{ice} relationships, numerous assumptions are made about the number concentration, ice density, and density of air so the error in calculating M_{ice} may diminish its utility for diagnosing lightning flash rates. While, the graupel echo volume performance well across all of DC3 AL, a closer inspection as to whether or not the polarimetric data (NCAR PID) offered any advantage over a legacy method (e.g. 30 dBZ echo volume) is required.

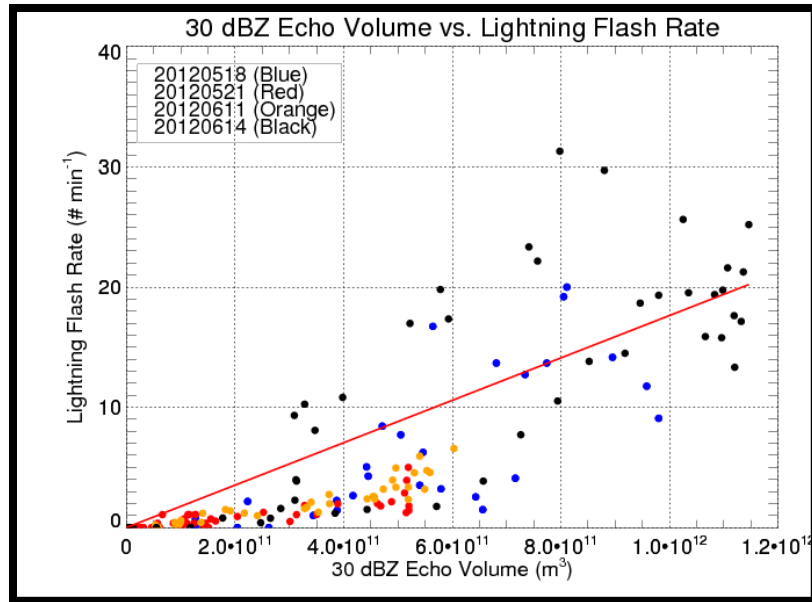


Figure 4.52. Scatterplot of 30 dBZ echo volume within the -10 °C and -40 °C layer for all DC3 AL cases. The filled circles are radar derived 30 dBZ echo volume within the -10 °C to -40 °C layer and corresponding total lightning flash rate. Solid blue circles correspond to data points of complex A1, solid red circles correspond to complex B1 and B2, solid orange circles correspond to complex C1, and solid black circles correspond to complex D1. The solid red line represents the best fit line.

From Table 4.7, it is apparent that the 30 dBZ echo volume in the -10 °C to -40 °C layer does not correlate as well ($\rho = 0.83$) with the total lightning flash rate as well as the graupel echo volume and as a result, it is apparent that there is some utility in the polarimetric radar data inferring relevant microphysical information. Moreover, the RMSE (4.14) and MSE (17.1) are larger. There are numerous possibilities as to why the 30 dBZ echo volume does not perform as well as the NCAR PID graupel echo volume. The 30 dBZ echo volume is a rigid threshold that may not account for the higher number concentration of smaller graupel particles. Also, the 30 dBZ echo volume may include hydrometeors that are not necessarily conducive to the NIC. These hydrometeors could range from liquid droplets (not supercooled) to large hail. Furthermore, in some instances

it may be insufficient to use a Z_h threshold to discriminate between rain drops and graupel.

Table 4.8. Additional storm parameters (30 dBZ echo volume and updraft volume $> 3 \text{ m s}^{-1}$) along with parameters from Table 4.7 correlation with the total lightning flash rate for DMC events across examined across DC3 AL.

Radar Observable	Sample Size (# of points)	Pearson Correlation Coefficient (ρ)
Graupel echo volume	200	0.91
30 dBZ Echo Volume	200	0.83
Graupel Mass	200	0.90
Updraft Volume $> 3 \text{ m s}^{-1}$	136	0.51
Updraft Volume $> 5 \text{ m s}^{-1}$	136	0.65
Maximum Updraft Velocity	136	0.59

Finally, the updraft volume greater than 5 m s^{-1} and the maximum updraft velocities performed the poorest in terms of trending well with the total lightning flash rate. For the updraft volume calculations, it is intuitive to think that for storms across DC3 AL, perhaps a smaller factor of the updraft volume is more appropriate. In general, the frequency in which these weaker storms exceed maximum updraft velocities of over 5 m s^{-1} may be intermittent at best. Interestingly, these storms still produced lightning. For these relatively lower flash rate storms, however, it may be appropriate to use a lower threshold for the updraft volume. The information in Table 4.8 would suggest that the updraft volume greater than 3 m s^{-1} is a poorer metric to use when compared to the updraft volume greater than 5 m s^{-1} on the entire dataset. Table 4.9 shows that on a case-by-case basis, the performance is slightly better across the lower peak flash rate events.

Table 4.9. Comparison between updraft volume $> 3 \text{ m s}^{-1}$ and updraft volume $> 5 \text{ m s}^{-1}$ versus total flash rate for all case events during DC3 AL.

Case Event	Updraft Volume $> 3 \text{ m s}^{-1}$	Updraft Volume $> 5 \text{ m s}^{-1}$	Peak Total Lightning Flash Rate (flash min^{-1})
	& Total Lightning Flash Rate (ρ)	& Total Lightning Flash Rate (ρ)	
A1	0.73	0.85	20.0
B1	0.87	0.81	1.1
B2	0.81	0.61	5.0
C1	0.72	0.69	6.57
D1	--	--	31.3

From Table 4.9, it is apparent that the smaller factor of the updraft volume tended to perform better for the two lower flash rate events across DC3 AL. While the former is true, the decline in the correlation when the updraft volume greater than 3 m s^{-1} is tested against the entire dataset suggests that this is not a particularly robust relationship. Moreover, additional testing is necessary in order to determine whether or not the updraft volume greater than 3 m s^{-1} will outperform the updraft volume greater than 5 m s^{-1} in terms of correlation with the total lightning flash rate. Nevertheless, it is evident that these lower flash rate events necessitate a lower threshold in terms of upward vertical motion due to their intrinsically weak nature. Finally, the poor performance of maximum updraft velocity with the total lightning flash rate is somewhat consistent with previous literature. Kuhlman et al. (2006) and Deierling and Petersen (2008), in numerical simulations and observations respectively, note that the maximum updraft velocity performs the worst in terms of correlation with the total lightning flash rate. Interestingly enough, Barthe et al. (2010) found that the maximum updraft velocity trended the best in their numerical simulations. The results presented here would certainly support findings of Kuhlman et al. (2006) and Dierling and Peterson (2008). The different results from these studies would suggest a high degree of variability (including error) when potentially

attempting to develop a total lightning flash rate and maximum updraft velocity relationship.

5.2 Discussion on errors associated with DC3 AL Dataset

This subsection will attempt to discuss the error associated with the DC3 AL dataset analyzed here. The most likely cause of error associated with this dataset is likely measurement error from both radar and lightning platforms. Discussed in section 3.5, Cummins et al. (1998) reported that median spatial errors of the NLDN were around 500 meters. As discussed in section 3.9, spatial errors for VHF radiation sources are on the order of 100s of meters. While these spatial errors are on the order of 100s of meters for both the NLDN and LMA, there was likely negligible impact on the dataset. This is due in part to the lightning information being used to primarily examine where likely NIC and subsequent breakdown occurred and various polarimetric radar signatures.

The calculations associated with radar observations vary depending on the variable (e.g. graupel echo volume, graupel mass, updraft volume, etc.). Reflectivity based observations are dependent on the diameter of the particle to the sixth power (D^6). This may result in the dominance of the radar sample volume by only a few large particles. For example, one to two large graupel particles would dominate the radar volume that consists of a larger quantity of ice crystals. The aforementioned scenario would likely lead to the NCAR PID diagnosing a region of graupel, even though the most common hydrometeor may be the ice crystals. This likely resulted in an overestimate of the graupel echo volume and graupel mass.

Finally, errors associated with the estimate of vertical motion from the multi-Doppler wind synthesis likely occurred. As discussed previously, the variational scheme

was invoked to determine vertical motion. This method integrates the mass continuity equation over a majority of the echo from storm top to some given level. The lowest portion of the echo is also integrated upward from the surface ($z = 0$ km) to a given level. Despite the improvement in estimation of the vertical motion as reported by Gao et al. (1999), errors are still present. These integration errors along with coarse, 1-km, grid resolution likely result in an underestimate of vertical motion. This is especially true for the 18 May 2012 (A1) case day in which the close proximity of the convective complex to ARMOR resulted in the inability to sample the entire echo. With the entire echo not being sampled, the assumption that the boundary condition at the echo top ($w=0$) is invalid. While convection on other case days (21 May and 11 June) was sampled completely, there is likely still some error associated with the upper boundary condition. Despite the echoes on these days (21 May and 11 June) being observed through the storm top, it is difficult to verify that even in clear air (e.g. 0 dBZ) above the echo that $w = 0$. With the variational method being invoked, a small layer near the surface is integrated upward and then averaged with the downward integration. Similar to the upper boundary conditions, this lower boundary condition becomes ambiguous due to the sampling limitation of the radar, especially for cases at relatively larger distances from ARMOR and KHTX.

CHAPTER SIX

SUMMARY AND CONCLUSIONS

6.1 Summary

An overview of the environmental controls on convective morphology has been examined for DMC across northern Alabama during the DC3 field campaign. Four case days consisting of a total of five convective events were examined in this study. Vertical profiles of temperature and humidity from radiosonde observations were used to denote important temperature levels in which hydrometeors relevant to the NIC mechanism develop and reside. These profiles lend themselves useful to calculations of CAPE, which provided at least a qualitative measure of expected updraft intensity. Moreover, an examination of observed wind speeds with height aided in the explanation of convective morphology.

The primary goal of this DC3 study was to utilize multi-Doppler and dual-polarization radar inferred observations and analysis products to investigate the microphysical and kinematic control of the total lightning flash rate. Observations of lightning were possible with NALMA and the NLDN platforms. The use of radar and environmental thermodynamic information was ingested into a fuzzy logic based hydrometeor identification algorithm (NCAR PID) and was also used in subjective interrogation of both radar CAPPI's and cross-sections. With information from the NCAR PID output, calculations of both bulk and mass specific hydrometeor quantities

were performed. Similarly, information obtained from multi-Doppler wind synthesis allowed for a quantitative measure of vertical motion within the DMC.

Finally, statistically derived empirical relationships have been developed between radar inferred kinematic and microphysical quantities and the total lightning flash rate as inferred by NALMA. The relationships developed here, in combination with similar studies over the other DC3 regions (e.g. Oklahoma, Colorado), can be used to create a more accurate and generalized lightning parameterization in numerical cloud models that lack an explicit cloud electrification module. The lightning parameterization can then be used in DC3 related atmospheric chemistry modeling studies of LNO_x production and perhaps also in an operational setting requiring lightning forecasts for lightning safety or convective situational awareness applications.

6.2 Conclusions

From an environmental standpoint, RAOBs during DC3 case days revealed that synoptic forcing was generally weak. As a result, deep layer shear was very small often less than 10 m s^{-1} . RAOBs indicated that surface based CAPE values across the DC3 case days were all fairly similar to each other and ranged from just below 1000 J kg^{-1} to values in excess of 2300 J kg^{-1} . Given this range of instability and the low magnitudes of the deep layer shear, predominately multicellular convection was anticipated based on field observations and numerical simulations (Rotunno et al. 1988; Weisman and Klemp 1984; Bluestein 1993). In this study, it was determined that the days characterized as having higher values of SBCAPE tended to facilitate higher flash rate storms. It was argued, based on elementary parcel theory, that the theoretical relationship between CAPE and

the maximum allowable updraft velocity was the primary reason for this correspondence. Convective episodes that had a higher peak in the updraft velocity tended to also have a higher peak in the total lightning flash rate when compared to the weaker updraft, events. Inferences from the observations of CAPE from environmental soundings and peak total lightning flash rate have been made from experiments in the past and the observations for this study appear to be consistent with prior studies (Rutledge et al. 1992; Williams 1992; Zipser and Lutz 1994; Petersen et al. 1996). Through the use of thermodynamic diagrams, it was often observed that low-level lapse (0-3 km) rates were generally on the order of -7.0 C km^{-1} . These relatively steep lapse rates often resulted in the generation of a substantial amount of DCAPE. With large amounts of DCAPE, effective convective outflows were generated. These convective outflows, in many instances during DC3 AL allowed for the development of additional convective cells. This is thought to be important to the overall maintenance of the multicell convective complex at least initially as new convective cells develop along thunderstorm outflow. Once low-level convergence proved to be insufficient, the convective complex typically decayed rapidly.

The Z_{dr} column signature as observed in nearly every case day analyzed for DC3 AL was shown to be a manifestation of important microphysical and to an extent kinematic processes of DMC. The Z_{dr} column was shown to denote a region in which large oblate raindrops are lofted by a sufficiently strong updraft (Smith et al. 1999). This point illustrates how the Z_{dr} column can be used to make kinematic inferences. It was argued that a Z_{dr} column that extended higher into the mixed phase region of the convective cloud often suggested that larger oblate particles (identified by NCAR PID based on Z_h and Z_{dr} thresholds), which have a larger terminal fall velocity, were being

transported upward by a stronger updraft (Kumjian et al. 2012). It was also shown that atop the Z_{dr} column, a depression in ρ_{hv} often existed (Kumjian et al. 2012). The lowered ρ_{hv} values represented a diversity of hydrometeors and perhaps the location of particles relevant for NIC. Similarly, a sharp decrease in the Z_{dr} atop the Z_{dr} column in the mixed phase region represented a transition from oblate (likely liquid), to more spherical particles (likely ice). As in Bruning et al. (2007), low-level flash initiations often occurred in this region, particularly associated with early lightning in the developing to mature stage of thunderstorms. An increase in both the graupel echo volume and graupel mass often accompanied or lagged behind this signature by a radar volume or two (5-10 minutes). The hail flare echo or three body scatter spike (TBSS) was also noted in two of the highest peak flash rate events (A1, D1). While hail is not a requirement for NIC, the presence of this signature in ordinary multicellular convection may have a microphysical and kinematic significance. From a microphysical standpoint, it has been shown that graupel is a key component of hail production. The appearance of large hail aloft (TBSS) may signify a large production of larger graupel particles due to graupel's role in the hail formation process. The kinematic perspective of this argument stems from the notion of requiring a persistently strong updraft for the lofting and riming growth of graupel aloft to generate large hail.

In order to develop meaningful relationships between a radar observable and total lightning flash rate, a more quantitative approach was necessary (Deierling and Petersen 2008; Barthe et al. 2010). Observations from Doppler polarimetric radars revealed that the graupel echo volume and graupel mass trended well with the total lightning flash rate. To quantify this behavioral trend, Pearson product moment correlation tests were

performed. These tests revealed that the best and most consistent performer was the graupel echo volume ($\rho = 0.91$). This is consistent with observations from Wiens et al. (2005), Kuhlman et al. (2006) and Carey and Rutledge (1996). Moreover, elementary linear regression analysis revealed that the graupel echo volume-total lightning flash rate relationship exhibited the least amount of root mean square error. The graupel echo volume was followed by the graupel mass ($\rho = 0.90$) and finally the updraft volume greater than 5 m s^{-1} ($\rho = 0.65$) and maximum updraft velocity ($\rho = 0.59$). The latter two parameters exhibited some of the higher root mean square and mean square error across the dataset. Based on these results, it can be determined that bulk hydrometeor (e.g. graupel echo volume) identification (and resultant calculations), outperform particle specific (graupel mass) computations slightly. Of most importance, however, is the relatively smaller amount of RMSE ($2.7 \text{ flashes min}^{-1}$) and MSE ($7.29 \text{ flashes}^2 \text{ min}^{-2}$) associated with the graupel echo volume-total lightning flash rate relationship when compared to the graupel mass-total lightning flash rate relationship. Also, in order to validate the notion that polarimetric radar variables offered additional useful information, the Pearson product moment correlation test was applied on the 30 dBZ echo volume ($\rho = 0.83$) across all data points (200) for the cases during DC3 AL. The RMSE ($4.5 \text{ flashes min}^{-1}$) and MSE ($17.1 \text{ flashes}^2 \text{ min}^{-2}$) were also higher with the 30 dBZ echo volume when compared to the NCAR PID graupel echo volume. Results from these tests increase the confidence that polarimetric radar may offer some added benefit in terms of identifying hydrometeors for the application of trends in total lightning. Based on previous studies praise of the updraft volume, it was somewhat surprising to see a relatively poorer Pearson product moment correlation for the DC3 AL DMC. As a result,

sensitivity tests were employed to determine the source of this discrepancy between results here and previous studies. It was determined that for lower flash rate events (< 10 flashes min^{-1}), a lower threshold for updraft volume may be more appropriate and the updraft volume greater than 3 m s^{-1} was the next logical threshold. The Pearson product moment correlation test between the updraft volume greater than 3 m s^{-1} and total lightning flash was applied to individual cases. For the lower flash rate events, a marked increase in correlation occurred for the lower flash rate events only. As a result, this parameter does not appear to be robust across all flash rate events. Finally, performance of the maximum updraft velocity and the total lightning flash rates had the worst correlation ($\rho = 0.59$) and some of the higher MSE ($11 \text{ flashes}^2 \text{ min}^{-2}$) and RMSE ($3.3 \text{ flashes min}^{-1}$)

APPENDIX A

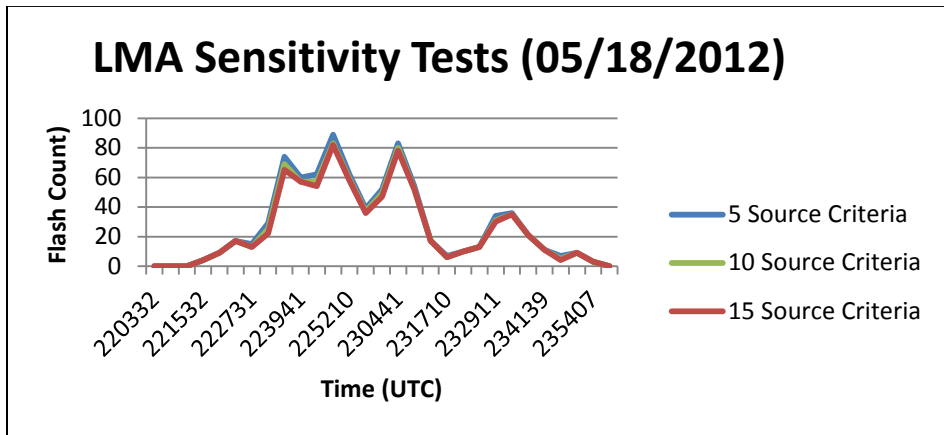


Figure A.1. This chart shows the sensitivity of VHF source criteria for a DMC event during DC3 across northern AL on 18 May 2012. This DMC event was roughly 20 km from the center of NALMA. VHF sources are clustered using the McCaul (2005) algorithm. The solid blue line represents a 5 source criteria, the solid green line represents a 10 source criteria, and the solid red line represents a 15 source criteria.

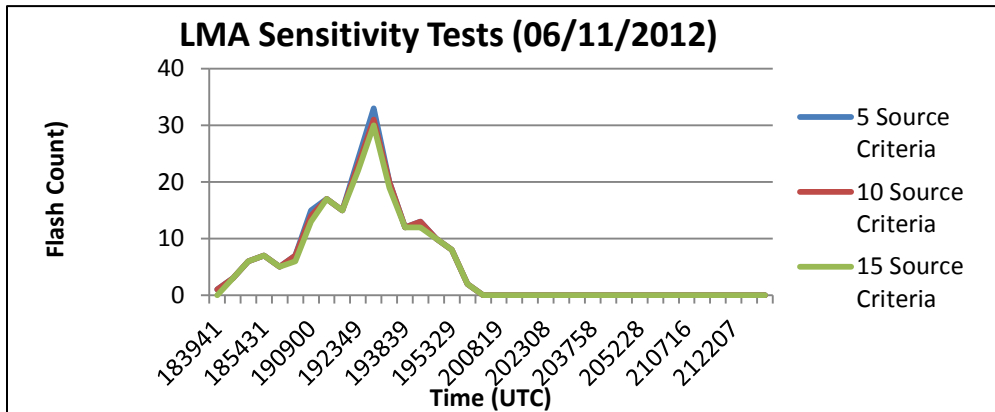


Figure A.2. This chart shows the sensitivity of VHF source criteria for a DMC event during DC3 across northern AL on 11 June 2012. This DMC event was roughly 80 km from the center of NALMA. VHF sources are clustered using the McCaul (2005) algorithm. The solid blue line represents a 5 source criteria, the solid red line represents a 10 source criteria, and the solid green line represents a 15 source criteria.

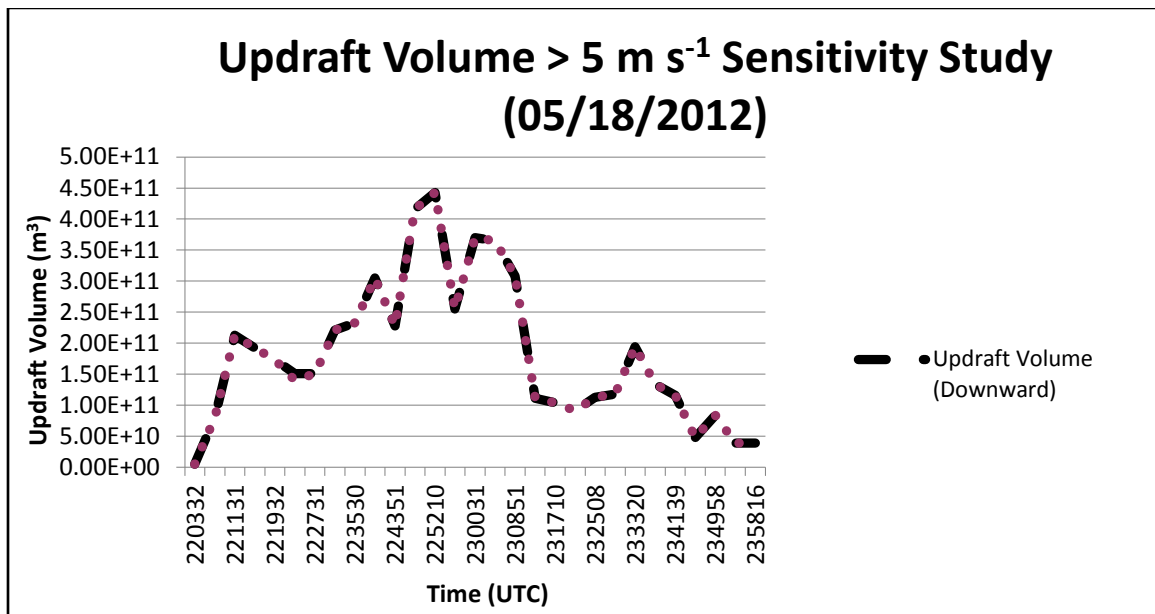


Figure A. 3. This chart shows the results from a sensitivity study that varies the direction of the integration of the anelastic mass continuity equation. Vertical motion is determined from this integration process. The sensitivity study is performed on data from the 18 May 2012 case day. The dashed black line represents the updraft volume > 5 m s⁻¹ in which the updraft velocity was computed using explicit downward integration of the anelastic mass continuity equation. The dotted light violet line represents the updraft volume > 5 m s⁻¹ in which the updraft velocity was computed using the variational method of integration of the anelastic mass continuity equation.

APPENDIX B

Table B.1. NWS Volume Coverage Patterns (VCP) of the WSR-88D

Volume Coverage Pattern (VCP)	Number of Tilts	Approximate Update Time (min)	Elevation Angles (°)
11 or 211	14	5	0.5, 1.5, 2.4, 3.4, 4.3, 5.3, 6.2, 7.5, 8.7, 10.0, 12.0, 14.0, 16.7, 19.0
12 or 212	14	4.5	0.5, 0.9, 1.3, 1.8, 2.4, 3.1, 4.0, 5.1, 6.4, 8.0, 10.0, 12.5, 15.6, 19.5
21 or 121 or 221	9	6	0.5, 1.5, 2.4, 3.4, 4.3, 6.0, 9.9, 14.6, 19.5
31 or 32	5	10	0.5, 1.5, 2.5, 3.5, 4.5

Table B.2. ARMOR and MAX scan pattern during DC3. The bolded information refers to the addition of a elevation angled during the 120° SV for MAX.

Scan Strategy	Number of Tilts	Elevation Angles (°)
360° Surveillance	23	0.7, 1.3, 1.9, 3.0, 4.1, 5.3, 6.4, 7.6, 8.7, 9.8, 11.0, 12.1, 13.2, 14.3, 15.5, 16.8, 17.6, 18.2, 19.7, 21.2, 23.0, 24.8, 26.8
120° Sector Volume	17 (18)	0.7, 1.3, 1.85, 2.99, 4.14, 5.28, 6.42, 7.56, 8.69, 9.83, 10.95, 12.08, 13.2, 14.32, 15.5, 16.77, 18.15, (19.64)
180° Sector Volume	21	0.7, 1.3, 1.85, 2.99, 4.14, 5.28, 6.42, 7.56, 8.69, 9.83, 10.95, 12.08, 13.2, 14.32, 15.5, 16.77, 18.15, 19.64, 21.24, 22.97, 24.83
RHI	--	Ranges from 0 to 45

Table B.3. NCAR PID Category Table

Category Value	Category Name
1	Cloud
2	Drizzle
3	Light Rain
4	Moderate Rain
5	Heavy Rain
6	Hail (Large)
7	Rain/Hail Mixture
8	Graupel/Small Hail
0	Graupel/Rain Mixture
10	Dry (Low Density) Snow
11	Wet (High Density) Snow
12	Ice Crystals
13	Irregular Ice Crystals
14	Supercooled Liquid Droplets
15	Insects
16	2 nd Trip Echo
17	Ground Clutter

Table B.4. Quality control flag, the flag description and ASCII code that is applied to RAOB data during the DC3 Experiment for all regions.

Quality Control Flag	Flag Description	ASCII Code
Good	No physical reason to question the parameter.	1.0
Questionable	The parameter seems to be questionable on a physical basis.	2.0
Bad	The parameter appears to be in error.	3.0
Estimated	The parameter was interpolated.	4.0
Missing	The parameter is missing.	9.0
Unchecked	The parameter is present but was not checked.	99.0

Table B.5. A summary of convective events across northern AL and southern TN during the DC3 field campaign is presented in this table. Bolded events (B2 and C1) denote aircraft and ground based observations were performed.

Cell Designation	Date	Time (UTC)	Distance to ARMOR (km)	Distance to center of NALMA (km)
A1	18 May 2012	2200-0100	15-20	25
B1	21 May 2012	1935-2037	60-65	35
B2	21 May 2012	1935-2127	60-65	50
C1	11 June 2012	1839-2131	90-95	85
D1	14 June 2012	1628-1933	65-70	65

REFERENCES

- Armijo, L., 1969: A Theory for the Determination of Wind and Precipitation Velocities with Doppler Radars. *J. Atmos. Sci.*, **26**, 570–573.
- Anderson, M.E, L.D. Carey, W.A. Petersen, K.R. Knupp, 2011: C-band Dual-polarimetric Radar Signatures of Hail. *Electronic J. of Operational Meteor.*, **12**, 1-30.
- Barthe, C., M.C. Barth, 2008: Evaluation of a new lightning-produced NO_x parameterization for cloud resolving models and its associated uncertainties. *Atmos. Chem. Phys.*, **8**, 4691-4710.
- Barthe, C., W. Deierling, M.C. Barth, 2010: Estimation of total lightning from various storm parameters: A cloud-resolving model study. *J. Geophys Res.*, **115**, doi: 10.1029/2010JD013305.
- Barth, M., W. Brune, C. Cantrell, S. Rutledge, 2012: Overview of the Deep Convective Clouds and Chemistry (DC3) Field Campaign presented at 2012 Fall Meeting, *Amer. Geophys. Union*, San Francisco, Calif., 3-7 Dec.
- Bluestein, H.B., 1993: *Synoptic-Dynamic Meteorology in Midlatitudes Vol II*. Oxford University Press, 456-462 pp.
- Boccippio, D. J., K.L. Cummins, H. J. Christian, S. J. Goodman, 2001: Combined Satellite- and Surface-Based Estimation of the Intracloud–Cloud-to-Ground Lightning Ratio over the Continental United States. *Mon. Wea. Rev.*, **129**, 108–122.
- Biagi, C. J., K. L. Cummins, K. E. Kehoe, P. Krider, 2007: National Lightning Detection Network (NLDN) performance in southern Arizona, Texas, and Oklahoma in 2003-2004. *J. Geophys Res.* **112**, DOI: 10.1029/2006JD007341.
- Bringi, V.N, V. Chandrasekar, 2001: *Polarimetric Doppler Weather Radar Principles and Applications*. Cambridge University Press, 636 pp.
- _____. T.D. Keenan, V. Chandrasekar, 2001: Correcting C-Band radar Reflectivity and Differential Reflectivity Data for Rain Attenuation: A Self-Consistent Method With Constraints. *IEEE Transc. on Geo. and Rem. Sens*, **39**, 1906-1915.
- Bruning, E. C., W. D. Rust, T. J. Schuur, D. R. MacGorman, P. R. Krehbiel, W. Rison, 2007: Electrical and Polarimetric Radar Observations of a Multicell Storm in TEXAS. *Mon. Wea. Rev.*, **135**, 2525–2544.

- Byers, H.R., R.R. Braham Jr., 1949: Thunderstorm structure and circulation. *J. Meteor.*, **5**, 71-86.
- Carey, L. D., S.A. Rutledge, 1996: A multiparameter radar case study of the microphysical and kinematic evolution of a lightning producing storm, *J. Meteorol. Atmos. Phys.*, **59**, 33–64.
- _____, 2000: The Relationship between Precipitation and Lightning in Tropical Island Convection: A C-Band Polarimetric Radar Study. *Mon. Wea. Rev.*, **128**, 2687–2710.
- _____, M.J. Murphy, T.L. McCormic, N.W. S. Demetriades, 2005: Lightning location relative to storm structure in a leading-line, trailing-stratiform mesoscale convective system. *J. Geophys. Res.*, **110**, D03105.
- Coleman, L. M., M. Stolzenburg, T. C. Marshall, M. Stanley, 2008: Horizontal lightning propagation, preliminary breakdown, and electric potential in New Mexico thunderstorms, *J. Geophys. Res.*, **113**, D09208.
- Cooray, V, 1997: Energy Dissipation in Lightning Flashes: *J. Geophys. Res.*, **102**, 21401-21410.
- _____, V. Rahman, M. Rakov, 2009: On the NO_x production by laboratory electrical discharges and lightning. *J. Sol. Atmos. Terr. Phys.* **71**, 1877-1889.
- Cressman, G.P., 1959: An Operational Objective Analysis System. *Mon. Wea. Rev.*, **87**, 367-374.
- Cummins, K.L., M.J. Murphy, E.A. Bardo, W.L. Hiscox, R.B. Pyle, A.eE. Pifer, 1998: A combined TOA/MDF technology upgrade of the U.S. National Lightning Detection Network. *J. Geophys. Res.*, **103**, 9035-9044.
- _____, J.A. Cramer, C.J. Biaji, E.P. Krider, J. Jerauld, M. A. Uman, V.A. Rakov, 2006: The U.S. National Lightning Detection Network: Post-upgrade status. Preprints, 2nd Conference on Meterological Applications of Lightning Data, January 29-February 2, Atlanta, GA, American Meterological Society, 9 pp.
- _____, M.J. Murphy, 2009: An Overview of Lightning Locating Systems: History, Techniques, and Uses, With an In-depth Look at the U.S. NLDN, *IEEE Transactions on Electromagnetic Compatibility*, Vol. **51**, 499-518.
- Davies-Jones, R. P., 1979: Dual-Doppler Radar Coverage Area as a Function of Measurement Accuracy and Spatial Resolution. *J. Appl. Meteor.*, **18**, 1229–1233.

- Deierling W., W.A. Petersen, J. Lantham, S. Ellis., H.J. Christian Jr., 2008: The relationship between lightning activity and ice fluxes in thunderstorms, *J. Geophys Res.*, **113**, doi:10.1029/2007JD009700.
- _____, W.A. Petersen, 2008: Total lightning activity as an indicator of updraft characteristics. *J. Geophys Res.*, **113**, doi:10.1029/2007JD009598.
- Doswell, C.A. III, 1985: The Operational Meteorology of Convective Weather. Vol. II: Storm-scale Analysis. NOAA Tech. Memo. ERL ESG-15, National Severe Storms Lab., 1313 Halley Circle, Norman, OK, 73069.
- Dye J.E., B.A. Ridley, W. Skamarock, M. Barth, M. Venticinque, E. Defer, P. Blanchet, C. Thery, P. Laroche, K. Baumann, G. Hubler, DD. Parrish, T. Ryerson, M. Trainer, G. Frost, J.S. Holloway, T. Matejka, D. Bartels, F.C. Fehsenfeld, A. Tuck, S.A. Rutledge, T. Lang, J.Stith, R. Zerr, 2000: An overview of the Stratospheric-Tropospheric Experiment Radiation, Aerosols, and ozone (STERA0)-Deep Convective experiment with results for the July 10, 1996 storm. *J. Geophys. Res.*, **105**, 10023-10045.
- Hall, M.P., J.W. Goddard, S.M. Cherry, 1984: Identification of hydrometeors and other targets by dual-polarization radar, *Radio Sci.*, **19**, 132-140.
- Heymsfield, A. J., A. G. Palmer, 1986: Relations for deriving thunderstorm anvil mass of CCOPE storm water budget estimates, *J. Clim. Appl. Meteorol.*, **25**, 691– 702.
- Heymsfield, A.J., K.M Miller, 1988: Water vapor and ice mass transported into the anvils of CCOPE thunderstorms Comparison with storm influx rainout. *J. Atmos. Sci.*, **45**, 3501-3514.
- Hill, R.D., R.G. Rinker, H.D. Wilson, 1980: Atmospheric Nitrogen Fixation by Lightning. *J. Atmos. Sci.*, **37**, 179-192.
- Hubbert, J., V. N. Bringi, 1995: An Iterative Filtering Technique for the Analysis of Copolar Differential Phase and Dual-Frequency Radar Measurements. *J. Atmos. Oceanic Technol.*, **12**, 643–648.
- Elster, J., H., Geitel, 1888: A method for determining the electric nature of atmospheric precipitation. *Meteor. Z.*, **5**, 95-100.
- Gallardo, L., V. Cooray, 1996: Could cloud-to-cloud discharges be as effective as cloud-to-ground discharges in producing NO_x? *Tellus*, **48B**, 641-651.
- Gao, J., M. Xue., A. Shapiro, K. K. Droegemeier, 1999: A Variational Method for the Analysis of Three-Dimensional Wind Fields from Two Doppler Radars. *Mon. Wea. Rev.*, **127**, 2128–2142.

- Gatlin, P. N., S. J. Goodman, 2010: A Total Lightning Trending Algorithm to Identify Severe Thunderstorms. *J. Atmos. Oceanic Technol.*, **27**, 3–22.
- Golestani, Y., V. Chandrasekar, V.N. Bringi, 1989: Intercomparison of multiparameter radar measurements. *Proc. 24th Conf. on Radar Meteorology*, Tallahassee, FL, Amer. Meteor. Soc., 309-314.
- Goodman S.J, R. Blakeslee, H. Christian, W. Koshak, J. Bailey, J. Hall, E. McCaul, D. Buechler, C. Darden, J. Burks, T. Bradshaw, P. Gatlin, 2005: The North Alabama Lightning Mapping Array: Recent severe storm observations and future prospects. *Atmos. Res.*, **76**, 423-437.
- Gunn, R., G. D. Kinzer, 1949: The terminal velocity of fall for water droplets in stagnant air. *J. Meteor.*, **6**, 243–248.
- Koshak, W.J., R.J. Solakiewicz, R. J. Blakeslee, S. J. Goodman, H. J. Christian, J. M. Hall, J. C. Bailey, E. P. Krider, M. G. Bateman, D. J. Boccipio, D. M. Mach. E. W. McCaul, M. F. Steward, D. E. Buechler, W. A. Petersen, D. J. Cecil, 2004: North Alabama Lightning Mapping Array (LMA): VHF source retrieval algorithm and error analyses, *J. Atmos. Oceanic Technol.*, **21**, 543-558.
- _____, H. Peterson, A. Biazar, M. Khan, L. Wang, 2013: The NASA Lightning Nitrogen Oxides Model (LNOM): Application to air quality modeling. *Atmos. Res.* <http://dx.doi.org/10.1016/j.atmosres.2012.12.015>
- Kuhlman, K. M., C. L. Ziegler, E. R. Mansell, D. R. MacGorman, J. M. Straka, 2006: Numerically simulated electrification and lightning of the 29 June 2000 steps supercell storm. *Mon. Wea. Rev.*, **134**, 2734–2757.
- Krehbiel, P. R., R. Thomas, W. Rison, 1998: Lightning Mapping observations during MearPS in central Oklahoma, *Eos, Trans. AGU* , **79**.
- Kumjian, M. R., S. M. Ganson, A. V. Ryzhkov, 2012: Freezing of Raindrops in Deep Convective Updrafts: A Microphysical and Polarimetric Model. *J. Atmos. Sci.*, **69**, 3471–3490.
- Lamarque, J.-F., G.P. Brasseur, P.G. Hess, J.-F. Mueller, 1996: Three-dimensional study of the relative contributions of the different nitrogen sources in the troposphere. *J. Geophys. Res.*, **95**, 9971-9981.
- Lang, T.J, S.A. Rutledge, 2002: Relationships between Convective Storm Kinematics, Precipitation, and Lightning. *Mon. Wea. Rev.*, **130**, 2492-2506.
- Lemon, L. R., 1998: The Radar “Three-Body Scatter Spike”: An Operational Large-Hail Signature. *Wea. Forecasting*, **13**, 327–340.

- Loehrer, Scot M., T. A. Edmands, J. A. Moore, 1996: TOGA COARE Upper-Air Sounding Data Archive: Development and Quality Control Procedures. *Bull. Amer. Meteor. Soc.*, **77**, 2651–2671.
- MacGorman, D.R., W.D. Rust, 1998: Introduction to the Electrical Nature of Thunderstorms. *The Electrical Nature of Storms*, J. Helsdon, J. Latham, T. Marshall, B. Smull, M. Stolzenburg, and C. Ziegler. Oxford University Press, 49-61 pp.
- _____, J. R. Apostolakopoulos, N. R. Lund, N. W. S. Demetriades, M. J. Murphy, P. R. Krehbiel, 2011: The Timing of Cloud-to-Ground Lightning Relative to Total Lightning Activity. *Mon. Wea. Rev.*, **139**, 3871–3886
- Markowski, P., Y. Richardson, 2010: Organization of Isolated Convection. *Mesoscale Meteorology in Midlatitudes*, P. Inness and W. Beasley, Wiley-Blackwell, 201-244 pp.
- McCaul Jr., E.W., J.C. Bailey, J. Hall, S.J. Goodman, R.J. Blakeslee, D.E. Buechler., 2005: A Flash Clustering Algorithm for North Alabama Lightning Mapping Array data. *Conf. on Meteor. App. Of Lightning Data Preprints.*, San Diego, CA. Amer. Meteor. Soc.
- _____, S. J. Goodman, K. M. LaCasse, D. J. Cecil, 2009: Forecasting Lightning Threat Using Cloud-Resolving Model Simulations. *Wea. Forecasting*, **24**, 709–729.
- Miller, L. J., T. Frederick 1998: Earth Observation Laboratory's Radar Data Analysis Tools, <https://wiki.ucar.edu/display/raygridding/home>
- Mullendore, G.L., D.R. Durran, J.R. Houlston, 2005: Cross-tropopause tracer transport in midlatitude convection. *J. Geophys Res.*, **110**, doi: 10.1029/2004JD005059.
- Murphy. M.J., 2006: When Flash Algorithms Go Bad. *19th International Lightning Detection Conf.*, Tucson, AZ. Vaisala International Lightning Detection Conf.
- Oye, R., C. Mueller, S. Smith, 1995: Software for radar translation, visualization, editing and interpolation. *27th Conf. on Radar Meteorology*, Preprints., Vail, Colorado, Amer. Meteor. Soc.
- Petersen, W. A., S. A. Rutledge, R. E. Orville, 1996: Cloud-to-ground lightning observations of TOGA COARE: Selected results and lightning location algorithm, *Mon. Wea. Rev.*, **124**, 602-620.
- _____, 1997: Multi-scale process studies in the tropics: Results from lightning observations. Ph.D. dissertation, Colorado State University, 354 pp.

- _____, K. Knupp, J. Walters, W. Deierling, M. Gauthier, B. Dolan, J.P. Dice, D. Satterfield, C. Davis, R. Blakeslee, S. Goodman, S. Podgorny, J. Hall, M. Budge, A. Wooten, 2005: The UAH-NSSTC/WHNT ARMOR C-Band Dual-Polarimetric Radar; A Unique Collaboration in Research, Education and Technology Transfer. *32nd Conf. on Radar Meteorology*, Preprints, Albuquerque, New Mexico, Amer. Meteor. Soc.
- Pickering, K.E., Y. Wang, W-K. Tao, C. Price, J.-F. Mueller, 1998: Vertical distributions of lightning NO_x for use in regional and global transport models. *J. Geophys. Res.*, **103**, 31203-31216.
- Price, C., J. Penner, M. Prather, 1997: NO_x from lightning, 1, Global distribution based on lightning physics. *J. Geophys. Res.*, **102**, 5929-5941.
- Pruppacher, H.R., Beard, K.V., 1970: A wind tunnel investigation of the internal circulation and shape of water drops falling at terminal velocity in air. *Q. J. R. Meteorol. Soc.*, **96**, 247-256.
- Rakov, V.A., U.A. Uman, 2003: Downward negative lightning discharges to ground. *Lightning: Physics and Effects*, E.P. Krider, Cambridge University Press, 108-191.
- Rasmussen, R.M., A. J. Heymsfield, 1987: Melting and Shedding of Graupel and Hail. Part I: Model Physics. *J. Atmos. Sci.*, **44**, 2754–2763.
- Reynolds, S. E., M. Brook, M. F. Gourley, 1957: Thunderstorm charge separation. *J. Meteorol.* **14**, 163-178.
- Rutledge, S. A., E. R. Williams, T. D. Keenan, 1992: The Down Upper Doppler and Electricity Experiment (DUNDEE): Overview and Preliminary Results. *Bull. Amer. Meteor. Soc.*, **73**, 3–16.
- NWS ROC, 2013: Radar Operations Center. <http://www.roc.noaa.gov>
- Rotunno, R., J.B. Klemp, M.L. Weisman, 1988: A theory for strong, long-lived squall lines. *J. Atmos. Sci.*, **45**, 463-485.
- Saunders, C. P. R., W.D. Keith, R.P. Mitzewa, 1991: The effect of liquid water content on thunderstorm charging. *J. Geophys. Res.*, **96**, 11007-11017.
- _____, 1994: Thunderstorm electrification laboratory experiments and charging mechanisms. *J. Geophys. Res.*, **99**, 10773-10779.

- _____, S. L. Peck 1998: Laboratory studies of the influence of the rime accretion rate on charge transfer during crystal/graupel collisions, *J. Geophys. Res.*, 103(D12), 13949–13956, doi:10.1029/97JD02644.
- Schultz, C. J., W. A. Petersen, L. D. Carey, 2009: Preliminary Development and Evaluation of Lightning Jump Algorithms for the Real-Time Detection of Severe Weather. *J. Appl. Meteor. Climatol.*, **48**, 2543–2563.
- Skamarock, W.C., J.G. Powers, M.C. Barth, J.E. Dye, T. Matejka, D. Bartels, K. Baumann, J. Stith, D.D. Parrish, G. Hubler, 2000: Numerical simulations of the July 10 Stratospheric-Tropospheric Experiment: Radiation, Aerosols, and Ozone/Deep convection Experiment convective system-Kinematics and transport. *J. Geophys. Res.*, **105**, 19973-19990.
- Smith, P. L., 1984: Equivalent Radar Reflectivity Factors for Snow and Ice Particles. *J. Climate Appl. Meteor.*, **23**, 1258–1260.
- Smith, P. L., D. J. Musil, A. G. Detwiler, R. Ramachandran, 1999: Observations of Mixed-Phase Precipitation within a CaPE Thunderstorm. *J. Appl. Meteor.*, **38**, 145–155.
- Straka, J. M., D. S. Zrnić, R.V. Ryzhkov, 2000: Bulk Hydrometeor Classification and Quantification Using Polarimetric Radar Data: Synthesis of Relations. *J. Appl. Meteor.*, **39**, 1341–1372.
- Takahashi, T., 1978: Riming electrification as a charge generation mechanism in thunderstorms. *J. Atmos. Sci.*, **35**, 1536-1548.
- _____, 1984: Thunderstorm electrification-A numerical study. *J. Atmos. Sci.*, **41**, 2541-2558.
- Torres, S., D. Zrnic, R. J. Doviak, 1998: Ground Clutter Canceling With A Regression Filter. National Severe Storms Laboratory Interim Report, 1313 Halley Circle, Norman, OK, 74069.
- Vivekanandan, J., D.S. Zrnic, S. Ellis, R. Oye, and A.V. Ryzhkov, 1999: Cloud Microphysics Retrievals Using S-Band Dual-Polarization Radar Measurements. *BAMS.*, **80**, 381-388.
- Vonnegut, B., 1953: Possible mechanism for the formation of thunderstorm activity. *Bull. Amer. Meteor. Soc.*, **34**, 378-381.
- Wang, T., A.W. DeSilva, G.C. Goldenbaum, R.R. Dickerson, 1998: Nitric oxide production by simulated lightning: dependence on current, energy, and pressure. *J. Geophys. Res.* **103**, 19149-19159.

- WDTB, 2013: The Warning Decision Training Branch. <http://www.wdtb.noaa.gov/>
- Weisman, M. L., J.B. Klemp, 1984: The structure and classification of numerically simulated convective storms in directionally varying wind shears. *Mon. Wea. Rev.*, **112**, 2479-2498.
- Wiens, K. C., S.A. Rutledge, S.A., Tessendorf, 2005: The 29 June 2000 Supercell observed during STEPS. Part II: Lightning and Charge Structure. *J. Atmos. Sci.*, **62**, 4151-4177.
- Williams, E. R., S. G. Geotis, N. Renno, S. A. Rutledge, E. Rasmussen, T. Rickenbach, 1992: A Radar and Electrical Study of Tropical "Hot Towers". *J. Atmos. Sci.*, **49**, 1386-1395.
- _____, 2001: The Electrification of Severe Storms. *Severe Convective Storms, Meteor. Monogr.*, **No. 50**, Amer. Meteor. Soc., 529-532.
- Wilson, C.T.R., 1929: Some thundercloud problems. *J. Franklin Inst.*, **208**, 1-12.
- Zipser, E.J., K. R. Lutz, 1994: The Vertical Profile of Radar Reflectivity of Convective Cells: A Strong Indicator of Storm Intensity and Lightning Probability?. *Mon. Wea. Rev.*, **122**, 1751-1759.